UC Berkeley

UC Berkeley Electronic Theses and Dissertations

Title
Integrated Multiport Conversion with Rotating Transformer

Permalink
https://escholarship.org/uc/item/9jv2z7rr

Author
Liou, Richard

Publication Date
2022

Peer reviewed|Thesis/dissertation

Integrated Multiport Conversion with Rotating Transformer

By

Richard Ichen Liou

A dissertation submitted in partial satisfaction of the

requirements for the degree of

Doctor of Philosophy

in

Engineering - Electrical Engineering and Computer Sciences

in the

Graduate Division

of the

University of California, Berkeley

Committee in charge:

Professor Seth Sanders, Chair

Professor Robert Pilawa-Podgurski

Professor Dennis Lieu

Summer 2022

Integrated Multiport Conversion with Rotating Transformer

Abstract

Integrated Multiport Conversion with Rotating Transformer

by

Richard Ichen Liou

Doctor of Philosophy in Engineering - Electrical Engineering and Computer Sciences

University of California, Berkeley

Professor Seth Sanders, Chair

Single-phase energy systems are becoming increasingly common due to the rise of residential scale ($\sim$3kW) renewable energy in the US. Integrating storage, sources, and loads poses many challenges associated with power balancing and being resilient to power supply variations or interruptions.

A multi-port hub for integrating a single-phase utility connection, DC battery storage, DC photovoltaic (PV) generation, and critical customer loads is presented in this dissertation. At the core of the system is an electric machine that functions as a multiport rotating transformer, providing voltage conversion, galvanic isolation, 120 Hz ripple energy balancing for single-phase ports, and hold-up energy by use of intrinsic stored kinetic energy in rotation. The energy stored in rotation of the machine is orders of magnitude greater than that available in the capacitor bank often used in static systems and has no associated power versus energy trade-off.

A transverse flux topology was chosen for the rotating transformer due to the topology's true torque scaling with respect to pole pairs and its simple winding configuration. The transverse flux machine was chosen to be have a U-core topology for its relative ease of manufacturing. A convex optimization design method was used to determine the machine physical dimensions and operating speed. The number of stator poles and magnets was specifically chosen to minimize cogging.

A prototype system has been constructed that demonstrates all the functionalities of the rotating transformer. The prototype system validates the multiport system with rotating transformer as an effective and cost efficient method for the integration of typical residential PV components. This dissertation covers the design and implementation of the rotating transformer, its mechanical suspension, the system control, and the system power electronic converters.

Contents

List of Figures

List of Tables

1 Introduction

1.1 The Growth of Residential Scale Photovoltaic Systems

Single-phase energy systems are becoming increasingly common due to the rise of residential scale ($\sim$3kW) renewable energy in the US. The increased number of residential scale solar energy systems can be in part attributed to attractive economics of such systems, along with government incentives. The price of residential solar systems has decreased by more than 60% over the past decade [2]. A 6 kWh system that cost \$50,000 in 2011 cost between \$16,000 and \$21,000 in 2021.

An analysis of the cost decrease can be found in [3] from the year 2020 to 2021. The study found that the driving factors behind the cost decrease of photovoltaic (PV) systems are mainly the technological improvements of the photovoltaic cells. With the technological improvements photovoltaic cells are able to be manufactured more cheaply and also have better efficiencies. On the other hand, the balance of system (BOS) costs representing those of all components other than the photovoltaic panels were found to have slightly increased. The BOS includes mounting hardware, labor, wiring, solar inverters, and so on. Those system components have not benefited from improvements in photovoltaic cell technology.

To further aide in residential PV system adoption, government incentives have been enacted in the recent years. One such program is the US Department of Energy's 2011 SunShot Initiative, aimed to make the unsubsidized cost of solar energy competitive with other forms of energy on the residential, commercial, and utility scale [1]. Additionally, many states in the US have also passed favorable laws for residential PV systems. In 2018, California became the first state to mandate that all newly constructed homes be equipped with PV systems [4].

1.2 Residential Scale PV System Components

Residential scale PV systems contain a mixture of DC and single phase AC sources and loads.

1.2.1 DC Sources and Loads

The DC components in a typical system include the photovoltaic panels and batteries.

Photovoltaic Panels The equivalent circuit of a photovoltaic cell can be seen in Figure 1.1 and its I-V characteristics in Figure 1.2 [8]. The ideal DC current source output I_L is proportional to the cell's solar flux exposure. In order to increase output voltage, current, and power, multiple PV cells are connected in series and parallel to form PV modules. The PV cells in the modules are sealed and protected from the environment. The modules are then connected in series or parallel to form PV arrays with the desired output voltage, current, and power. The PV arrays are connected to power converters that allow the arrays to operate at their maximum power point.
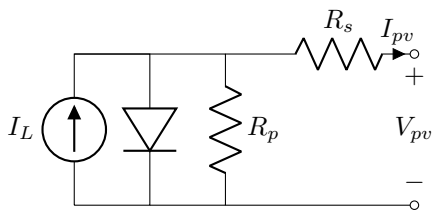
Figure 1.1: PV cell equivalent circuit.
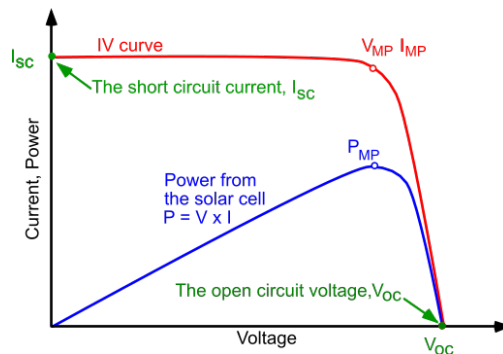
Figure 1.2: PV cell IV curve showing the maximum power point [8].

Batteries   A battery may be modeled as an ideal DC voltage source in series with a parasitic resistor representing its internal resistance. The DC voltage source's value varies based off the battery's state of charge. The internal resistance of the battery may vary depending on its chemistry, state of charge, and charge/discharge rate. The dominant battery chemistry for energy storage is lithium ion.

1.2.2   AC Sources and Loads

The AC components in a residential scale PV system are typically the grid connection and the household loads.

Power Grid   Grid connections to US residential systems are single phase with two hot wires, a neutral wire, and a ground wire. The two hot wires and neutral wire are derived from a center tapped transformer, where the neutral wire represents the center tap. The voltage difference between the hot and neutral wires is 120 Vrms, while that between the two hot wires is 240 Vrms.

   The connections for residential scale PV systems in California are bidirectional, allowing excess locally generated power to be supplied back to the grid. The power converters that interface with the grid must have anti-islanding features so that power will not be supplied to the grid when the transmission line is damaged. Anti-islanding is a precaution to ensure the transmission line is not live during repairs and to prevent the small residential inverter from facing the collapsed grid system.

Household Loads   Household loads can generally be divided into plug loads, lighting, heating, and air conditioning. Plug loads consist of devices that use the standard 120 or 240 V connectors to obtain power from the grid. Plug loads include computers, coffee makers, televisions, etc. Even though a plug load device may be internally powered by DC, they take power from the AC grid and therefore are treated as AC loads.

   A breakdown of household energy usage data obtained from the 2015 Residential Energy Consumption Survey can be seen in Figure 1.3 [5]. As seen in the figure, plug loads account

Residential electricity consumption by end use, 2015
percent of total

air conditioning 17%

space heating 15%

water heating 14%

refrigerators 7%

not elsewhere classified 13%

lighting 10%

TVs and related 7%

clothes dryers 5%

ceiling fans
air handlers (heating)
separate freezers
cooking
dehumidifiers
microwaves
pool pumps
air handlers (cooling)
humidifiers
dishwashers
clothes washers
hot tub heaters
evaporative coolers
hot tub pumps

previously published end uses

new end uses

eia

Figure 1.3: Breakdown of home energy usage [5].

for approximately 50% of household energy usage, and the remaining loads account for the other 50%.

1.3 System Integration Challenges

In order to integrate the numerous DC and AC loads and sources, power balance between them must be achieved. At timescales on the order of seconds, power imbalance events include switchovers of the system power supply (from grid to backup battery, etc.), power supply ebbs, and load surges. During a switchover event, glitches or even the entire momentary loss of power may occur. Additional power supply variations occur due to the intermittent nature of PV arrays. Load surges may occur when loads with high inrush currents turn on or become connected. Holdup energy is required to power the loads throughout such events.

On the millisecond timescale, undesirable power flow results from the pulsating second harmonic power ripple associated with single phase AC loads/sources. The second harmonic power ripple does not allow the PV arrays to operate at their maximum power point and also increases conduction losses due to ripple currents in DC sources such as batteries. Much research has been performed on power decoupling techniques. The techniques can be broadly classified as active or passive.

Passively decoupling the power imbalance involves using capacitors in the inverter DC bus to provide the mismatch in power. Due to the low AC frequency and the respective power levels in residential PV systems, the energy stored by the capacitors is very large, heavily favoring the use of electrolytic capacitors as a cost effective implementation. Unfortunately, electrolytic capacitors suffer from limited life spans [7]. A fundamental limitation associated with passive balancing is the tradeoff between the fraction of total energy utilized for power balancing in the storage capacitor and the capacitor's voltage ripple. The capacitor is sized according to the DC bus voltage ripple constraint, and the majority of the capacitor energy

is unaccessed.

Active power decoupling techniques remove the tradeoff, allowing arbitrary swings of the capacitor voltage. The capacitor can then be sized for only the energy storage requirement and can have a much smaller capacitance. A detailed analysis about the minimum capacitances needed for both active and passive power decoupling techniques can be found in [7]. Active power decoupling adds additional circuitry and control to the power converter in order to drive the capacitor voltage swings.

Conventional solutions using capacitors and supercapacitors as the energy storage elements have a power versus energy tradeoff due to their equivalent series resistance (ESR). The ESR and capacitor form an RC time constant that is indicative of how quickly the capacitor may be charged or discharged and partly determines its power rating. With current capacitor and supercapacitor technologies, the RC time constant increases when the capacitance increases. Because energy stored in a capacitor is proportional to its capacitance, this implies the power and energy tradeoff.

A graph illustrating this tradeoff can be seen in Figure 1.4 where the power per dollar and energy per dollar of various capacitor technologies have been plotted. The power and energy are calculated as

$$P_{cap} = \frac{V^2}{R} = \frac{qV}{RC} \tag{1.1}$$

$$E_{cap} = \frac{1}{2}CV^2 = \frac{1}{2}qV \tag{1.2}$$

where V is the voltage rating of the capacitor, q is the charge stored on the capacitor, R is the capacitor ESR, and C is the capacitance. The power represents the peak power discharged from the capacitor if its terminals were shorted together. The energy represents that which is stored in the capacitor charged up to its maximum rated voltage V. Data was pulled from the electronics supplier Digikey [6]. The general trend of increased power per dollar corresponding to decreased energy per dollar among the various capacitor technologies can been seen.

The power energy tradeoff necessitates the use of different capacitor technologies in order to supply both the holdup and second harmonic power decoupling energy. Supercapacitors are the most cost effective solution to store holdup energy, while ceramic capacitors are the most cost effective solution to store the power decoupling energy. The use of two different technologies however results in additional cost to the system because one capacitor technology cannot perform the function of the other.

In addition to the power balancing challenges, system integration also poses safety and voltage mismatch challenges that may be solved by using transformers. Transformers offer galvanic isolation, which is desirable to avoid any unwanted coupling between system components in the case of faults. It also avoids undesired ground loop currents between the components. Another feature of transformers is their voltage conversion ability that is controlled by the turns ratio between the windings. The ability to convert between various voltage levels is advantageous because the system components naturally have different voltage levels. Power converters function most efficiently when the voltage levels between the input and output are as close as possible. In such cases the switching stress and VA ratings of
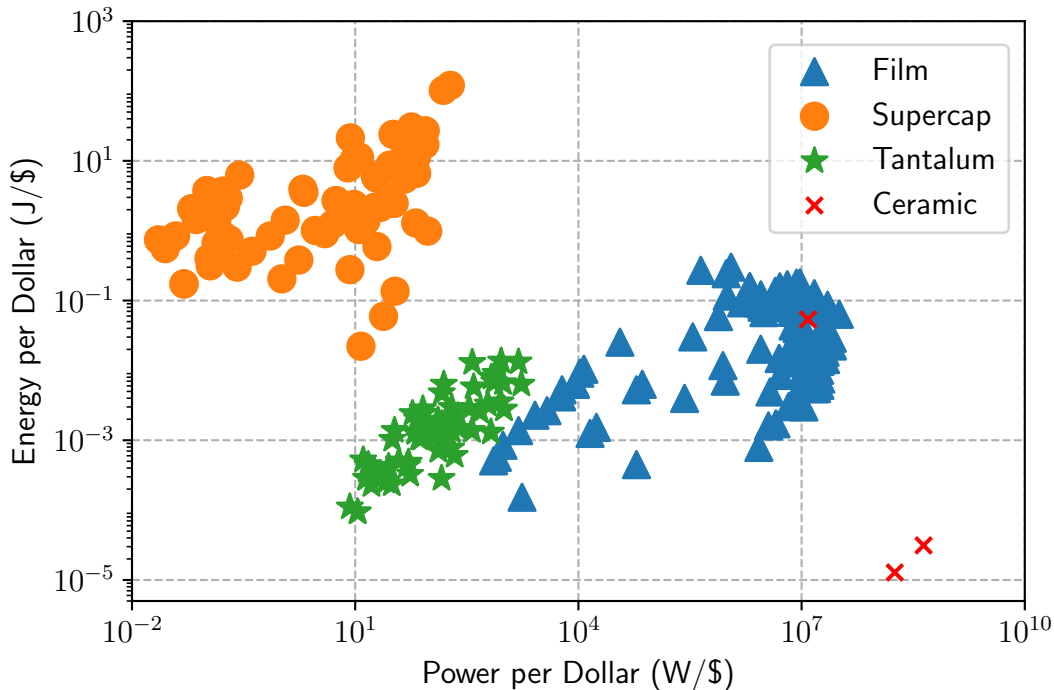
Figure 1.4: Energy vs power cost effectiveness of various capacitor technologies. The general trend of increased power per dollar corresponding to decreased energy per dollar across the various capacitor technologies can been seen. Data obtained from Digikey [6].

the power converter switches may be minimized. The transformer voltage conversion ability overcomes such voltage mismatch challenges.

1.4   Thesis Overview

This thesis presents the design and implementation of a multiport converter using a rotating transformer for residential scale PV systems. The multiport converter enables tight integration of the various system components by presenting a cost effective solution to the challenges described in Section 1.3. The functionalities of and the motivation for the multiport conversion with rotating transformer are presented in Section 2. The design and implementation of the rotating transformer as a transverse flux machine and its mechanical suspension are presented in Sections 3 and 4 respectively. The system control design is explained in Section 5. The construction of the prototype multiport converter is presented in Section 6. Experimental results are shown in Section 7, and conclusions are presented in Section 8.

2   Multiport Conversion with Rotating Transformer

A multiport converter with rotating transformer is proposed for residential scale PV systems. At the core of such a system is an electric machine that functions as a multiport rotating transformer, providing voltage conversion, galvanic isolation, 120 Hz ripple energy balancing for single-phase ports, and hold-up energy by use of intrinsic stored kinetic energy in rotation. The electric machine contains multiple windings that share the same winding area. The windings exhibit magnetic coupling between themselves and also the rotor. The magnetic coupling between the windings allows point-to-point direct power transfer, while the magnetic coupling to the rotor allows for mechanical energy storage and recovery.

The system is expandable to any number of subsystem interconnections, with the example shown in Figure 2.1 as a nominal configuration. In this exemplary system, the four subsystems correspond to AC grid power, DC battery, photovoltaic interface, and resilient customer side AC power.

The multiport converter with rotating transformer is a cost efficient solution for enabling seamless integration of sources and loads while incorporating energy storage in residential scale PV systems. In this section each functionality of the multiport rotating transformer is presented. The active energy storage element costs of the multiport converter with rotating transformer are compared with those in a static transformer system and found to be superior.
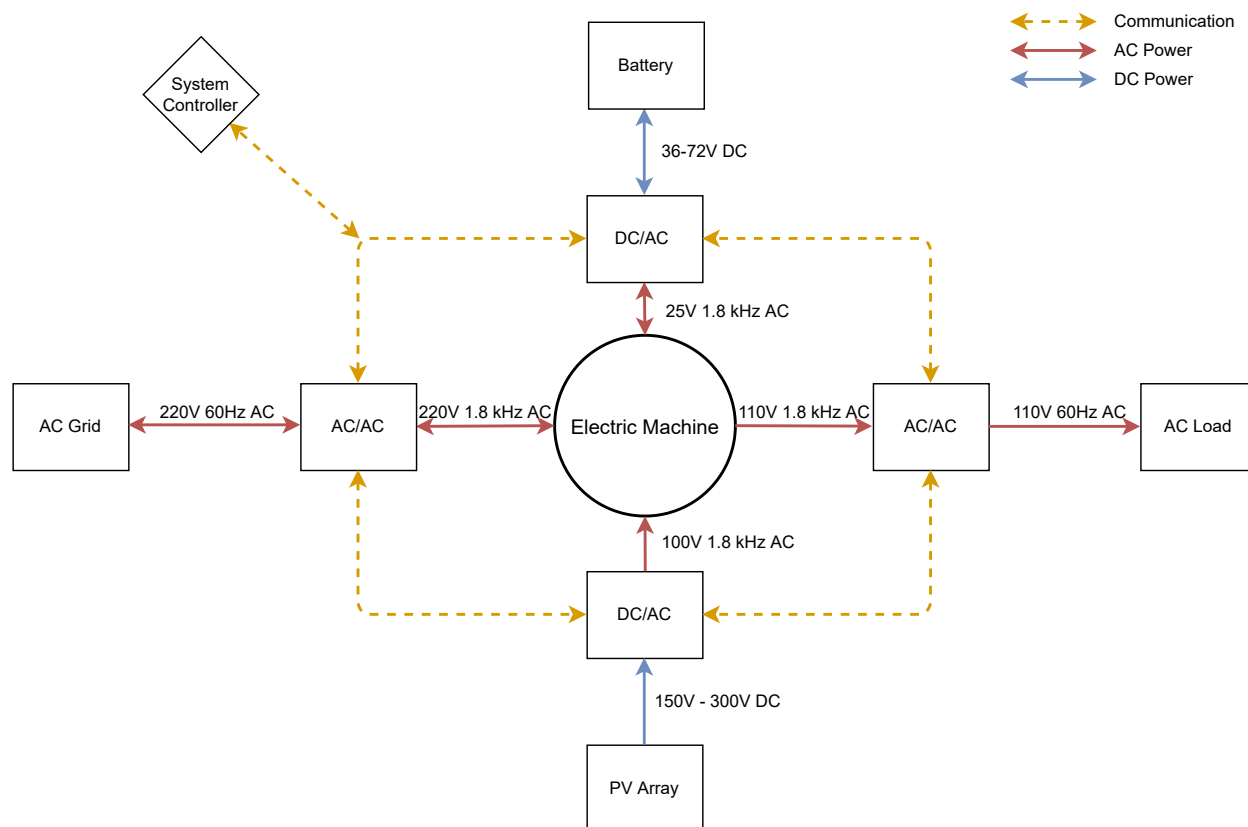
Figure 2.1: Exemplary system. The four subsystems correspond to AC grid power, DC battery, photovoltaic interface, and resilient customer side AC power.

2.1 Holdup Energy

The provision of highly resilient customer power is enabled through the continuously available rotational kinetic energy of the core rotating machine. The rotational energy is directly available to be delivered to customer loads while the system is changing modes, or while any one of the source/storage electrical ports is undergoing a temporary outage, sag, etc. The energy may also be supplied during load surges, allowing the overall PV system to be sized according to the customer average power demands rather than their peak power demands. This represents significant savings on the system level, as the PV array or backup battery no longer must be oversized to handle potential surge events on the order of seconds without failing or blacking out. Component life is also increased by not having to the handle power surges. The additional peak power rating that the rotating transformer adds to the system is substantial and cost-wise unfeasible using capacitors, supercapacitors, or batteries. Furthermore, the availability of the holdup energy adds no complexity, energy conversion loss, nor reliability hazard to the system.

The industry is already beginning to recognize the advantages of mechanical energy storage for holdup energy applications. A startup company called Maxout Renewables is developing their product Evergrid that functions as a mechanical energy storage device targeted at supplying holdup energy for residential PV systems [9]. The product is the winner of the American-Made Solar Prize, an Energy Department's National Renewable Energy Laboratory (NREL) sponsored "multi-million-dollar prize competition designed to energize U.S. solar manufacturing through a series of contests and the development of a diverse and powerful support network that leverages national laboratories, energy incubators, and other resources across the country [10]." The basic Evergrid configuration adds 6.5 kW of peak power for three seconds to the PV system at a target cost of $1000 and requires no special mounting [9].

2.2 Single Phase Power Decoupling

Unlike the supercapacitors typically used for holdup applications, the electric machine may supply energy for both holdup and single phase power decoupling. Second harmonic power balancing can be provisioned at more than one port with simple controls organized on a per-port basis. The individual line frequencies/phases need not be synchronized. The controller drives a power ripple to the machine that is out of phase and equal in magnitude to the AC port ripple. The energy stored in the electric machine rotor is orders of magnitude greater than that available in the capacitor bank often used in static systems. The energy required for power decoupling is insignificant compared to the total energy stored in the machine, and therefore the machine speed ripple is extremely small.

2.3 Voltage Conversion and Galvanic Isolation

The magnetic coupling between the windings allows the electric machine to also function as a transformer. The voltage conversion ability and galvanic isolation offered by transformers are highly beneficial for the efficient and safe integration of system components as described in Section 1.3. While the rotating transformer is connected to all ports, it is important to

note that the majority of power is not converted into mechanical energy. Power that flows directly from port-to-port is not converted to mechanical energy and instead is transferred via magnetic coupling to the other windings. Direct port-to-port power transfer is the main power flow path and does not suffer any efficiency penalties associated with conversion to and from mechanical energy. Only the energy that must be stored or extracted from the rotor will be converted to mechanical energy, and therefore system efficiencies are able to remain high.

2.4   Static vs Rotating Transformer Conversion System

The cost of the rotating transformer system is explored and compared to a static conversion system. The static conversion system was designed to achieve the same efficiency (99%) and energy storage capacity as the rotating transformer system. The comparison is summarized in Table 2.1. Only the costs of the active storage elements and transformer are compared in the table.

2.4.1   Static Conversion System

The static conversion system consists of a multi-winding pot core transformer with capacitors as the energy storage elements. The electrical frequency is chosen to be 100 kHz, a typical value for such systems. The high electrical frequency allows for the miniaturization of the transformer core. The transformer core was designed using the Magnetics T material ferrite core [15]. The T material was chosen for its high permeability that is stable over a wide temperature range. Its loss is also stable over a wide temperature range. The resulting core and copper weight can be seen in Table 2.1. The cost of ferrite is estimated to be about $23 per pound from Digikey data [6]. Copper price is estimated to be $5 per pound based on current market rates [16].

The power decoupling energy is supplied by 450 V X6S ceramic capacitors [13]. An energy of 23 J was used based on the appropriately scaled energy requirements of the Google Little Box Challenge winning circuit [11], [12]. The holdup energy to provide 3 kW for 1s (3 kJ) is implemented using Maxwell Bcap0310 supercapacitors [14]. The total energy of the supercapacitor bank has been sized to be four times the absolute minimum energy to avoid excessive voltage sag. The prices of the capacitors were obtained from Digikey at the largest bulk quantities.

2.4.2   Rotating Transformer System

The rotating conversion system consists only of the rotating transformer as the energy storage element. The rotating transformer has no extra costs associated with storing the 120 Hz power decoupling and holdup energy. The material costs of the machine itself are estimated from market prices and listed in the table. Prices for the amorphous iron were obtained from Magnetic Metals quotes [18], and prices for the magnets were obtained from K&J Magnetics [17]. Steel price is estimated to be $.4 per pound based on current market rates [19].

As can be seen, the rotating transformer system compares favorably in the bill of materials cost to the static one. The cost savings arise from being able to access the same rotating

Table 2.1: Comparison of a Static Conversion System to a Rotating Transformer System

	Static Conversion System			Rotating Transformer System	
	Energy Storage Element	**Cost**		**Energy Storage Element**	**Cost**
120 Hz Energy	23 J of X6S ceramic cap	$126	120 Hz Energy	Rotor (steel)	$0
1s Holdup Energy	Super-capacitor	$135	1s Holdup Energy	Rotor (steel)	$0
	(Eg. 11 x Maxwell Bcap0310)				
	Weight	**Cost**		**Weight**	**Cost**
Core (Ferrite)	.4 lbs	$9	Core (Amorphous Fe)	4.5 lbs	$23
Wire (Cu)	.05 lbs	$.25	Magnet (NdFeB)	.25 lbs	$10
Subtotal	.45 lbs	$15	Wire (Cu)	1 lbs	$5
			Rotor (steel)	15 lbs	$6
Total	2 lbs	$276	**Total**	20.75 lbs	$44

energy at multiple time scales needed for 120 Hz power decoupling and holdup. The energy is stored using inexpensive common grade steel. While the final costs of both systems is difficult to determine, such a comparison highlights the potential of the rotating transformer system to be an effective low cost solution that simultaneously replaces the functionalities of capacitors, supercapacitors, and a multiport transformer.

3   The Transverse Flux Machine

3.1   Motivation

This chapter presents the implementation of the rotating transformer. In general an electric machine with any topology could function as a rotating transformer. A transverse flux machine (TFM) was specifically chosen due to its promising characteristics and interest generated in scientific literature. Among its most promising characteristics is the true torque scaling with respect to pole pairs. In transverse flux machines, the available winding cross sectional area is decoupled from the magnetic pole pair pitch. This allows TFMs to increase pole pair count with no immediate drawbacks. Increased pole pair count results in a higher back emf / torque constant, allowing them to achieve highly efficient power transfer as required by the multi-port system. The scaling is in contrast to conventional radial and axial flux machines, where the available winding cross sectional area is inversely proportional to the number of pole pairs.

Another advantage of TFMs is their simple winding structure, as highlighted in Section 3.2. It is straightforward to place multiple isolated windings within the single prescribed winding area.

3.2   Basic Topology

Transverse flux machines can be broken into two basic topologies: U (C) core and claw pole. The claw pole topology can be seen in Figure 3.1 [25], while the U core topology can be seen in Figure 3.2 [29]. Both topologies may have either single or double sided stators. The machines in Figures 3.1 and 3.2 are single sided. Double sided machines duplicate the stator geometry on the back side of the magnets to better utilize the magnet flux. Additional minor variations exist with the arrangement of the permanent magnets, such as incorporating flux concentration.

The U core topology lends itself to the use of tape wound cut cores, providing a clear and cost effective manufacturing route. The claw pole topology was ruled out because its stator is more difficult to manufacture. More details on the manufacturability of the TFM are found in Section 3.3.2.

A conceptual drawing of the implemented U core TFM can be seen in Figure 3.3. The U core TFM has an outer-rotor geometry, with two circumferential rings of magnets. The outer-rotor geometry allows for shorter turns of the winding, as the winding length of one turn is minimized when the stator is in the machine interior. The inherently single-phase transverse flux machine incorporates a very simple winding geometry, basically one-to-one analogous with the toroidal winding in a conventional pot-core structure. Although the rotating transformer and a pot-core based transformer are topologically equivalent, a fundamental difference is that in the case of the rotating transformer, the magnetizing excitation is provided by the rotating permanent magnet assembly.

To obtain a basic understanding of how the machine functions, Section A-A in Figure 3.3 shows a cross-section transverse to the winding. In the drawn state, magnet flux flows in the counter-clockwise direction around the winding. As the rotor turns, the magnet flux reverses directions to flow clockwise, inducing a time varying flux linkage in the winding and
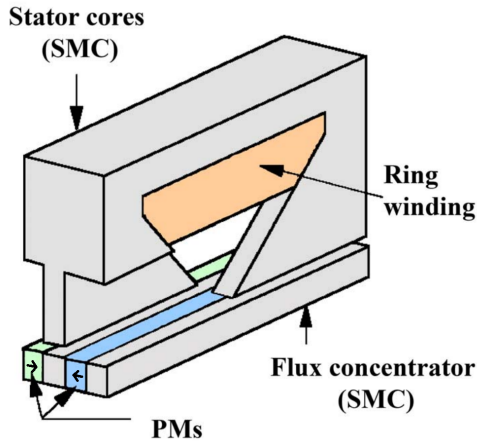
Figure 3.1: Simplified drawing of a single sided claw pole TFM topology with one pole pair [25]. The rotor consists of the permanent magnets and flux concentrator. As drawn the direction of movement is normal to the cross section plane.
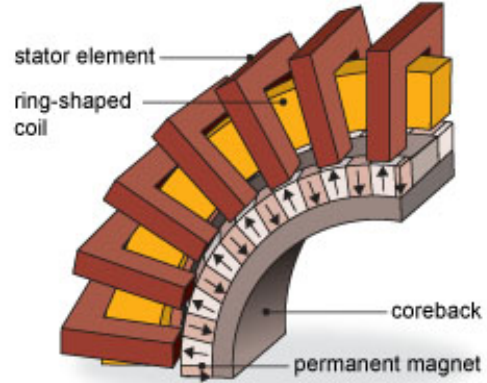
Figure 3.2: Simplified drawing of a single sided U core TFM topology with seven pole pairs [29]. The rotor consists of the permanent magnets and coreback. The direction of movement is normal to the cross section plane.

thus a back emf.

It is important to note that Figure 3.3 is simplified for conceptual purposes. Section 3.3 elaborates on the various additional challenges that arise with such a topology.

3.3 Topological Challenges

3.3.1 Simulation

Unlike in conventional radial and axial flux machines, the active AC flux paths in TFMs are 3D. Simplifying the 3D geometry into a 2D one is desirable in order to reduce computation burden, but not as straightforward as with conventional machines. However, it is still possible, and a 2D model was formulated in which the U cores are straightened out into vertical rectangular columns on a rectilinear grid. The magnets follow and are located at the ends of the columns. An example of such a transformation can be seen in Figure 3.11. The approximated 2D geometry is sufficient for magnetostatic simulations, but the 3D models still must be used for complete electromagnetic simulations.

3D magnetostatic simulations were initially performed while optimizing the machine dimensions. They were used to correct the results of analytical formulas derived from 1D magnetic circuit analysis in Section 3.4.1. After manufacturing the initial prototype, 2D simulations were used to devise subsequent improved topologies, greatly reducing design iteration times. The 2D simulations were especially useful when the candidate topologies were no longer periodic and the entire geometry must be simulated, as is later the case in Section 3.5.
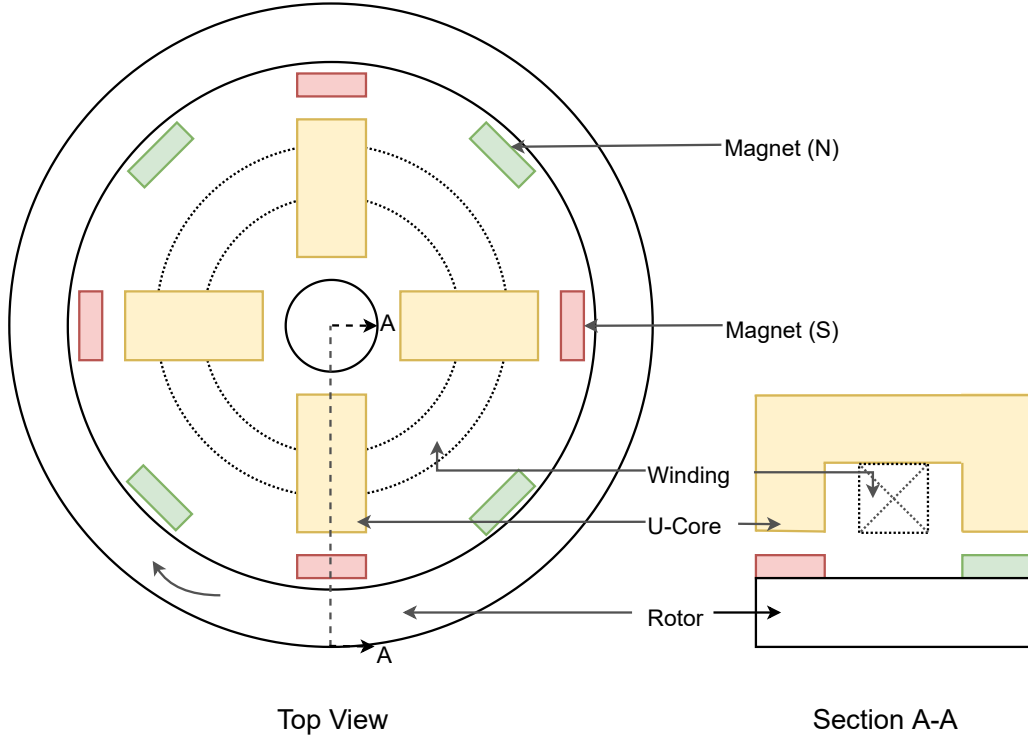
Figure 3.3: Simplified U core TFM topology with four pole pairs.

3.3.2 Manufacturability

3D flux paths also lead to challenges in manufacturability. The U core topology was selected because the stator could be manufactured from mass produced tape wound cut cores that are commonly used for inductor or transformer designs. The cut cores consist of laminations wrapped around a mandrel, bonded, and then cut diametrically.

A further advantage of using cut cores is that they are available as amorphous iron alloys. Amorphous iron alloys have higher permeability and lower AC magnetic loss than silicon steel. Despite their superior magnetic properties, they have not been used in conventional motors because they are costly to manufacture. The laminations must be produced with thicknesses less than 40 μm in order to achieve the rapid cooling rates required to retain their random atomic structure when quenched from a liquid state [26]. The resulting material is extremely hard and brittle, requiring more advanced techniques such as laser cutting, water jetting, or wire EDM to form the desired shape. These difficulties in working with amorphous iron alloys have restricted their wider adoption.

Soft magnetic composites (SMC) are another potential technology that were considered for use. Standardized techniques such as die forming exist to manufacture SMCs into desired 3D geometries [27]. SMCs are magnetically isotropic and have lower eddy losses than laminated steel due to their composition of small insulated particles. While their hysteresis losses are higher than silicon steel, their lower eddy losses allow SMCs to potentially have the same or even less total magnetic loss at the operating frequencies for this application. However experiences as summarized in [28] have shown that SMCs do not always deliver on the promised low losses. Another drawback of SMCs is their low permeability due to the

presence of a distributed air gap.

3.3.3 Non-smooth Air Gap

The smoothness of the air gap is the term used to describe the variation in air gap energy vs rotor angle. If the rotor is non-salient as in the TFM, then the term also describes the variation in the stator reluctance around the air gap. A smooth air gap in the TFM indicates that there is little variation in reluctance seen by the rotor and thus little variation in the corresponding air gap energy. The simplified drawing in Figure 3.3 has a non-smooth air gap. In the aligned position where the magnets are aligned with the U core faces, the reluctance that the magnets see is at the minimum. In the misaligned position, the reluctance is at the maximum.

The machine's magnetically preferred position is at the aligned position. The aligned position is a stable equilibrium point, and the misaligned position is an unstable one. The existence of those preferred positions causes cogging. Excessive cogging causes undesired vibrations and noise. It also causes thermal stresses on the drive train and machine during startup due to the large currents required to overcome the cogging when there is no rotor inertia to aid rotation.

The non-smooth air gap also causes eddy current losses in the magnets and rotor back iron. As drawn in Figure 3.3, the magnets will experience a varying reluctance with respect to the rotor angle. The varying reluctance changes the operating point of the magnet as the rotor rotates, resulting in an AC flux swing in the magnets and rotor back iron.

3.3.4 Magnet Leakage

Limiting the pole pair scaling of transverse flux machines is the magnet leakage flux that does not link the winding. As the number of pole pairs increases, the average magnetic path length in the air gap to the neighboring magnet becomes comparable to the air gap itself. Therefore, continuing to increase the number of pole pairs will eventually result in reduced magnet flux linkage to the point where the machine performance will not be improved.

3.4 Initial Design and Prototype

Overcoming the topological challenges outlined in Section 3.3 requires modification of the drawing in Figure 3.3. A smooth air gap is desired in order to eliminate cogging and magnet eddy current loss. In order to smooth the air gap, I-cores were added over the inactive magnets, creating a stator facing polygonal air gap. The U and I cores are complementary cut core pairs cut from the same structure. However, results of a FEA simulation showed that the cogging torque was comparable to the operating torque and thus still too large.

A ring of steel laminations was designed to be included on the stator outer diameter, further reducing the air gap irregularity. On the outer diameter, the laminations are circular. On the inner diameter there are flats to mate with the faces of the cut cores. The laminations allow for flux concentration in the cut cores. The radial dimension in the bridging section of the steel laminations between the U and I cores had to be carefully designed. The larger the radial dimension, the smoother the air gap becomes. However, there would also be
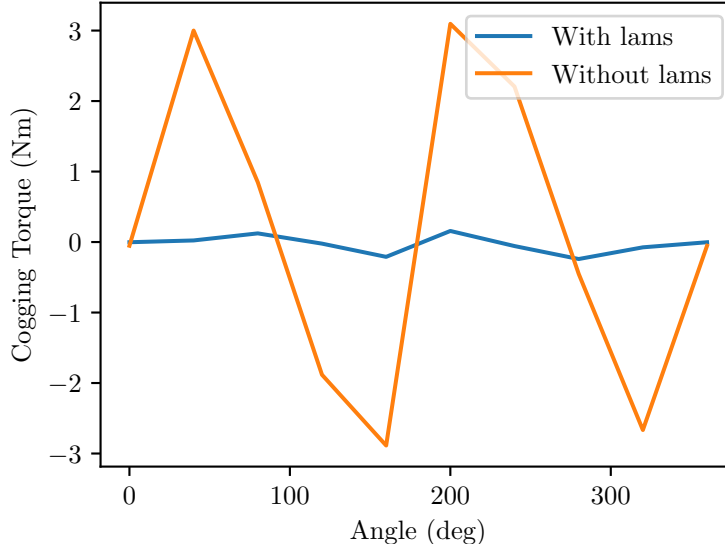
Figure 3.4: FEA results showing the cogging torque with and without the steel ring laminations. The period is one magnet pole pair pitch.

increased magnet flux leakage between the U and I cores. The bridging section relies on the saturation characteristic of steel to limit the amount of magnet flux leakage in the aligned position. After adding the laminations, the FEA showed that the cogging became negligible, indicating that a smooth air gap was achieved. The cogging torque simulation results can be seen in Figure 3.4. The resulting topology that was built as the first prototype can be seen conceptually in Figure 3.5. A picture of the initial prototype's stator can be seen in 3.10.

3.4.1 Convex Optimization Design Approach

The machine physical dimensions and optimal operating point are now determined. With the chosen topology, six geometric free variables and their corresponding constraints were identified that completely characterize the machine's physical dimensions. The final free variable, mechanical speed, defines the machine operating point. A constrained optimization was carried out over the seven free design parameters which are listed in Table 3.1. The magnet and winding window dimensions are indicated in Figure 3.6. As seen in the figure, the U core cross-sectional dimensions are constrained to match those of the magnets. The optimization scenario is taken to be a holdup or power balancing operation where full power is being transferred to the motor through only one winding. During this mode of operation, the winding self inductance limits the power transferred. For normal operation where power is transferred directly from one port to another, the series impedance consists only of the leakage inductances.

The following two step process was used to determine the optimal machine parameters.

1. The problem was approximated as a geometric program [20], a class of nonlinear convex optimization problems. While the geometric program problem formulation is limiting,
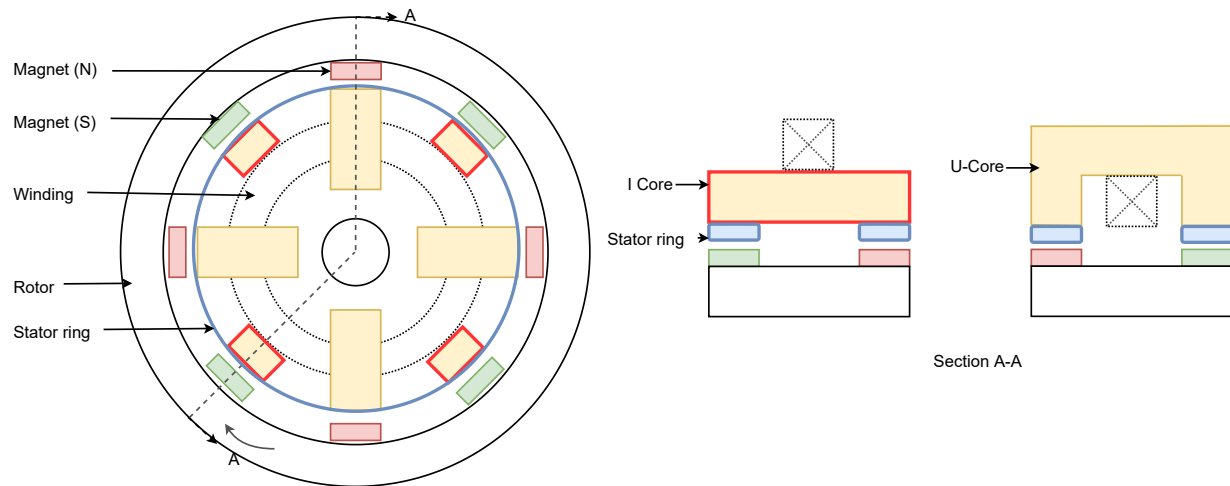
Figure 3.5: Conceptual initial prototype topology with a smooth air gap by adding the I cores and stator ring laminations.

Table 3.1: Design Free Variables

Free Variable	Optimized Value
Magnet dimensions	
$\quad m_1$: axial, m_2: radial, m_3: azimuthal	0.25 in. x 0.125 in. x 0.5 in.
Winding window dimensions	
$\quad w_1$: axial, w_2: radial	3 in. x 0.92 in.
Mechanical speed (ω_m)	7200/120 rpm/Hz
Pole pairs (pp)	15
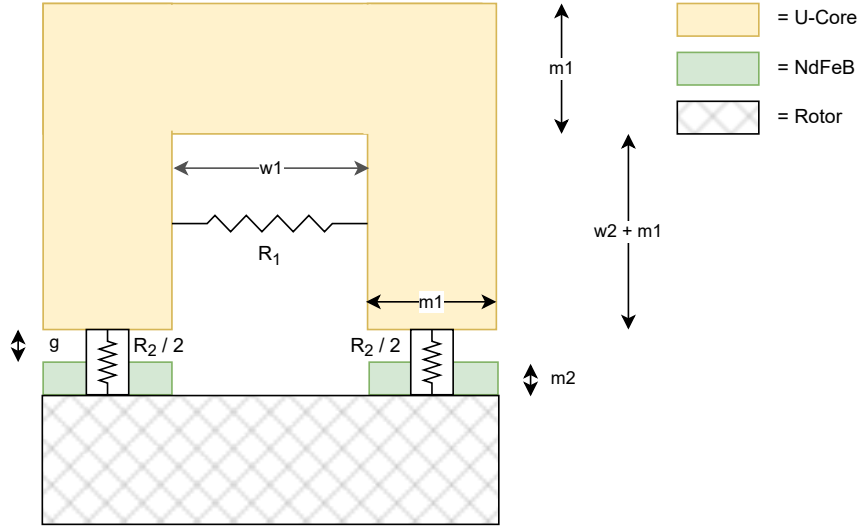
Figure 3.6: Design parameters m_1 and m_2 are the magnet axial and radial dimensions respectively, while the parameters w_1 and w_2 are the winding window axial and radial dimensions respectively. The reluctance R_2 represents the reluctance of the air gap flux path. The reluctance R_1 approximates the leakage reluctance of the flux path through the winding window area. Neighboring I cores exist in the azimuthal direction (in/out of the page) and reduce the radial dimension available for the winding by m_1.

its solution is computationally tractable. The optimal solution to the problem is also guaranteed to be unique. Any approximations to enforce convexity are explicit and allow greater understanding of the problem's solution.

2. An exhaustive search was performed in the neighboring regions of the solution to the geometric program. This step is necessary to find feasible solutions that incorporate the original non-convex constraints. With the explicit exhaustive search, variables can easily be swept over integer ones or over predefined values, for example constraining the number of pole pairs to be an integer number or limiting the magnets to have off-the-shelf dimensions.

The standard form of geometric programs is:

$$
\begin{aligned}
\min_{\mathbf{x}} \quad & f_0(\mathbf{x}) \\
s.t. \quad & f_i(\mathbf{x}) \leq 1 \qquad i = 1, \ldots, m \\
& g_i(\mathbf{x}) = 1 \qquad i = 1, \ldots, p
\end{aligned}
\tag{3.1}
$$

where $f_i(\mathbf{x})$ are posynomials, $g_i(\mathbf{x})$ are monomials, and $\mathbf{x} \in \mathbb{R}^n$ is the vector of optimization variables [20]. The objective function f_0 is a posynomial. A function is a posynomial $f(\mathbf{x})$

if it can be expressed as a conical combination of monomials $g_k(\mathbf{x})$:

$$g_k(\mathbf{x}) = c_k \prod_{i=0}^{n} x_i^{a_i} \qquad f(\mathbf{x}) = \sum_{k=0}^{K} \alpha_k g_k(\mathbf{x}) \tag{3.2}$$

where a_i are real and x_i, c_i, α_k are real and nonnegative. The above definition of a monomial in the context of geometric programming is different than that used in algebra and should not be confused with it.

The machine design problem can be stated as:

$$\min_{\boldsymbol{m},\boldsymbol{w},\omega_m,pp} f_0 \tag{3.3}$$

$$s.t. \quad \frac{1}{f_1} \leq \frac{1}{P_{des}}, f_2 \leq M_{cores}$$

where f_0 is the sum of the losses (accounting only for core loss and DC winding resistance of one winding), f_1 the amount of power the machine can handle, f_2 the weight of the magnetic cores, $\boldsymbol{m}$ the vector containing the 3 dimensions of the magnet (axial, radial, azimuthal), $\boldsymbol{w}$ the vector containing the 2 dimensions of the winding area (axial, radial), ω_m the machine mechanical frequency, and pp the number of pole pairs. Variables that are normally integers such as pole pairs are allowed to be real numbers, as optimization over integers is non-convex. For the target application P_{des} is set to 3 kW and M_{cores} to 2.27 kg (5 lbs).

Additional constraints ensuring the mechanical feasibility of the solutions can be derived from the geometry and also shown to be posynomials. In order to reduce the effects of magnet leakage flux, a lower bound constraint on the azimuthal magnet dimension m_3 was also necessary. As previously noted in Section 3.3.4, this limits the pole pair scaling of the transverse flux machine.

Using the solution obtained from the geometric program, an exhaustive search in the vicinity was performed. The pole pair variable was varied with integer values around the solution from the geometric program. An additional intermediate variable, the number of turns of one winding, was also enforced to have integer values. The remaining variables were also perturbed around their original solutions to finally obtain the best solution that had the least loss while satisfying the constraints was chosen. Contour plots plotting the trade-offs between the magnet and winding window axial dimensions can be seen in Figure 3.7. The efficiency is equal to $1 - f_0/P_{des}$, where f_0 is the sum of the machine losses and P_{des} is the target machine power.

The design equations $f_{0,1,2}$ are now shown to take the form of posynomials using models that are developed from magnetic circuit analysis and mechanical geometry. Because the problem is not convex with respect to the magnet's radial dimension m_2, m_2 was chosen such that a flux level of 1 T in the core is achieved with a 1 mm air gap. The 1 T flux level was chosen to operate within the linear region of the amorphous iron BH curve. To find core loss, a second order polynomial relating core loss power density vs frequency at 1 T was fit to empirical data supplied by the U-core and steel lamination manufacturers. The volume

17

of the magnetic U-cores plus magnetic shunts is calculated as:

$$V_{core} = 2m_1m_3(pp)(w_1 + w_2 + 3m_1) \tag{3.4}$$

where m_1 and m_3 are the magnet axial and azimuthal dimensions respectively, w_1 and w_2 are the winding window axial and radial dimensions respectively, and pp the number of pole pairs. In a similar process the core losses of the stator ring were parameterized and determined.

The machine functions as a multiport rotating transformer and therefore has multiple independent windings sharing the winding area. For the winding loss, the area A_w and length l_w for a single turn of one winding are calculated as:

$$A_w = w_1w_2k_p \qquad l_w \approx 2(pp)(m_3) \tag{3.5}$$

where k_p is the packing factor divided by the number of windings in the machine. The winding length expression is the length for a single turn of a winding. It slightly overestimates the true value but is needed to preserve convexity. For each pole pair, the winding travels in the azimuthal direction for an approximate distance equal to the azimuthal dimension of one U-core and one I-core. The azimuthal dimension of each core is equal to that of the magnet m_3.

Finally the total loss for one winding is found as:

$$f_0 = \alpha V_{cores} + (NI)^2 \frac{\rho_{cu}l_w}{A_w} \tag{3.6}$$

where α is the core loss power density as a second order polynomial function of frequency for a given 1 T flux density, ρ_{cu} is the resistivity of copper, I is the full load current, and N is the number of turns.

The amount of power that can be transferred through the machine under the assumption that the terminal and back emf voltage magnitudes are equal is:

$$f_1 = \frac{V_{emf}^2}{X}\sin\theta = \frac{(\omega_e\phi)^2}{X}\sin\theta \tag{3.7}$$

where ϕ is the magnet to winding flux linkage, $X = \omega_e L_s$, L_s is the self inductance of one winding, and θ is the angle between the terminal and back emf voltages. The angle to achieve maximum power transfer is $\pi/2$, but operating at or near that angle is undesirable due to motor controller stability issues. The angle at the nominal operating point is assumed to be $\pi/3$.

The winding flux reluctance path over the span of one U-core R was modeled based on

its geometry as:

$$R_1 = \frac{w_1}{\mu_0(w_2 + m_1)m_3} \tag{3.8}$$

$$R_2 = \frac{2(g + m_2)}{\mu_0 m_1 m_3} \tag{3.9}$$

$$R = \frac{R_1 R_2}{R_1 + R_2} = R_1 \| R_2 \tag{3.10}$$

where μ_0 is the permeability of free space. The magnetic paths corresponding to R_1 and R_2 can be seen in Figure 3.6. Assuming a unity turns ratio, the winding self inductance can be approximated as:

$$L_s = 2\frac{(N^2)(pp)(k_r)}{R} \tag{3.11}$$

where N is the number of turns, pp the number of pole pairs, and $k_r = 5$ a factor relating the estimated inductance to the FEA simulated one. While the leakage reluctance R_1 is not a posynomial, its inverse that is used in the problem formulation is.

The inductance equation 3.11 without the k_r factor does not predict the inductance as accurately as FEA simulations. FEA simulations were run for several design points. The factor k_r was then determined by comparing the predictions from the FEA simulations and the equation 3.11 without k_r. The factor k_r was then incorporated into the inductance equation to improve its accuracy.

The winding magnet flux linkage was found as:

$$\phi = k_f(pp)B_g m_1 m_3 \tag{3.12}$$

where $k_f = 0.8$ is a factor relating the estimated flux linkage to the FEA simulated one and $B_g = 1$ T. The reason for the inclusion of the k_f factor is the same as the k_r factor, except with regards to the magnet flux linkage instead of the winding self inductance.

Finally, the weight of the magnetic cores f_2 is equal to their volume in (3.4) multiplied by their density.

Maximizing the ratio of rotor-stator mutual flux to the stator leakage flux, or in other words the back emf to winding impedance ratio (neglecting wire resistance), has been noted as a figure of merit in [21, 22]. This flux ratio is slightly different than the objective function in (3.7) where the mutual flux is squared, but the two ratios are closely related. A favored design trend was having a large axial winding window dimension, as it is beneficial to both reducing stator leakage flux and also increasing winding cross sectional area. The final optimized variables can be seen in Table 3.1. The convex optimization code that contains all constraints and details can be found in the Appendix Section B.

A 3D magnetostatic simulation to find k_r and k_f can be seen in Figure 3.8. To find k_r, a test remanent flux density in the axial portion of the U-core was defined. The operating flux density on the U-core mid axial height cross section plane was found and used to calculate self inductance for one turn. To find k_f, the magnet remanent flux density was defined, and then the flux density over the same mid axial height U core cross section was integrated to

19
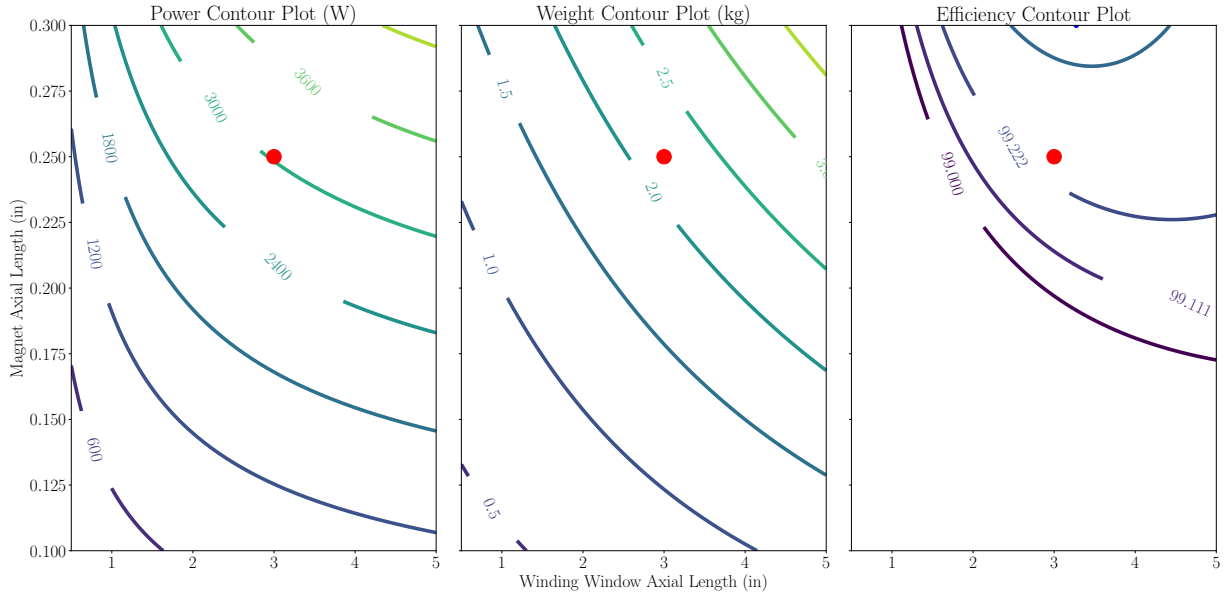
Figure 3.7: Power, weight, and efficiency trade-off contour plots. The red dot indicates the optimal value after performing the exhaustive search.

find the magnet flux linkage.

3.4.2 Winding Design

Due to the high electrical frequency of the machine, litz wire is used to reduce AC wire losses. The design procedure follows that in [23]. Choosing the optimal number of strands is a trade-off between DC and AC winding losses. As the number of strands increases, insulation begins to occupy a larger fraction of the winding space and increases the DC winding resistance. Analytical expressions based on experimental data for the ratio of copper to insulation as the wire size is varied are also derived in [23]. AC losses are dominated by proximity effect for properly sized litz wire, as normally the strands are so small that skin effect can be ignored. A simplified model of loss for one strand consists of the eddy current loss due to a transverse uniformly distributed AC magnetic field in a conducting cylinder and is given in (3.13), where P is the power dissipation, l the length of wire, B the peak flux density, d the diameter of the strand, and ρ_c the resistance of copper.

$$P = \frac{\pi \omega^2 l B^2 d_c^4}{128 \rho_c} \tag{3.13}$$

The AC and DC losses are plotted in Figure 3.9, the red dot representing the chosen number of strands. The litz wire used in the machine is 8 AWG (105/28) equivalent.
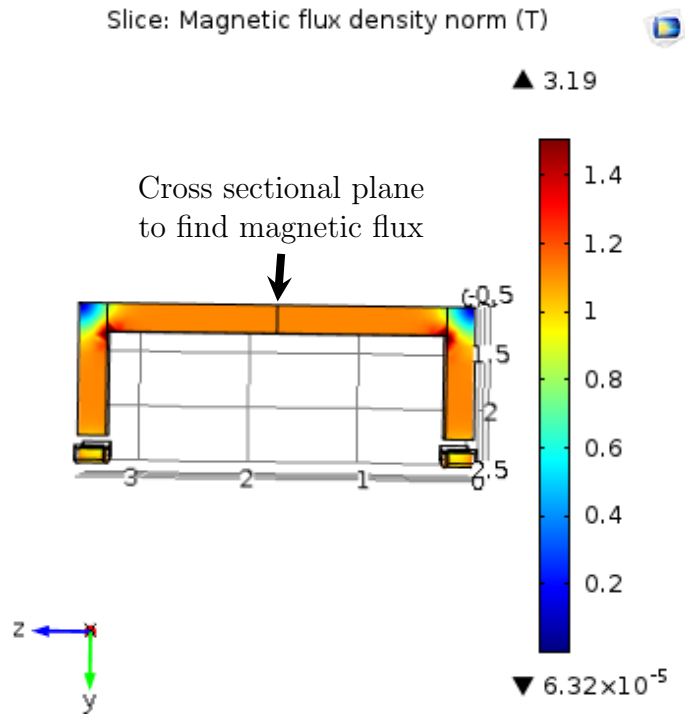
Figure 3.8: 3D FEA magnetostatic simulation used to correct the flux linkage predictions from 1D magnetic circuit analysis. I-cores and the stator laminations are hidden for better U-core visibility. The location of the mid axial height U-core cross-section plane over which the flux is integrated is labeled.
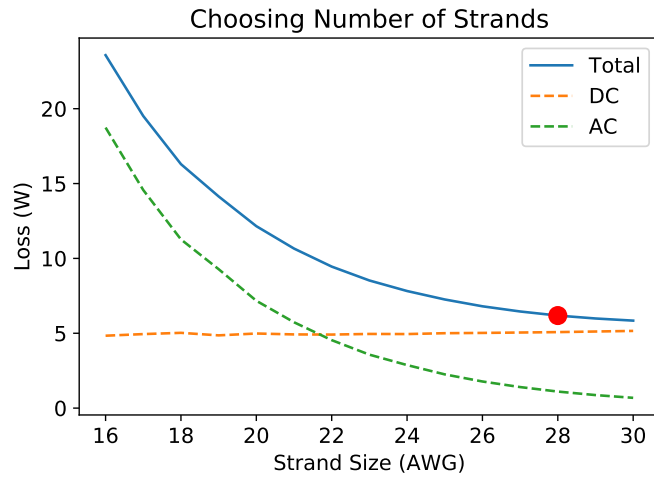
Figure 3.9: Choosing the optimal number of strands in litz wire.

3.4.3 Analysis of Results

The initial prototype was built, with the manufacturing process described in Section 6. A photo of the stator can be seen in Figure 3.10. After assembly, the cogging was found to be 3 Nm, higher than predicted by the FEA simulation. Core loss was also much higher than expected. The suspected reason for the observed behavior was that the U and I cores did not mate perfectly with the lamination ring due to mechanical tolerances. The cut core radial dimension tolerance was approximately ±0.5 mm. This caused small parasitic air gaps to exist between the cut cores and lamination ring.

An interesting singularity in the cogging torque was observed in the FEA simulation when small parasitic air gaps were added between the cut cores and lamination ring. With zero air gap, the simulation predicted zero cogging. However, once parasitic air gaps as small as 0.1 mm were added, the simulation predicted around 1 Nm of cogging. To explain such a phenomena, the flux distribution in the stator was more closely examined.

At positions where the lamination and magnet faces are perfectly misaligned, there is no magnet flux linkage by design. Instead of linking the winding, the magnet flux leaks azimuthally to the neighboring magnet. The leakage flux is equal to the amount of active flux, and this flux distribution realizes the smooth airgap. The lamination ring itself was not designed to support the entirety of the leakage flux. The cut core helps in distributing the leakage flux. When a small parasitic air gap is present between the cut cores and lamination ring, the leakage flux is discouraged from flowing through the cut cores. The lamination ring saturates, and the amount of leakage flux is reduced. The difference in flux between the aligned and misaligned positions causes cogging and core loss in the magnets and rotor back iron. FEA simulations that confirm the theory can be seen in Figure 3.11. The simulations predict 3 Nm of cogging that matches experimental data when a 0.5 mm parasitic air gap is added.

Many design ideas were explored to remedy the cogging and loss. Non-conductive magnets such as bonded neodymium and ceramic were considered in order to eliminate magnet eddy loss. Unfortunately the remanent flux density of such magnets is considerably lower than neodymium ones, resulting in significantly reduced machine performance. The loss in performance penalty is more severe than the eddy loss reduction benefit.

To eliminate the large cut core mechanical tolerances, steel laminations were considered as replacements. The U-cores would be split into three stacks of laminations where the lamination planes are rotated 90° with respect to each other. The two arms of the U-cores would be replaced with axially laminated steel sheets, while the remaining portion would be replaced with azimuthally laminated sheets. This idea was ultimately not implemented due to the mechanical complexity of the assembly and uncertainties about the increase of magnetic loss due to the joints.

3.5 Magnet to Stator Pole Count Mismatch Design and Prototype

Inspiration to solve the cogging issue arose from examining conventional slotted surface mount permanent magnet motors. In such machines, the number of stator slots is chosen strategically such that its least common multiple (LCM) with the number of magnets is as high as possible. It can be shown that cogging is highly dependent on the LCM, with
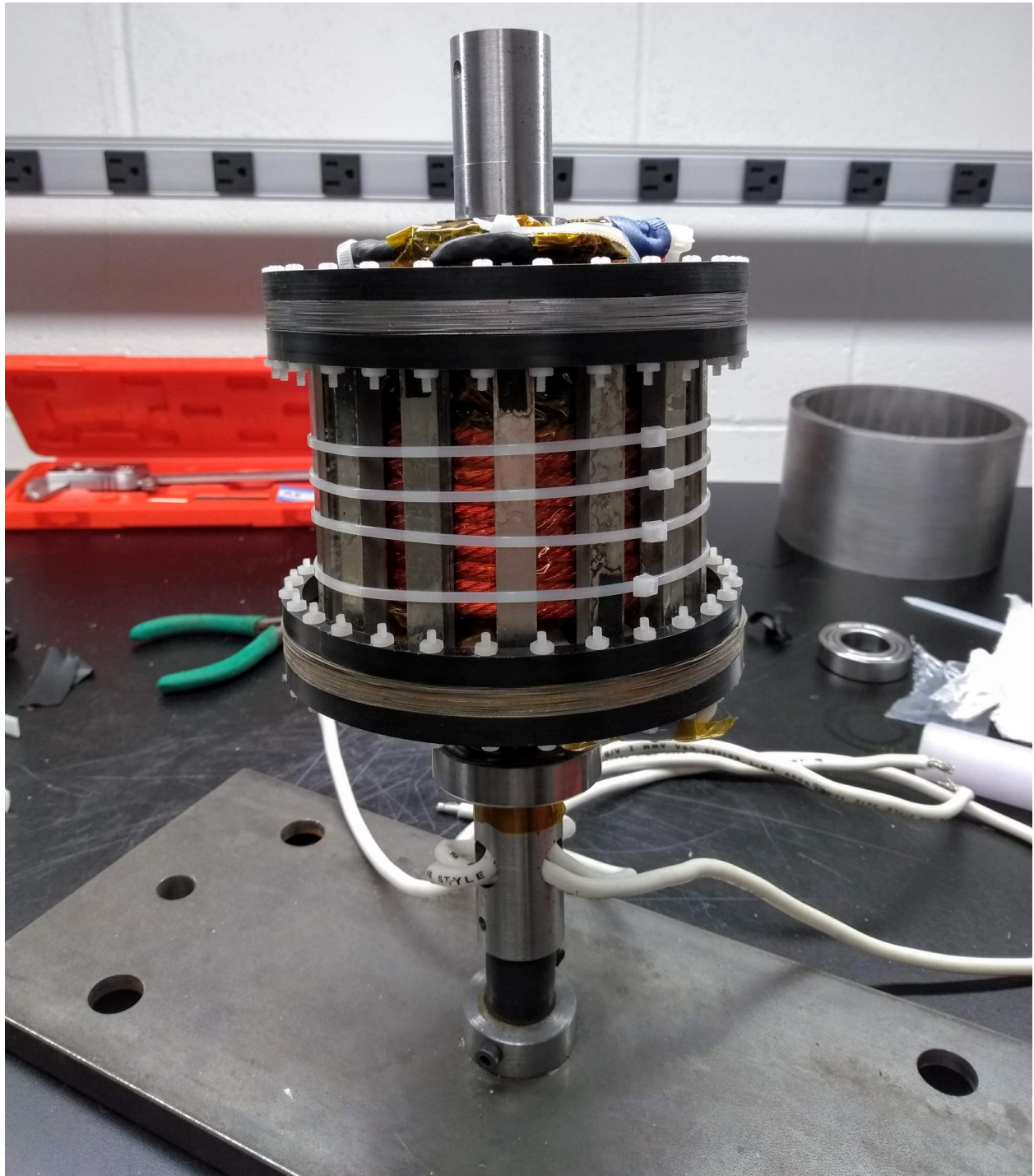
Figure 3.10: Initial prototype stator.
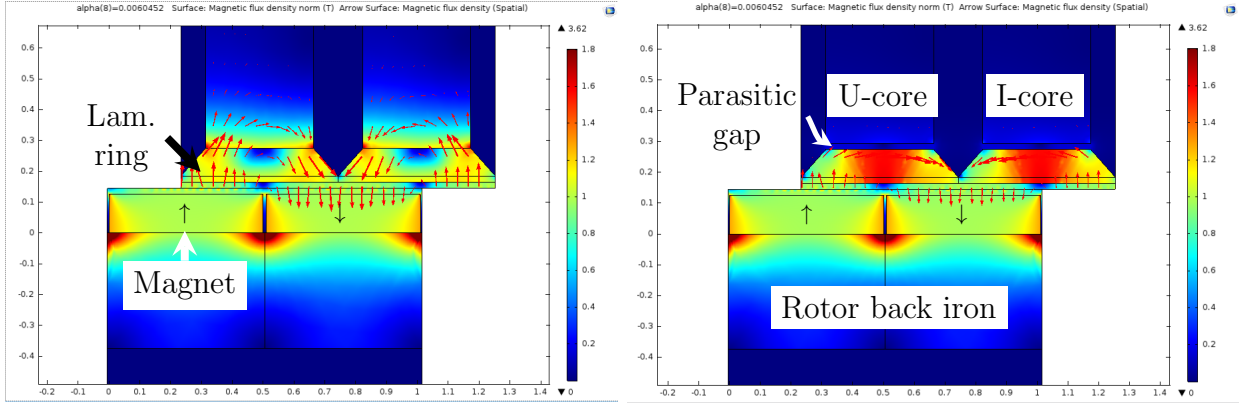
Figure 3.11: Flux distribution of the position where the magnet and stator lamination faces are misaligned. On the left no parasitic gap is present, and the leakage flux is evenly distributed between the lamination ring and cut cores. On the right a 0.5 mm parasitic gap is present, and the leakage flux is limited by saturation in the lamination. The red arrows represent the magnetic flux density angle and magnitude. The magnitude of the magnetic flux field is proportional to the length of the arrow.

larger numbers indicating lower cogging [24]. The transverse flux machine was modified to have 29 magnets on each circumferential ring while keeping the 30 stator cut cores. This modification achieves a high LCM between the magnets and cut cores, reducing the cogging to negligible amounts. It also required minimal modifications to the initial prototype.

Initially, an interior permanent magnet arrangement was considered where the magnets are embedded inside of laminations to address the remaining magnet eddy loss issue. In doing so, the stator laminations can be removed. Instead of smoothing the air gap on the stator side, the smoothing is done on the rotor side. Compared to the stator laminations, the rotor laminations experience much lower loss. When the laminations are on the stator, they experience full flux polarity reversal from the rotating magnets. When they are on the rotor, they co-rotate with the magnets and experience nominally no AC flux swing. Careful design is necessary for the bridging sections of the laminations to avoid excessive magnet leakage flux while ensuring adequate mechanical integrity and flux linkage.

After performing FEA simulations, it was found that embedding the magnets was not necessary. With the stator laminations removed, the air gap on the stator side is polygonal. Even so, the eddy loss in the magnets was found to be sufficiently low. The rotor laminations behind the magnets were kept however, as they could serve two purposes. First, they are a mechanical adapter to modify the existing rotor to accept 29 magnets in each ring. Second, they conduct the AC flux behind the magnets with low loss. The improved conceptual topology can be seen in Figure 3.12.

Removing one magnet does unfortunately reduce the magnet flux linkage. To understand the loss in flux linkage, it is noted that an average non zero torque is generated only when the stator and rotor magnet fields have the same spatial and temporal frequency. The spatial period is taken to be one 2π rotation around the air gap. With an instantaneous current I in the windings, the 30 stator cut cores generate a 15th spatial harmonic mmf. With a sinusoidal current, the cut cores generate a 15th spatial harmonic and forward (and
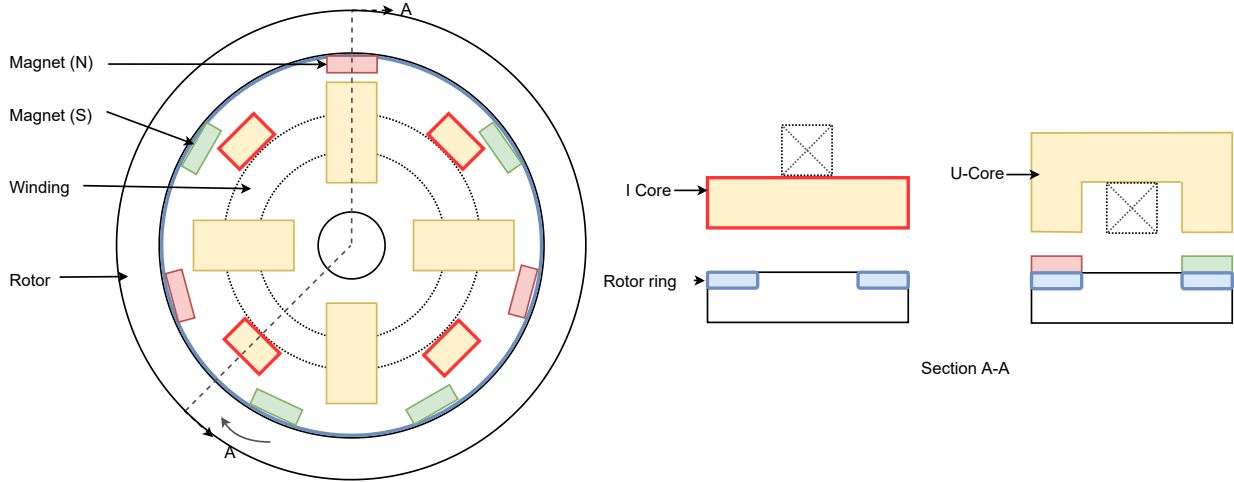
Figure 3.12: Conceptual prototype topology with a mismatch between magnet and stator pole count. The number of stator cores and magnets illustrated do not represent their actual counts.

backward) traveling mmf wave. Therefore the 15th spatial harmonic mmf on the rotor is the only torque producing component. By reducing the number of magnets to 29, the 15th spatial harmonic rotor mmf wave is reduced to about 63% of that generated by a 30 magnet rotor. The normalized and idealized 29 magnet rotor mmf pattern and its 15th harmonic can be seen in Figure 3.13. In three phase slotted surface mount permanent magnet motors, there is design freedom to select a suitable combination of slots and magnet poles with little impact on performance. Unfortunately, this is not the case with transverse flux machines.

The overall electromagnetic design is otherwise unchanged. The effective pole pair count is still 15. The core loss in the cut cores still experience very similar loss because their AC flux density has almost the same frequency and magnitude. The reduced magnet flux linkage motivated increasing the operating speed from 7.2 krpm to 8 krpm to recover some of the lost open circuit voltage.

The magnet eddy current loss simulation was performed in two stages. The skin depth of the magnets at the nominal operating point is approximately 10 mm, which is larger than the magnet thickness of 3 mm. Full flux penetration is assumed. The AC flux swing in the magnets is first found by performing a 2D FEA simulation sweep of the magnet flux density vs rotor angle. The flux density at the center point of the magnet is extracted as the rotor angle is swept. Due to the 3D geometry of the magnets, the eddy currents are not easy to estimate using analytical formulas. A separate 3D simulation was performed with one magnet. The same AC flux swing as found previously was enforced throughout the entire magnet, and the losses were extracted. The eddy currents inside the magnet do not significantly alter the flux distribution, allowing the separation of flux density and loss simulations to be a good approximation. The surface plot of the losses can be seen in Figure 3.14. The total magnet eddy loss of the machine at the nominal operating point is estimated to be 18 W. A summary of predicted and experimentally estimated losses at the 8 krpm operating point can be seen in Table 3.3.

For performance evaluations, 2D magnetostatic simulations were performed to extract
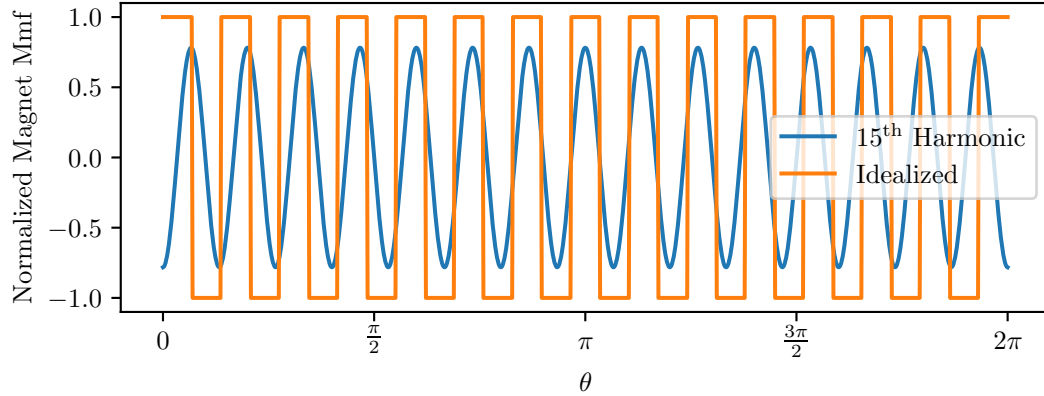
Figure 3.13: Idealized 29 magnet mmf pattern and its 15th harmonic. The amplitude of the 15th harmonic is roughly 63% that of the 15th mmf harmonic generated by a 30 magnet rotor.
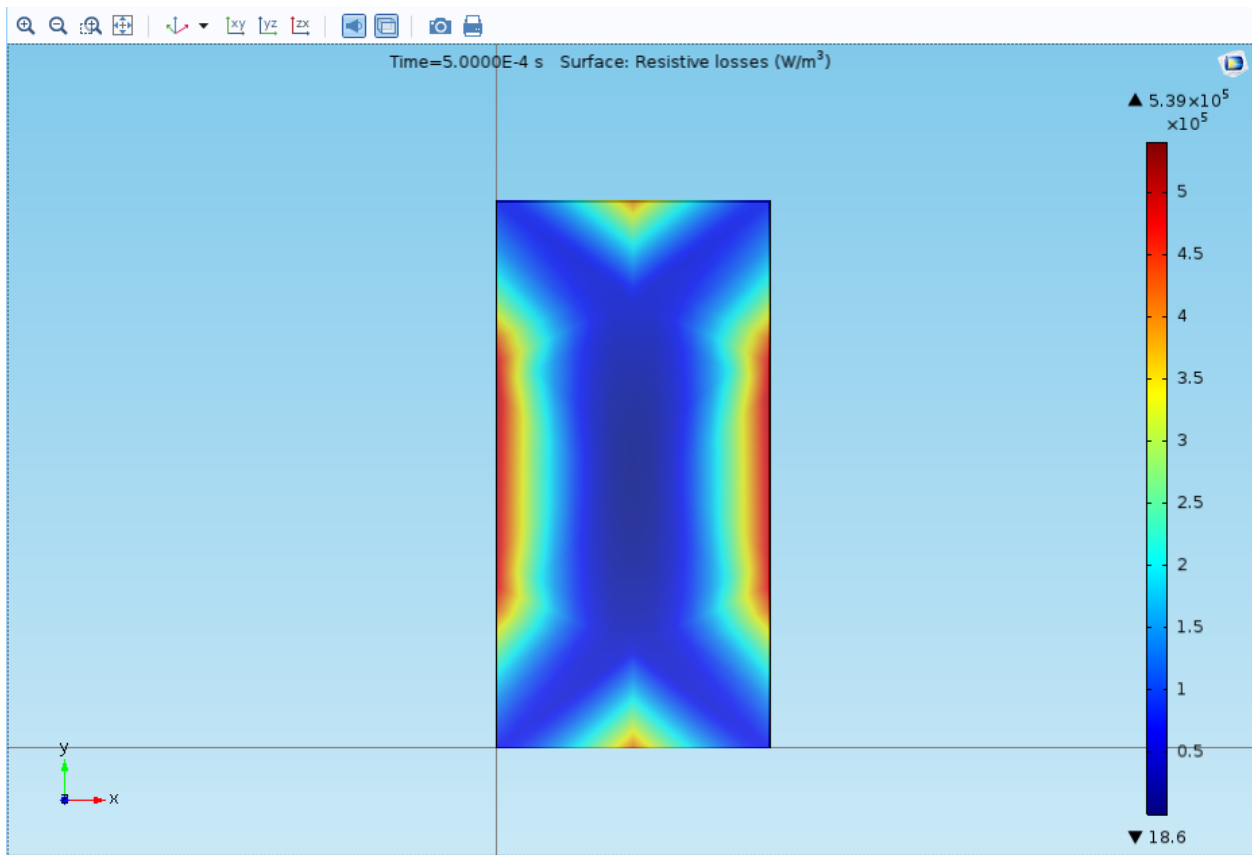
Figure 3.14: 3D FEA simulation of magnet losses. The air gap facing side of the magnet is shown.
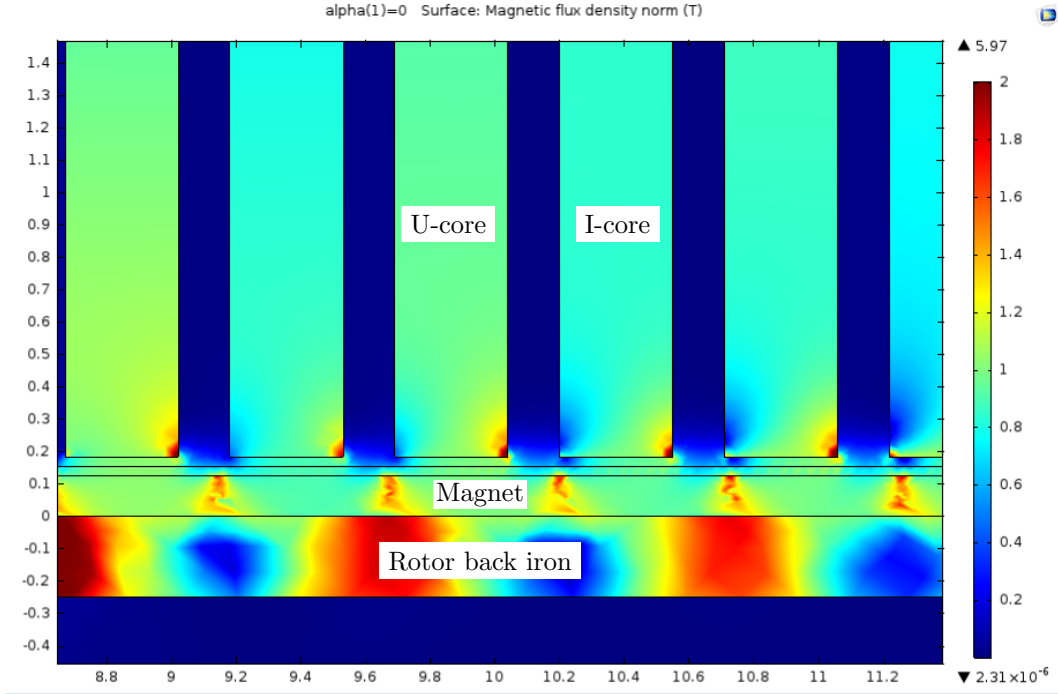
Figure 3.15: 2D FEA simulation of 30 stator cores and 29 magnets. Lack of periodicity necessitates simulating the entire geometry.

magnet flux linkage, magnet operating point, and cogging. The entire machine geometry was simulated due to the lack of periodicity. A section of the simulation can be seen in Figure 3.15. All magnets in the simulation were modeled as a single solid rectangle, and the magnetization pattern for the rectangle was defined separately as a function of the horizontal (azimuthal) coordinate. The simulation proved to be a useful test bed for different magnet arrangements, as the only change necessary was the magnetization function and not the geometry.

3.6 Experimental Results

The TFM prototype with 29 magnets on each circumferential ring was constructed. The prototype construction is detailed in Section 6. Its winding parameters and loss are characterized in this section.

3.6.1 Prototype Machine Parameters

The constructed rotating transformer's parameters were measured and compared to their designed values. The electrical parameters of interest are the winding self and mutual inductances, winding resistances, and the magnet flux linkage. Also of interest are the primary referred leakage and magnetizing inductances for direct substitution into the transformer cantilever circuit model. A four terminal LCR meter was used to measure the self inductances, mutual inductances, and resistances at an excitation frequency of 1 kHz, the closest

Table 3.2: Machine Winding Parameters

Parameter	Design Value	Measured Value
Resistance	$\begin{bmatrix} 9.28 & 0 & 0 \\ 0 & 9.28 & 0 \\ 0 & 0 & 9.28 \end{bmatrix} m\Omega$	$\begin{bmatrix} 10.2 & 0 & 0 \\ 0 & 9.8 & 0 \\ 0 & 0 & 10.8 \end{bmatrix} m\Omega$
Inductance	$\begin{bmatrix} 312 & \text{N/A} & \text{N/A} \\ \text{N/A} & 312 & \text{N/A} \\ \text{N/A} & \text{N/A} & 312 \end{bmatrix} \mu H$	$\begin{bmatrix} 261 & 237 & 236 \\ 237 & 224 & 220 \\ 236 & 220 & 225 \end{bmatrix} \mu H$
Primary referred leakage inductance (winding 2)	5 μH	6.1 μH
Primary referred magnetizing inductance (winding 2)	307 μH	217.9 μH
Magnet flux linkage (winding 2, peak)	5.41 mWb	3.35 mWb

frequency to the 2 kHz operating point frequency with which the LCR meter is able to make a measurement.

The magnet flux linkage was found by integrating back emf measurements. The simulated and measured magnet flux linkage for winding 2 vs rotor angle is plotted in Figure 3.16. The flux linkage for winding 3 is identical, and that for winding 1 is scaled by 13/12 according to the turns ratio. Both simulated and measured waveforms agree in terms of harmonic content, showing a dominant fundamental harmonic and very little higher order harmonics. The difference in magnitude is attributed in part to the unintentional circumferential skewing of magnets as described in Section 6.1.2, which is estimated to account for 40% of the difference according to simulation. The remaining difference can be attributed to the mechanical tolerances of the cut cores. The tolerances increased the average air gap beyond the design specification of 1 mm. A summary of the electrical parameters is given in Table 3.2.

3.6.2 Machine Loss Analysis

A spin down test was conducted where the machine was spun up to 8.9 krpm and then allowed to spin down with the inverter disabled open circuit. The DC bus was left powered at a voltage higher than the back emf peak voltage in order to prevent body diode conduction. The back emf was measured, from which the mechanical frequency was extracted using the Hilbert transform. The Hilbert transform yields a signal that is 90 degrees phase shifted from the back emf waveform. A new complex signal can be composed with the result of the transform as the complex part and the original as the real part. The desired instantaneous back emf phase and magnitude may be extracted from the new complex signal.
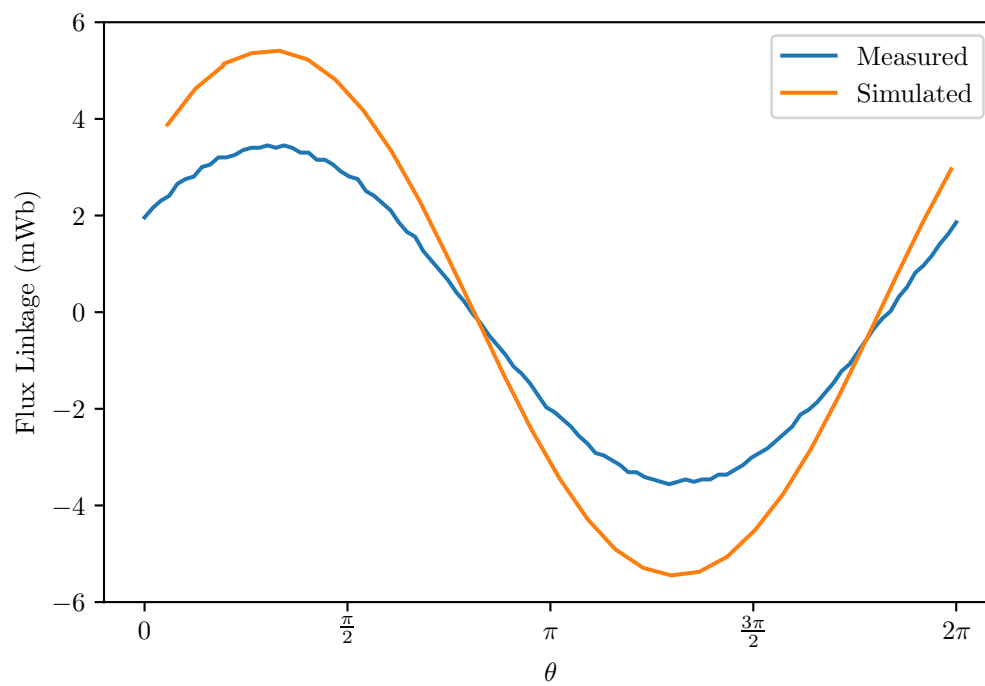
Figure 3.16: Machine permanent magnet flux linkage to winding 2 vs rotor angle. The period is equal to one pole pair pitch.

The losses can be calculated as:

$$P_{loss} = J\omega_m \frac{d\omega_m}{dt} \tag{3.14}$$

where J is the rotor's polar moment of inertia and ω_m is the mechanical speed. There is no current flowing in the stator windings, so the losses consist only of:

1. Bearing drag

2. Magnetic core loss

3. Windage drag

The bearing drag is estimated from its total frictional moment given as:

$$M = M_{rr} + M_{sl} \tag{3.15}$$

where M_{rr} is the rolling frictional moment and M_{sl} is the sliding frictional moment. The rolling frictional moment is largely dependent on the loading, while the sliding frictional moment is largely dependent on the lubrication conditions. The parameters were found from data provided by bearing manufacturer SKF. For a 6005 bearing with 150 N of axial preload corresponding to the bottom bearing, the following parameters were given: $M_{rr} = 2.55\ Nmm$ and $M_{sl} = 2.32\ Nmm$ for a total frictional moment of $M = 4.88\ Nmm$ [43]. The top bearing has an axial preload of 250 N with the following parameters given: $M_{rr} = 3.15\ Nmm$ and $M_{sl} = 4.41\ Nmm$ for a total frictional moment of $M = 7.57\ Nmm$. The temperature is assumed to be 20 C.

The magnetic core loss consists of losses in both the stator and rotor. In the stator the losses occur in the cut cores, while on the rotor the losses occur in the magnets and rotor laminations. The estimation of those losses are described in Section 3.4.1.

The windage drag is crudely estimated by assuming planar Coutte air flow at both the rotor inner and outer diameters. The results most likely underestimate the loss at the rotor inner diameter, where the Reynolds number was estimated to be around 6500 at the ring of magnets. The machine began producing a ringing noise starting at speeds around 6 krpm, corresponding to a Reynolds number of around 5000. It is hypothesized that the onset of turbulent air flow caused the noise. Once the air flow is turbulent, the windage loss is difficult to estimate and also much higher than that for laminar flow.

The predicted losses at 8 krpm are summarized in Table 3.3. The predicted vs measured losses are shown in Figure 3.17. As can be seen in the table and figure, the measured losses were around three times that of the designed value. In addition to the windage losses, the stator core losses are suspected to also be underestimated. It is not uncommon to measure higher cores losses than those given in manufacturer datasheets when waveforms do not match the sinusoidal conditions used for characterization. One example found core losses up to four times higher than expected [44].

Table 3.3: Machine Loss Summary at 8 krpm

Parameter	Design Value	Percentage of Measured Loss
Bearing drag	10.4 W	7.3%
Magnetic core loss	35 W	25%
Stator core loss	17 W	
Magnet eddy loss	18 W	
Rotor lamination loss	<1 W	
Windage drag	4.56 W	3.2%
Total predicted loss	50 W	35%
Measured loss	142 W	100%
Remaining loss	92 W	65%
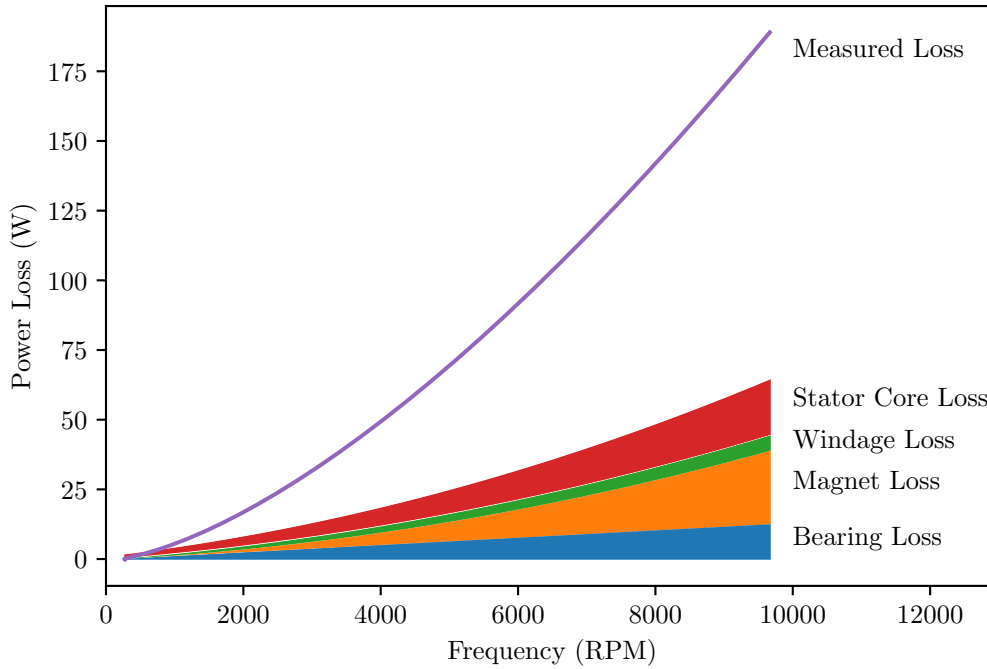
Figure 3.17: Spindown losses.

4 Mechanical Suspension

4.1 Mechanical Suspension Design

A compliant mechanical housing was designed in order to prevent excess vibration. A 2D Jeffcott rotor model seen in Figure 4.1 was adopted to analyze the dynamics. Only the lateral dynamics are considered. The analysis follows that presented in [30]. Parameter $\boldsymbol{y}$ represents the center of the axle, $\boldsymbol{r}$ the radius of the axle's displacement, $\boldsymbol{e}$ the rotor eccentricity, $\boldsymbol{z}$ the rotor center of mass, and Ω the speed of rotation.

The center of the axle $\boldsymbol{y}$ and the rotor center of mass are related by the eccentricity $\boldsymbol{e}$ as given by

$$\boldsymbol{z} = \boldsymbol{y} - \boldsymbol{e} \tag{4.1}$$

The dynamics are governed by

$$m\ddot{\boldsymbol{z}} + d\dot{\boldsymbol{y}} + k\boldsymbol{y} = 0 \tag{4.2}$$

where m is the mass of the rotor and stator, d the system damping, and k the system stiffness.

Substituting Equation 4.1 into Equation 4.2 while assuming constant angular velocity yields two uncoupled scalar differential equations that can written in the vector form

$$m\ddot{\boldsymbol{y}} + d\dot{\boldsymbol{y}} + k\boldsymbol{y} = m\Omega^2 \boldsymbol{e} \tag{4.3}$$

Solving the differential equations gives

$$\boldsymbol{y} = re^{\mathbf{J}\theta} \tag{4.4}$$

where

$$r = \frac{m\Omega^2}{\sqrt{(k - m\Omega^2)^2 + (d\Omega)^2}} e = Ve \tag{4.5}$$

$$\theta = \Omega t + \epsilon \tag{4.6}$$

$$\epsilon = \tan^{-1}\frac{d\Omega}{k - m\Omega^2} \tag{4.7}$$

$$e^{\mathbf{J}\theta} = \begin{bmatrix} \cos\theta \\ \sin\theta \end{bmatrix} \tag{4.8}$$

Generally, the solutions to the second order ordinary differential equations are underdamped. The relationship between the gain $V = r/e$ and the machine frequency Ω resembles a high pass filter with natural frequency $\omega_n = \sqrt{k/m}$ and high frequency gain of one.

A compliant housing has several advantages in this application. First, the system's resonant frequency will be low so that the machine will not encounter it during normal operation. Secondly, the displacement amplitude will remain fixed over a wide frequency range around the operating point, a desirable property in this application where there is a
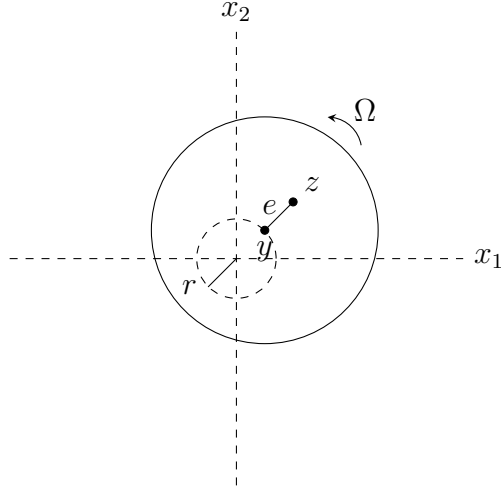
Figure 4.1: Jeffcott rotor dynamical system. Parameter y represents the center of the axle, r the radius of the axle's displacement, e the rotor eccentricity, z the rotor center of mass, and Ω the speed of rotation.

120 Hz speed ripple present. Finally, the restoring forces in the system will be small at the operating speed.

A polyurethane part provides the system's main source of damping and compliance. The desired compliance was obtained by dimensioning it and selecting an appropriate material hardness, which is related to its elastic modulus. Its compliance can be approximated as

$$k = \frac{GA}{l} \tag{4.9}$$

where G is the shear modulus, A is the cross sectional area, and l is the length.

The shear modulus is available from datasheets on the BASF website [31]. The material's damping properties are also readily available from the data sheet.

4.2 Experimental Results

The implementation and construction of the mechanical housing can be seen in Section 6.1.3. The mechanical system's designed and measured parameters including natural frequency and damping of both lateral and diametric modes are summarized in Table 4.1. The diametric mode indicates the dynamics of the rotor about an axis that is diametric to the rotor, similar to the roll or pitch mode in aircraft.

To investigate the properties of the constructed mechanical housing, a two axis accelerometer was attached to the axle. The rotor was excited with an impulse, and the acceleration response was measured. The displacement was found through integration. The impulse response of the mechanical system can be seen in Figure 4.2.

The rotor accelerations were also measured while driving the machine at constant speeds. Figure 4.3 shows the measured accelerations at 8 krpm. The green waveform is the secondary AC square wave voltage, and the yellow waveform is the voltage output from one axis of
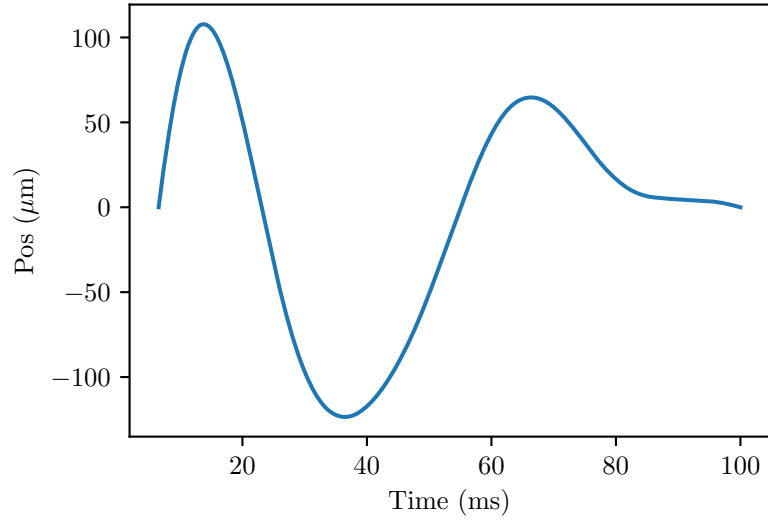
Figure 4.2: Impulse response of mechanical housing showing a resonance frequency of 19 Hz.

Table 4.1: Machine Mechanical Parameters

Parameter	Design Value	Measured Value
Lateral natural frequency	20 Hz	19 Hz
Lateral Q	10	6.15
Polar moment of inertia	0.041 kg m^2	0.046 kg m^2
Diametric natural frequency	60 Hz	53 Hz
Diametric Q	N/A	65.6
Diametric moment of inertia	N/A	0.101 kg m^2
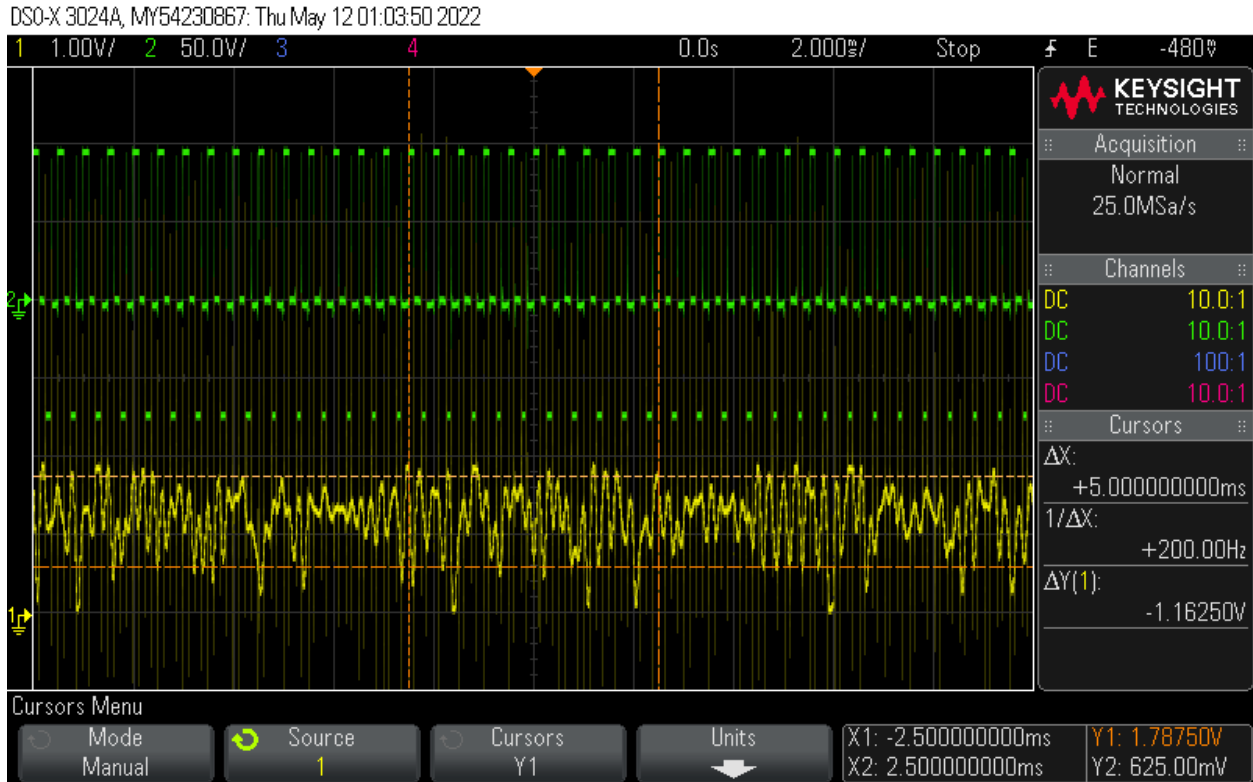
Figure 4.3: Accelerations at 8 krpm are dominated by higher order harmonics. The green waveform is the secondary side applied square wave voltage, and the yellow waveform is the voltage output from one axis of the accelerometer. The accelerometer sensitivity is 100 mV/g.

the accelerometer. The accelerometer sensitivity is 100 mV/g. The scope capture shows approximately 34 electrical periods, which is a little more than two complete mechanical revolutions. There is no noticeable mechanical fundamental harmonic in the accelerometer output. Instead, the accelerations are dominated by higher order harmonics generated by other sources such as cogging or current time harmonics. The low fundamental harmonic indicates that the system is past resonance and in the constant displacement regime.

5   System Control

This section presents the system's control design. The system has single phase quantities, resulting in more challenging control than in 3 phase systems. In traditional 3 phase systems, a rotating vector in $\mathbb{R}^2$ can easily be constructed using the Clarke transform [40]. Projecting the vector onto a set of orthogonal rotating axes (the Park transform [41]) results in DC steady state quantities, also known as a phasor. In single phase systems, the phasor cannot be so easily constructed.

Existing works have derived a quadrature phase from the single phase measurement to reconstruct the phasor. This can be accomplished in numerous ways. In [33, 35] the signal is delayed in time by 90° in software (transport delay). An all pass filter is used to implement a 90° phase delay in [34]. Another popular method is the second-order generalized integrator (SOGI), which consists of a bandpass filter tuned to the desired frequency. The quadrature phase is derived from an internal signal that is the integral of the bandpass filter output. An in-depth analysis of the filter and its dynamics can be found in [38]. In [32] differentiation of the signal is used to provide the quadrature phase instead of integration. It is important to note that for this application the frequency is not constant. As the frequency varies, all of these methods can introduce additional dynamics into the control system.

The measured signal can also be treated as the sum of forward and backward rotating vectors in $\mathbb{R}^2$ in which the first element is the measured signal and the second element is zero. With a null quadrature component of the signal, directly projecting the single phase signal onto the set of orthogonal rotating axes results in an undesired second harmonic component. The second harmonic component is the projection of the backward rotating component onto the axis. It is possible to remove the second harmonic through filtering, and this method is known as the power PLL. A detailed overview of single phase PLLs can be found in [42].

A reference frame transformation that extracts the phasor with no filtering computations is presented in this section. The method is based off the power PLL concept. Then a motor circuit model is shown, from which the phasor dynamics are derived. A sensorless motor controller is designed and implemented using the dynamic phasors. The small signal performance is analyzed, and the experimental results are presented. Finally the controller for realizing the system 120 Hz power balancing and holdup energy is shown.

5.1   Single Phase Motor Control Using Dynamic Phasors

The single phase sensorless motor controller operates using the phasor representations of all system signals. The controller relies on the reference frame transform that converts the measured single phase motor current into its phasor representation.

5.1.1   Single Phase Reference Frame Transform

The single phase reference frame transform is implemented in the digital domain and relies on sampling at precise instants to extract the phasor. A linear transformation that is used
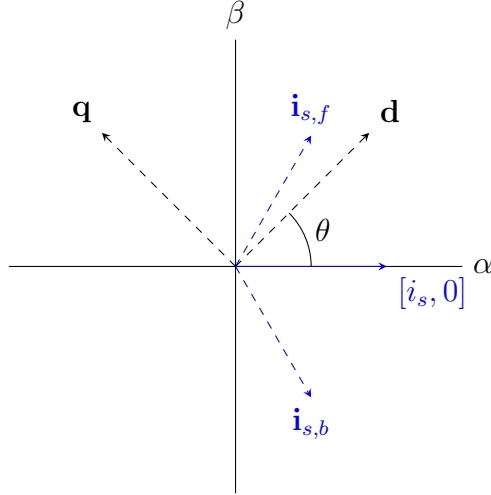
Figure 5.1: Drawing showing the stationary frame α-β axes, dq axes, and the measured current signal i_s. At steady state the dq axes and $\mathbf{i}_{s,f}$ vectors rotate forward synchronously at the electrical frequency. The vector $\mathbf{i}_{s,b}$ rotates backwards at the electrical frequency. The angle θ represents the angle between the dq axes and the stationary α axis.

to lift the single phase quantities in $\mathbb{R}$ into the $\mathbb{R}^2$ domain is defined as:

$$f : \mathbb{R} \to \mathbb{R}^2$$
$$f(x) = \begin{bmatrix} x & 0 \end{bmatrix}^T \tag{5.1}$$

The vector $f(i_s) = [i_s, 0]^T$ is projected onto a pair of orthogonal dq axes, where i_s is the measured current signal. The chosen orthogonal dq axes rotate synchronously at the electrical frequency defined by the applied inverter voltage, and the q axis is aligned with the inverter voltage phasor. This projection can be seen as applying independently to the forward and backward rotating components of the single phase signal through linearity. In the dq rotating reference frame it results in a static (DC) phasor superimposed with another dynamic phasor rotating backwards at twice the electrical frequency. The static phasor is the forward rotating component of the signal, and the dynamic one is the backward rotating component.

The sampling instants can be chosen so that removing the second harmonic component involves no computations. If the sampling takes place four times a period when the d axis is at angles:

$$\theta = [0, \pi/2, \pi, 3\pi/2] \tag{5.2}$$

with respect to the stationary alpha-beta axes, then the projection onto the d and q axes is trivial. Figure 5.1 illustrates the dq axes, stationary frame axes, and the vector representation of the measured signal $\mathbf{i_s}$.

The current i_q that is the projection of the current vector onto the q axis is derived below. The d axis current i_d may be found in a similar process. Without loss of generality let the

q axis coordinates and current be modeled as

$$\mathbf{q} = [-\sin(\theta), \cos(\theta)] \tag{5.3}$$

$$\mathbf{i_s} = [i_s(\theta), 0] \tag{5.4}$$

$$= \mathbf{i}_{s,f} + \mathbf{i}_{s,b} \tag{5.5}$$

where $\mathbf{q}$ is the instantaneous vector representation of the q axis in the stationary frame, $\mathbf{i_s}$ is the instantaneous vector representation of the measured current signal, $\theta = \omega_e t + \phi$, ω_e is the electrical frequency, ϕ is an arbitrary angle, and $\mathbf{i}_{s,f}$, $\mathbf{i}_{s,b}$ are forward and backward traveling vectors respectively that sum to $\mathbf{i}_s$.

The current i_s can be decomposed into its even and odd harmonics over one electrical period $2\pi/\omega_e$ and can be represented as

$$i_s(\theta) = i_{s,e}(\theta) + i_{s,o}(\theta) \tag{5.6}$$

where $i_{s,e}$ are the even harmonics of the signal and $i_{s,o}$ are the odd harmonics of the signal. Projecting the current $\mathbf{i_s}$ onto the q axis yields

$$\mathbf{i_p} = <\mathbf{i_s}, \mathbf{q}> \mathbf{q} = i_s(\theta)\mathbf{q}[0]\mathbf{q} = -i_s(\theta)\sin(\theta)\mathbf{q} = i_p(\theta)\mathbf{q} \tag{5.7}$$

where $\mathbf{i_p}$ is the projected current containing both a DC and second harmonic component, $< \cdot >$ represents the dot product, $\mathbf{q}[0]$ represents the first component of the q axis, and i_p is the dot product between $\mathbf{i}_s$ and $\mathbf{q}$.

At the $\pi/2$ sampling instances, the value of the projection i_p is equal to

$$i_p(0) = 0 \tag{5.8}$$

$$i_p\left(\frac{\pi}{2}\right) = -i_s\left(\frac{\pi}{2}\right) \tag{5.9}$$

$$i_p(\pi) = 0 \tag{5.10}$$

$$i_p\left(\frac{3\pi}{2}\right) = i_s\left(\frac{3\pi}{2}\right) \tag{5.11}$$

The DC component of the projected current i_p can then be calculated directly to be:

$$
\begin{aligned}
i_q &= \frac{1}{4}(i_p(\pi/2) + i_p(3\pi/2)) \\
&= \frac{1}{4}(-i_s(\pi/2) + i_s(3\pi/2)) \\
&= \frac{1}{4}(-i_{s,e}(\pi/2) - i_{s,o}(\pi/2) + i_{s,e}(\pi/2) - i_{s,o}(\pi/2)) \\
&= -\frac{1}{2}(i_{s,o}(\pi/2)) = \frac{1}{2}(i_{s,o}(3\pi/2)) \tag{5.12}
\end{aligned}
$$

where the symmetrical / anti-symmetrical properties of even and odd harmonics were used. Figure 5.2 depicts the timing diagram of the sampling showing the first element of the q axis, the measured current, and the magnitude of the projected current.
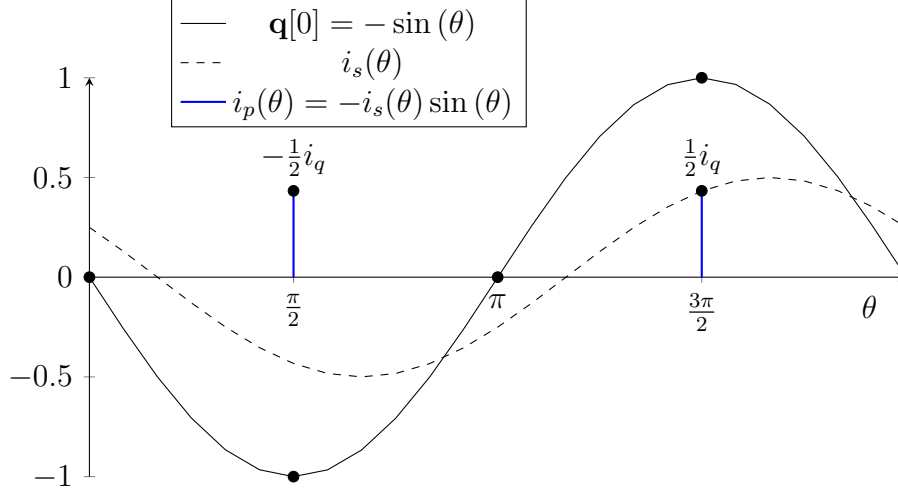
Figure 5.2: Time domain waveforms of the single phase reference transform by sampling at four times the motor frequency. The legend entry $\mathbf{q}[0]$ indicates the first element of the q axis vector, and i_s is the measured current. Mutiplying the two and choosing appropriate sampling instants yield a clear DC component that represents the i_q current.

Equation 5.12 implies that only one sample at the correct timing is needed to extract the direct or quadrature component of the signal. In the above example i_q may be found by sampling at the angles $\pi/2$ and $3\pi/2$. The i_d current may be found by sampling at the angles 0 and π. This represents significant computational savings over more conventional methods mentioned earlier. Additionally no dynamics are added into the system. There are two such correct timings in one electrical period. This allows the controller to resolve the dq quantities and respond accordingly twice per electrical period.

The aliasing of all odd harmonics onto the zero normalized frequency is one weakness of the described reference transform. For this motor drive application the conditions are favorable for the first current harmonic to dominate given the low pass filtering characteristic from the winding inductance and the dominant first harmonic in the source and back emf voltages.

5.1.2 Motor Model and Electrical Dynamics

The single phase permanent magnet motor circuit model is shown in Figure 5.3. The winding resistance R, winding self inductance L, and back emf V_e are modeled. The stator voltage is V_s. The stator flux λ_s is defined by integrating the stator voltage minus the voltage drop across the winding resistance. The single phase reference frame transformation in Section 5.1.1 is applied to the measured current signal to obtain its d and q quantities.

The electrical dynamics are described in the synchronous reference frame, where the q

axis aligned with the stator voltage. The large signal dynamics are found as:

$$
\frac{d}{dt}
\begin{bmatrix} \lambda_d \\ \lambda_q \\ \theta \end{bmatrix}
=
\begin{bmatrix} -\frac{R}{L} & \omega_e & 0 \\ -\omega_e & -\frac{R}{L} & 0 \\ 0 & 0 & 0 \end{bmatrix}
\begin{bmatrix} \lambda_d \\ \lambda_q \\ \theta \end{bmatrix}
+
\begin{bmatrix} 0 \\ V_q \\ \omega_e \end{bmatrix}
+
\begin{bmatrix} \frac{R\lambda_r \cos(\theta)}{L} \\ -\frac{R\lambda_r \sin(\theta)}{L} \\ -15\omega_m \end{bmatrix}
\tag{5.13}
$$

where θ is the electrical angle between the stator and back emf voltages, λ_r is the magnet flux linkage, and ω_m is the machine's mechanical frequency. The factor of 15 in front of ω_m arises from the machine's pole pair count. The output of the system in the synchronous frame is the current, which is equal to:

$$
\begin{bmatrix} i_d \\ i_q \end{bmatrix}
=
\begin{bmatrix} \frac{1}{L} & 0 & 0 \\ 0 & \frac{1}{L} & 0 \end{bmatrix}
\begin{bmatrix} \lambda_d \\ \lambda_q \\ \theta \end{bmatrix}
+
\begin{bmatrix} -\frac{\lambda_r \cos(\theta)}{L} \\ \frac{\lambda_r \sin(\theta)}{L} \end{bmatrix}
\tag{5.14}
$$

To convert from the vector quantities in $\mathbb{R}^2$ into single phase quantities in $\mathbb{R}$, the dq quantities are represented in the stationary $\alpha\beta$ frame. The following linear transformation is applied to the current vector in the stationary frame:

$$
g : \mathbb{R}^2 \to \mathbb{R} = \mathbf{x}[0]
$$
$$
g(\mathbf{x}) = \begin{bmatrix} 1 & 0 \end{bmatrix} \mathbf{x}
\tag{5.15}
$$

The single phase quantity current output is the α component of the current vector.

The mechanical dynamics are modeled separately as:

$$
\frac{d}{dt}\omega_m = -\frac{B}{J}\omega_m + \frac{1}{J}\tau_e
\tag{5.16}
$$

where B is a viscous drag coefficient, J is the rotor's polar moment of inertia, and τ_e is the electrical torque. The electrical dynamics are treated as much faster than the mechanical dynamics. As such, the mechanical frequency ω_m is treated as a constant for purposes of designing the controller. A rigorous analysis to justify such an assumption may be performed using singular perturbation theory. A detailed treatment of singular perturbation theory can be found in [36].

The electrical dynamics are then linearized, with the inputs of the system being electrical frequency ω_e and voltage magnitude V_q. The small signal quantities are denoted by the hat symbol (ˆ), while the operating point values are denoted by the overhead bar symbol (¯). The small signal operating points can be seen in Table 5.1. The linearized small signal

Parameter	Value
$|V_s|$	$50V$
i_d	$15.2\ A$
i_q	$10\ A$
λ_d, λ_r	$4\ mWb$
λ_q	$0\ mWb$
θ	$31.7°$
ω_e	$2\pi(2000)\ rad/s$

dynamics are calculated to be:

$$
\frac{d}{dt}\begin{bmatrix} \hat{\lambda}_d \\ \hat{\lambda}_q \\ \hat{\theta} \end{bmatrix} = \begin{bmatrix} -\frac{R}{L} & \bar{\omega}_e & -\frac{R\lambda_r \sin(\bar{\theta})}{L} \\ -\bar{\omega}_e & -\frac{R}{L} & -\frac{R\lambda_r \cos(\bar{\theta})}{L} \\ 0 & 0 & 0 \end{bmatrix} \begin{bmatrix} \hat{\lambda}_d \\ \hat{\lambda}_q \\ \hat{\theta} \end{bmatrix} + \begin{bmatrix} 0 & \bar{\lambda}_q \\ 1 & -\bar{\lambda}_d \\ 0 & 1 \end{bmatrix} \begin{bmatrix} \hat{V}_q \\ \hat{\omega}_e \end{bmatrix} \tag{5.17}
$$

$$
\begin{bmatrix} \hat{i}_d \\ \hat{i}_q \end{bmatrix} = \begin{bmatrix} \frac{1}{L} & 0 & \frac{\lambda_r \sin(\bar{\theta})}{L} \\ 0 & \frac{1}{L} & \frac{\lambda_r \cos(\bar{\theta})}{L} \end{bmatrix} \begin{bmatrix} \hat{\lambda}_d \\ \hat{\lambda}_q \\ \hat{\theta} \end{bmatrix} \tag{5.18}
$$

The operating point is chosen where the stator flux magnitude is matched to that of the rotor. The equilibrium phasor diagram can be seen in Figure 5.4. For this operating point the current bisects the stator and back emf voltages assuming the inductive impedance dominates. Operating at unity power factor on the inverter side enables the use of the lowest rated VA switches, while operating at unity power factor on the motor side results in the highest torque per amp. These conditions are not simultaneously achievable, and a matched flux level represents a balance between the two. The remaining values are calculated assuming a scenario where 250 W of power is being delivered to the machine at 8 krpm.

The transfer functions are then found as:

$$
\begin{bmatrix} \tilde{i}_d \\ \tilde{i}_q \end{bmatrix} = \begin{bmatrix} H_{11} & H_{12} \\ H_{21} & H_{22} \end{bmatrix} \begin{bmatrix} \tilde{V}_q \\ \tilde{\omega}_e \end{bmatrix} \tag{5.19}
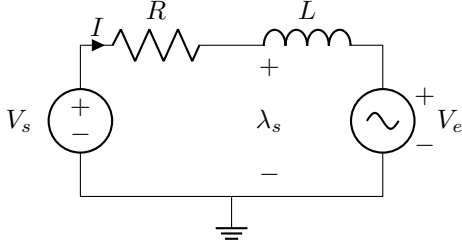$$

Figure 5.3: Permanent magnet motor circuit model.
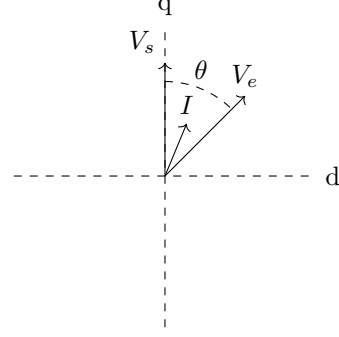
Figure 5.4: Equilibrium phasor diagram assuming the winding inductive impedance dominates.

where the tilde symbol (˜) denotes the variable in the s-domain, and:

$$H_{11} = \left(\frac{\bar{\omega}_e}{L}\right)\frac{1}{D_H} \tag{5.20}$$

$$H_{12} = \frac{L(\bar{\lambda}_q + \lambda_r \sin\bar{\theta})s^2 + (R\bar{\lambda}_q + R\lambda_r \sin\bar{\theta} - \bar{\omega}_e L\bar{\lambda}_d)s + \bar{\omega}_e\lambda_r(\bar{\omega}_e L \sin\bar{\theta} - R\cos\bar{\theta})}{sD_H} \tag{5.21}$$

$$H_{21} = \left(\frac{R}{L^2}\right)\frac{\left(1 + \frac{s}{\left(\frac{R}{L}\right)}\right)}{D_H} \tag{5.22}$$

$$H_{22} = \frac{N_{22}}{sD_H} \tag{5.23}$$

$$N_{22} = L(\lambda_r \cos\bar{\theta} - \bar{\lambda}_d)s^2 + (-R\bar{\lambda}_d - \bar{\omega}_e L\bar{\lambda}_q + R\lambda_r \cos\bar{\theta})s$$
$$+ \lambda_r(R\bar{\omega}_e \sin\bar{\theta} + 2(R^2/L)\cos\bar{\theta} + \bar{\omega}_e^2 L \cos\bar{\theta})$$

$$D_H = s^2 + 2\frac{R}{L}s + \left(\frac{R}{L}\right)^2 + \bar{\omega}_e^2 \tag{5.24}$$

The Bode plot of the transfer functions can be found in Figure 5.5. The transfer functions mirror those obtained from standard 2 axis methods used with conventional three phase systems, as found in [37].

Independent scalar feedback is used to control the 2x2 multiple-input multiple-output (MIMO) system in Equation 5.19. A general treatment of this 2x2 MIMO system is given in [37], where the small signal conditions for stability through independent scalar feedback are established according to the small gain theorem. The system is guaranteed to be stable if:

$$\max_{0 < j\omega < \infty} \left(|\Delta| \cdot |T_1| \cdot |T_2|\right) < 1 \tag{5.25}$$

where $\Delta = \frac{H_{12}H_{21}}{H_{11}H_{22}}$ and $T_1 = \tilde{i}_d/\tilde{i}_{d,ref}$, $T_2 = \tilde{i}_q/\tilde{i}_{q,ref}$ are the respective decoupled closed loop transfer functions involving the two diagonal input-output pairs assuming $H_{12} = H_{21} = 0$.
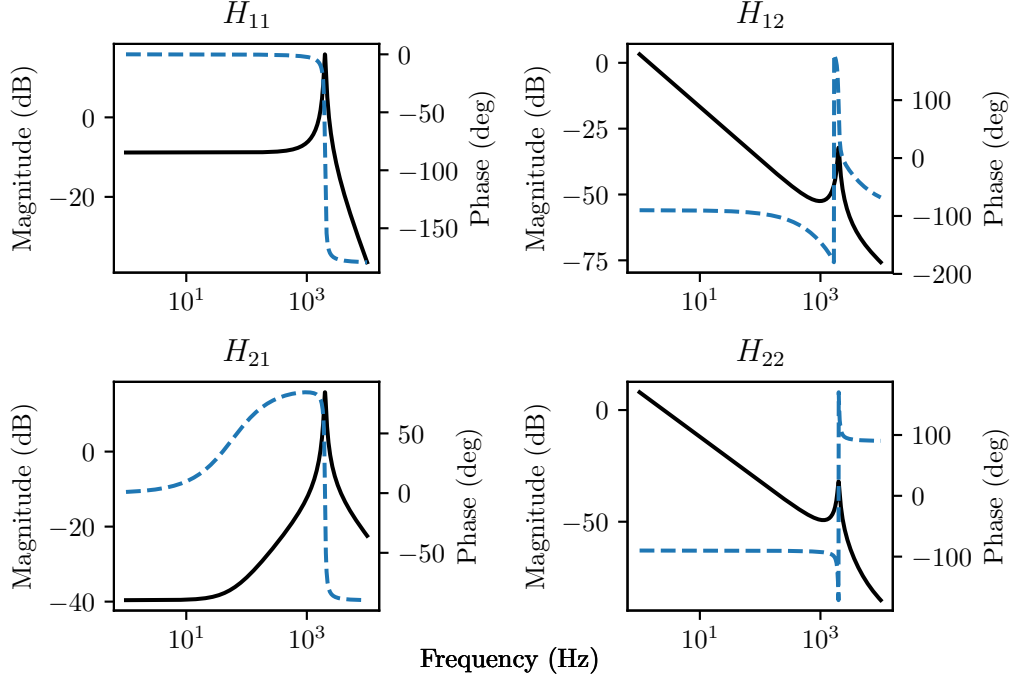
Figure 5.5: Open loop transfer functions.

Table 5.2: Compensator Gains

	Parameter	Value
$i_{d,err}$	k_p	0.006
	k_i	251
$i_{q,err}$	k_p	6.3
	k_i	25

The diagonal input-output pairs are (V_q, i_d) and (ω_e, i_q), and the off-diagonal pairs are (ω_e, i_d) and (V_q, i_q). The magnitude of the Δ term represents the relative strengths of the off-diagonal vs diagonal input-output pairs. If $|\Delta|$ is small, then Equation 5.25 implies that the 2x2 MIMO system may be stabilized by designing the appropriate compensators assuming two independent scalar systems. Furthermore, it is shown that if $|\Delta|$ is small, then the coupled closed loop transfer functions for the diagonal systems will be approximately equal to their decoupled ones. The plots of $|\Delta|$, $|T_1|$, $|T_2|$, and $|\Delta| \cdot |T_1| \cdot |T_2|$ can be seen in Figure 5.6. The gains of the compensators are given in Table 5.2. As can be seen, Equation 5.25 holds.

Following those results, the system is treated as two independent systems. The inverter voltage V_q is used to control the reactive current i_d, and ω_e is used to control the real current i_q. The control block diagram can be seen in Figure 5.7.
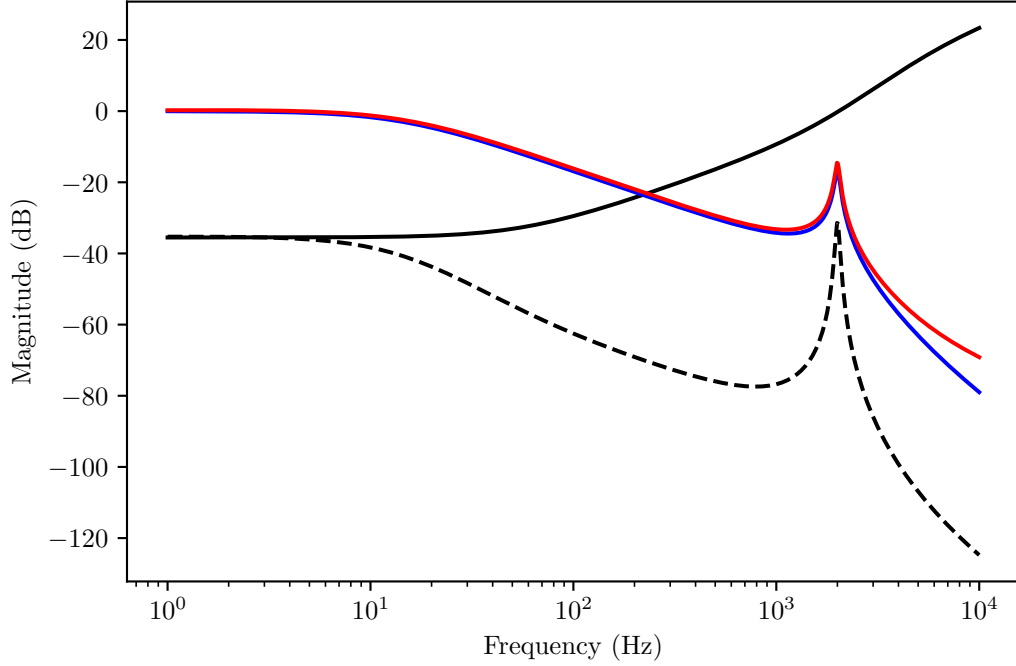
Figure 5.6: Plots of $|T_1| = \tilde{i}_d/\tilde{i}_{d,ref}$ (blue), $|T_2| = \tilde{i}_q/\tilde{i}_{q,ref}$ (red), $|\Delta| = \frac{H_{12}H_{21}}{H_{11}H_{22}}$ (solid black), and $|\Delta| \cdot |T_1| \cdot |T_2|$ (dashed black).
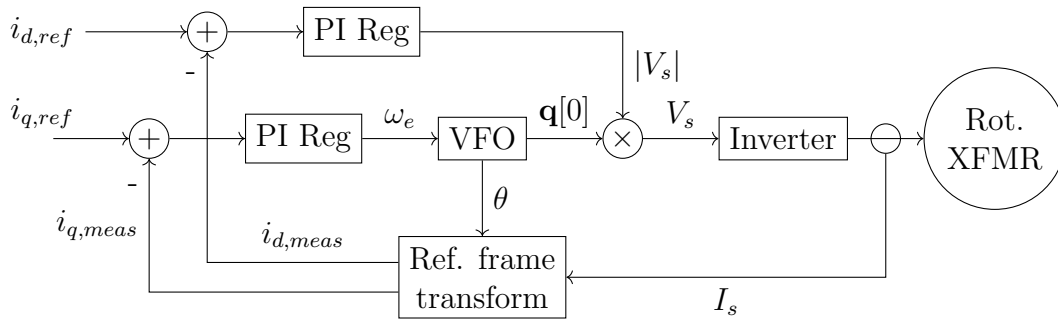
Figure 5.7: Block diagram of motor control system. The electrical frequency ω_e is used to control the motor i_q current, and the voltage magnitude $|V_s|$ is used to control the motor i_d current. The variable frequency oscillator (VFO) contains a rotating unit vector that defines the $\mathbf{d}$ axis vector. The $\mathbf{q}$ axis vector is found by rotating $\mathbf{d}$ by $+90°$. The $\mathbf{q}[0]$ output of the VFO represents the α axis component of the $\mathbf{q}$ axis vector.

5.2 Square Wave Drive

Square wave drive was chosen for its numerous advantages over pulse width modulation (PWM). A list of advantages has been given in [37] for three-phase six-step control. The motivations remain the same for single phase control, and a summary of the motivations is given below.

1. Square wave drive is able to achieve higher DC bus utilization than with PWM. PWM must modulate down the DC bus voltage to avoid duty cycle saturation. While the fundamental amplitude of three-phase six-step control is fixed, that of single phase square wave drive may be controlled through the square wave duty cycle when using an H bridge with four active switches. The result allows the use of less costly switches with lower VA ratings for a given fundamental voltage amplitude.

2. Square wave drive will have lower switching losses than PWM because the switching frequency of square wave drive is the same as the electrical frequency. The switching frequency for PWM must be much larger than the electrical frequency in order to minimize the appearance of sideband harmonics in the output.

3. Square wave waveforms produce less stator and rotor core loss than those associated with PWM [39].

5.2.1 Experimental Results

Motor Model Current Locus The range of achievable i_d, i_q currents can be plotted from Equation 5.14 and can be seen in Figure 5.8. The prototype parameters L and λ_r are substituted into the equations, yielding circles as a function of the stator flux magnitude $||\lambda_s||$. Only the left half of the circles have been drawn, corresponding to the practical operating points before pull-out. The maximum i_q current is 15 A. The electrical terminal characteristics of the transverse flux machine are identical to that of a permanent magnet machine. The current locus diagram is helpful to visualize the range of achievable currents and also the power factor at various operating points. The diagram does not include the effects of core loss.

Current Controller The sensorless control scheme was implemented as described in Section 5.1.2, and the results of a positive 0 A to 10 A $i_{q,ref}$ step and a negative 10 A to 0 A $i_{q,ref}$ step can be seen Figure 5.9. The machine was rotating at a speed of 8 krpm. The gains used are given in Table 5.2.

Due to the non-ideal implementation of the current sensor, the reactive current i_d is unable to be sampled. The reason is explained in the prototype implementation Section 6.2.1. Fortunately the intended operating point of matched stator and rotor flux levels already defines the voltage magnitude, so no i_d feedback is required. The inverter voltage magnitude is commanded to match the back emf voltage open loop.

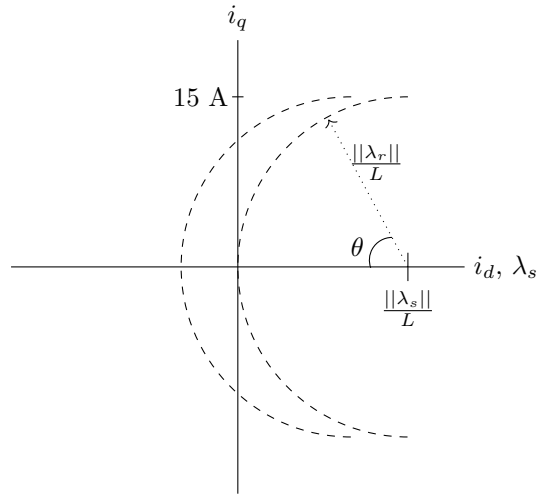Figure 5.8: Current locus diagram for the transverse flux machine. The general locus shape is that of a permanent magnet machine. The left and right arcs represent the set of currents that may be achieved when $||\lambda_s|| < ||\lambda_r||$ and $||\lambda_s|| = ||\lambda_r||$ respectively.
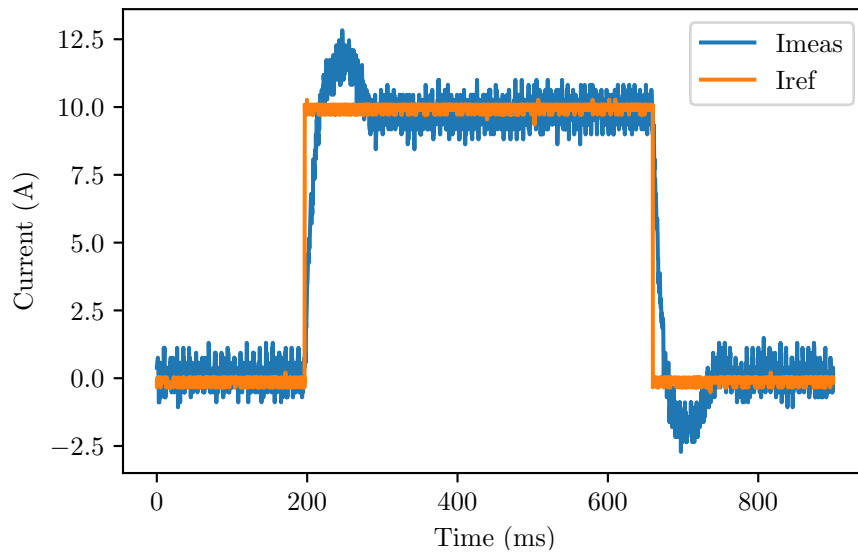

Figure 5.9: Current i_q step waveforms showing the reference current I_{ref} and measured current I_{meas}.

5.3 Multiport Controls

The system 120 Hz power balancing and holdup energy controls are presented in this section on a high level. The overall controller structures are shown using block diagrams. Both functionalities require high bandwidth regulation of the motor i_q current as explained in their respective sections. Experimental results containing system waveforms and their analysis are presented in Section 7. A block diagram of the experimental setup can be seen in Figure 7.1, and a diagram containing circuit level components can be seen in Figure 7.2.

5.3.1 DC Power Transfer

Transferring DC power from one port to another is accomplished by enforcing identical switching sequences on all ports. It then occurs naturally during the converter active states when non-zero voltage is applied to the machine. The mechanism of action is described in detail in Section 7.1 and is analogous to the power transfer mechanism in switched capacitor converters or dual active bridge converters.

5.3.2 120 Hz Power Balancing Controller

In order to achieve 120 Hz power balancing through feedback, the i_q machine current must be regulated with a bandwidth of at least 120 Hz. However, as seen in Figure 5.6, the closed loop bandwidth is only around 20 Hz. If the PI gains are increased, the feedback loop becomes unstable. To achieve i_q regulation at 120 Hz with a limited closed loop bandwidth, a feedforward path is added and can be seen in Figure 5.10.

The reference signal is split into a slowly varying component i_q and a 120 Hz component i_{120Hz}. The feedback loop alone is already sufficient to regulate i_q to follow the slowly varying component $i_{q,ref}$. Feedforward is only necessary for the 120 Hz signal i_{120Hz}. Therefore the plant transfer function H_{22} only must be inverted at 120 Hz to find the ideal feedforward gain. Assuming the feedforward path precisely inverts $H_{22}(120Hz)$, the new system output $\tilde{i}_{q,ff}$ in the s-domain can be found to be:

$$\tilde{i}_{q,ff} = \tilde{i}_{120Hz} + T_2\tilde{i}_{q,ref} \tag{5.26}$$

where the symbol ($\tilde{\ }$) denotes a variable in the s-domain and T_2 is the closed loop gain between $\tilde{i}_{q,ref}$ and $\tilde{i}_q$ with no feedforward term.

Derivation of the i_{120Hz} current can be found in Section 7.2. A first order all pass filter with the desired phase response was used to provide the phase shift for the feedforward path.

5.3.3 Holdup Energy Controller

When the power supply is disconnected, the machine supplies power to the load. Power balance is maintained by regulating the secondary DC bus voltage to a reference voltage v_{ref} by controlling the i_q current drawn from the machine. To achieve regulation, the real parts of the load and machine current must be equal. The secondary DC bus capacitor integrates the difference between the two currents, and the result is the secondary DC bus voltage. The holdup energy controller block diagram is shown in Figure 5.11. The closed loop transfer
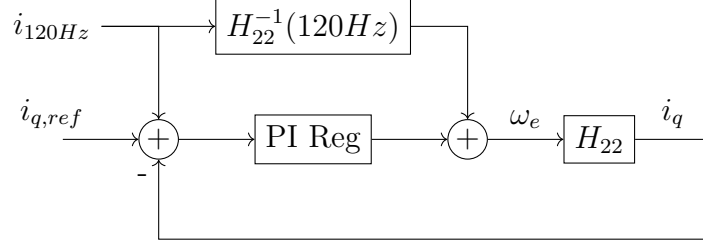
Figure 5.10: Small signal block diagram of 120 Hz power balancing control.
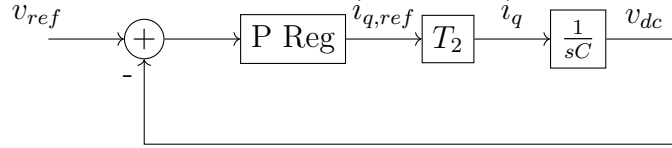
Figure 5.11: Small signal block diagram of DC bus regulation. The variable C represents the secondary DC bus capacitance.

function $T_2 = \tilde{i}_q/\tilde{i}_{q,ref}$ can be approximated as a first order unity gain low pass filter with a pole around 20 Hz. The transfer function between v_{dc} and i_q is:

$$\frac{\tilde{v_{dc}}}{\tilde{i}_q} = \frac{1}{sC} \tag{5.27}$$

where C is the secondary DC bus capacitance.

The secondary DC bus capacitance is sized only for a DC bus voltage ripple below 10% of the nominal value, where the voltage ripple results from the inverter PWM switching. It is not sized to handle the full load current. When the power source is suddenly disconnected, the secondary DC bus also drops suddenly. A high i_q control bandwidth is necessary in order to respond quickly enough and regulate the secondary DC bus before excessive voltage sag occurs.

6 Prototype Construction

This section presents the construction of the transverse flux machine, the power converter PCB circuit design, and the embedded controller software implementation.

6.1 Transverse Flux Machine Construction

The prototype construction of the transverse flux machine is described in this section. The rotor, axle, and mechanical housing have all been machined from 1045 structural steel.

6.1.1 Stator

A picture of the stator can be seen in Figure 6.1. The U-cores and I-cores used in the prototype are two complementary halves of 1 mil amorphous iron tape wound cut cores. Plastic end plates that support the cut cores axially were machined out of black Delrin. The end plates contain bosses that locate the cut cores in the desired position. The cut cores were bonded to the end plates using structural epoxy. Black plastic shields that fit on the I-core outer diameter were 3D printed from polyethylene terephthalate glycol (PETG) to mask the I-core sharp edges. Fiberglass reinforced packaging tape (not pictured) was wrapped tightly around the plastic shields to further restrain the I-cores against movement in the radial direction.

The prototype machine was built with 3 windings to simplify the assembly process. The winding structure is composed of 3 radial layers, each layer belonging to one winding. The windings are numbered low to high from inner to outer layer. The inner most winding 1 has 13 turns, and the outer two have 12. The winding layout cross-section can be seen in Figure 6.2. The number of turns was chosen so that at nominal operating speed the first winding's back emf voltage magnitude would equal 120 V according to design. The layers are dielectrically isolated by Kapton tape. A bobbin for protecting the winding from the sharp edges of the U-cores was 3D printed using Proto-pasta's high temperature polylactic acid (HTPLA).

Shielded 6005-Z deep groove ceramic ball bearings were used. The bearing inner diameter had to be sized so that the six flexible wires (two for each winding) could clear the rotor from the center of the axle and exit at the bottom of the axle. As a result the bearings are over sized with regards to static and dynamic load capacity.

The two main challenges of constructing the prototype were dealing with the tolerances of the cut cores and the winding of the machine. All tolerances of the cut cores were relatively large (up to +1.5 mm from nominal), including a tilt tolerance that indicates deviations from the ideal U shape. Several parts had to be re-machined or ground down to clear the desired 1 mm air gap. The resulting air gap was poorly controlled and resulted in reduced magnet flux linkage.

Winding the machine involved threading the wire through several tight bends and small holes. The Litz wire used was not very flexible and difficult to work with, and thus it was used only in the magnetically active winding area. It was first cut to length and tinned on both sides to remove the strands' insulation. After winding on the bobbin, the Litz wire was threaded through the plastic end plates and crimped to AWG 10 ultra flexible stranded wire.
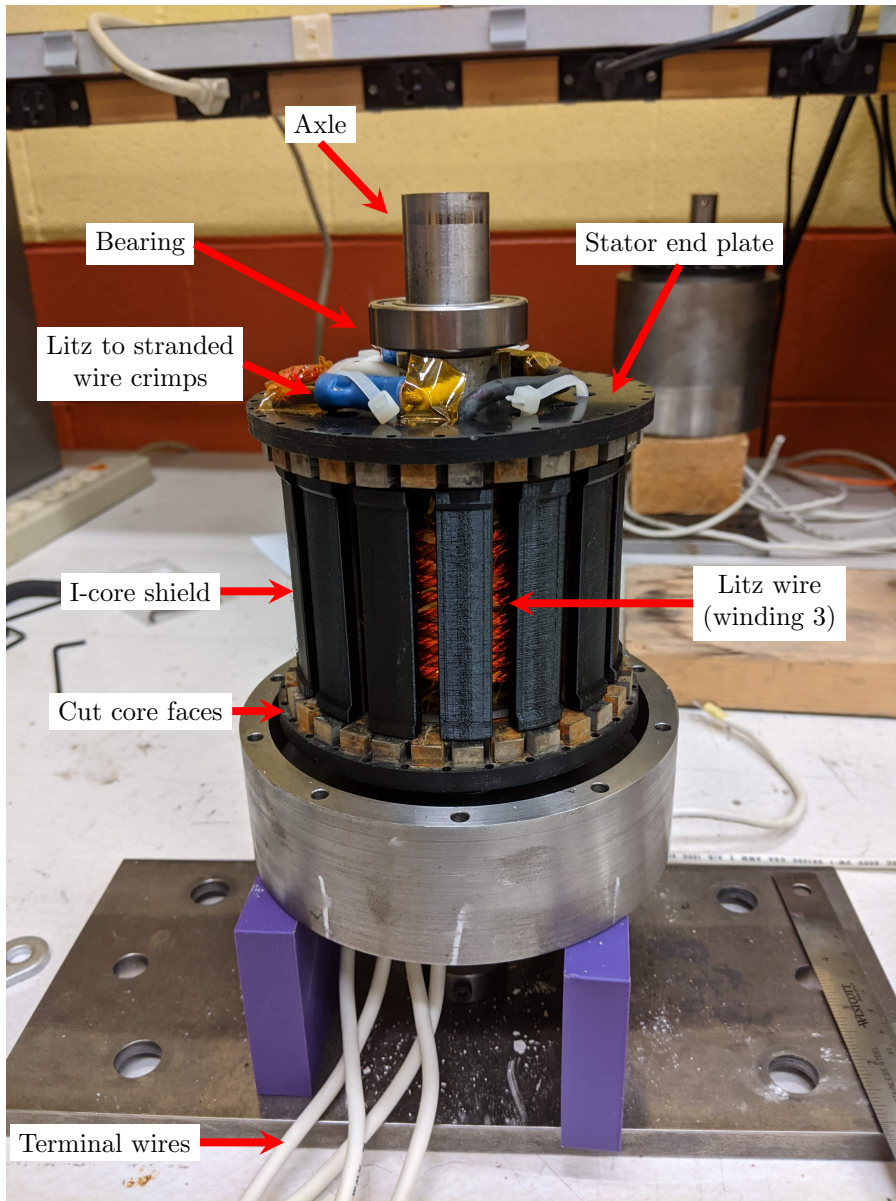
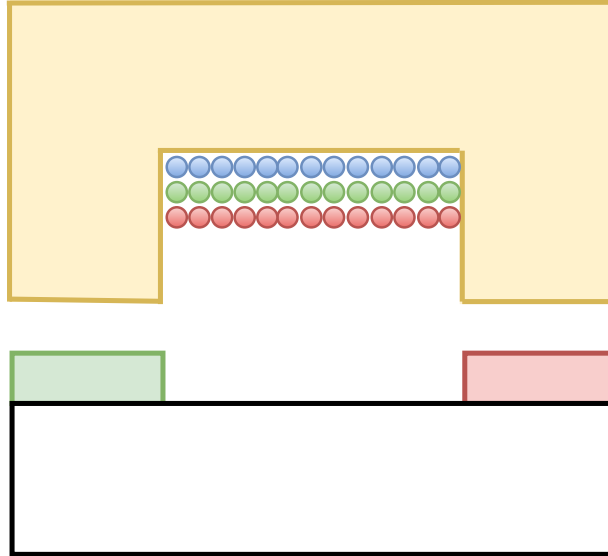Figure 6.1: Transverse flux machine stator with annotations.

Figure 6.2: Winding layers. Blue is winding 1, green is winding 2, and red is winding 3.

The wire then travels to the center of the axle through machined holes, axially downward, and exits from machined holes at the bottom of the axle. To aide with the threading, braided marine rope was first threaded through the entire path. The rope and flexible wire were then linked by a heat shrink tube, and the rope, along with the flexible wire, was pulled out. The use of slightly larger AWG number wire corresponding to a smaller copper cross-sectional area than designed and also the additional crimps contributed to a slightly higher than expected winding resistance.

6.1.2 Rotor

The rotor consists of three parts: two end plates and the central cylinder. The original prototype design had two circumferential rings of 30 magnets, and the rotor cylinder had 30 corresponding flats machined on its inner diameter. After the design change to 29 magnets in a ring, the cylinder inner bore was enlarged to accommodate rotor laminations. The inner bore was enlarged only up to an axial depth of 0.25" from both ends and has a circular inner diameter. Rotor laminations that have a circular outer diameter and 29 flats on the inner diameter were shrink fit into the cylinder bore with a -0.005" clearance. The rotor lamination stack consists of 25 sheets of 10 mil thick AKsteel HF-10. A drawing of the rotor cylinder modification can be seen in Appendix A Figure A.6. The magnets are neodymium (NdFeB), grade 52N. A picture of the rotor can be seen in Figure 6.3.

The two end plates each contain a pocket to seat the bearing outer raceway. The top bearing is press fit onto the axle, while the bottom bearing has a slip fit. A stationary wave disc washer is placed between the bottom bearing inner raceway and a shoulder on the axle. The amount of washer compression is determined by the bottom rotor end plate bearing pocket location, which sets the location for the bottom bearing outer raceway. The wave disc washer loads the bottom bearing axially downward with its spring force, and the top bearing is loaded axially downward with the washer spring force plus the weight of the rotor.
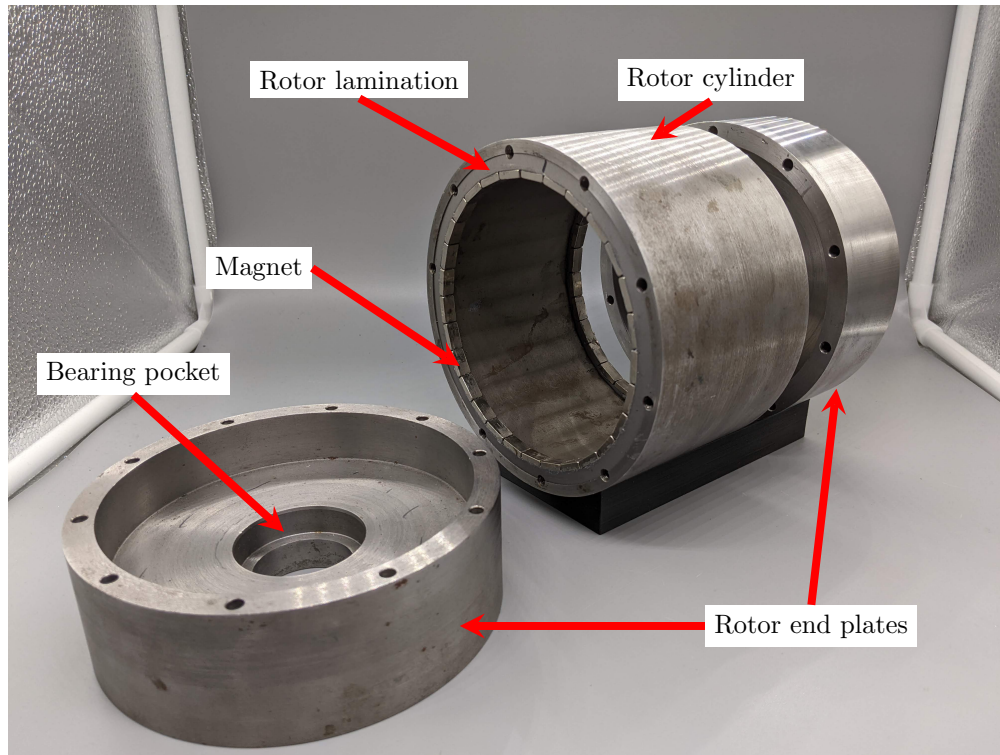
Figure 6.3: Transverse flux machine rotor with annotations.

The bottom wave disc washer supplies 33 lbs of bearing preload to the bottom bearing.

When installing the rotor laminations, an unintentional circumferential skew of approximately 2.5° mechanical (37.5° electrical) was added to one circumferential ring of magnets relative to the other. The flats on the two rotor lamination stack inner diameters were intended to align on the same plane. When a skew is added, the magnet flux linkage is decreased.

6.1.3 Mechanical Suspension and Containment

The machine is mounted with its rotational axis in the vertical direction, and a drawing of the mounting method can be seen in Figure 6.4. Polyurethane elastomer supports are press fit into the two ends of the axle and are used as compliant elements that incorporate damping. The other side of the urethane supports are press fit into steel plates. The bottom steel plate bolts directly into the concrete floor at the bottom of a test pit for containment. The pit is below grade and contains a 3 inch thick steel cylinder that surrounds the assembly. Outside the steel cylinder are sandbags.

One 1" thick steel plate is placed over the steel cylinder using a hydraulic lift and bolted down with eight 1" diameter tie rods. The machine assembly is slightly taller than the pit. Wooden blocks were used as spacers to allow the machine top steel plate to clear underneath the 1" steel plate. The terminal wires exited from the top of the pit through the gap created by the wooden spacers.
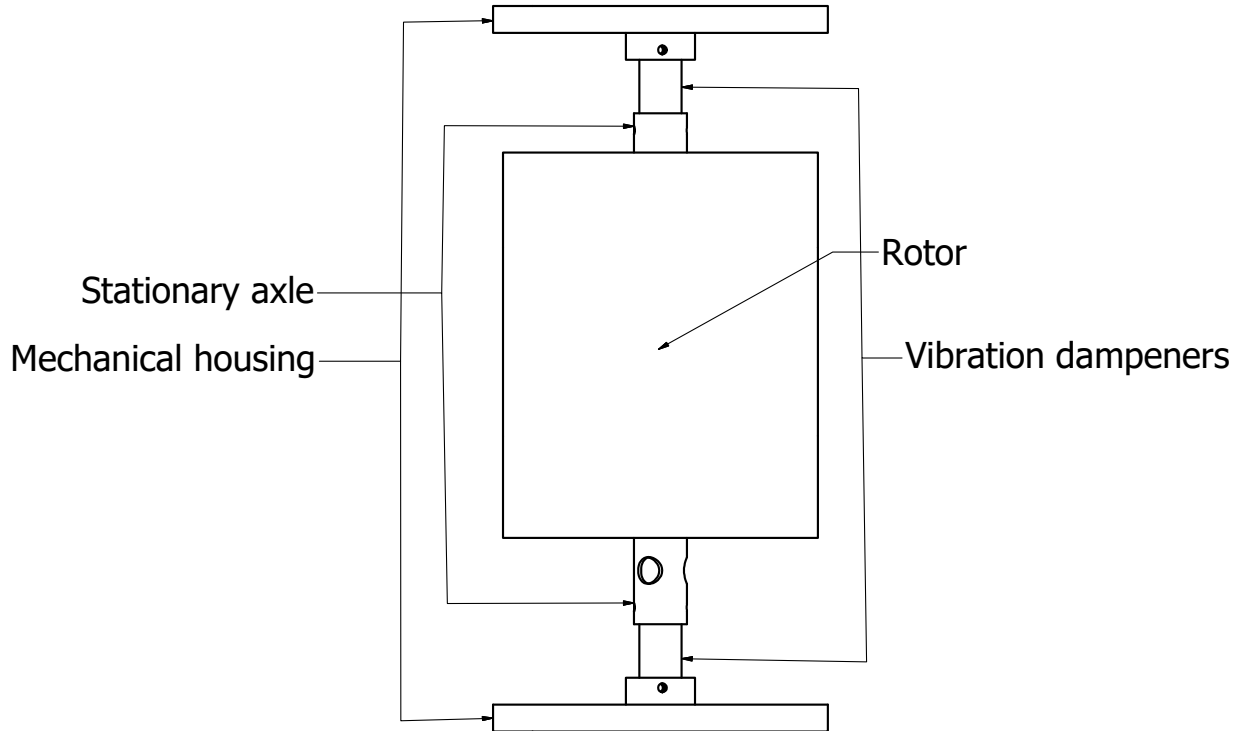
Figure 6.4: Mechanical suspension system overview.

6.2 Power Electronics

6.2.1 Power Converter PCB Layout

The power converter board can be seen in Figure 6.6. All power converters used in the experimental circuit setup as seen in Figure 7.2 were incorporated into a single large two layer PCB. The PCB contains four H-bridges. H-bridges 1 and 2 share a DC bus, and H-bridges 3 and 4 share another DC bus. The two DC buses are independent but not isolated. They share a common ground.

The gate driver ICs are all located remotely from the power transistors in a single row at the bottom of the board. The gate drive power signals are routed to their respective gate and source terminals through shielded twisted pair wires. The twisted pair wires help reduce the parasitic inductance in the gate drive loop. Excessive gate drive loop inductance was a potential concern of this design, but no negative effects such as ringing were observed in the gate drive waveforms. The gate drive arrangement is ideal for prototyping. By locating the gate drivers remotely, the routing of the board is greatly simplified. Potential capacitive coupling between the switching nodes with high dV/dt and gate drive logic signals is also mitigated. When a different gate drive pinout is desired, it is easy to reroute gate drive power signals, and no adhoc board modifications are needed.

Hall effect current sensors were installed on the DC sides of each H-bridge. The location is not ideal because it does not allow the measurement of the AC side current when the H-bridge is in a zero state. This prevents the measurement of the reactive current using the
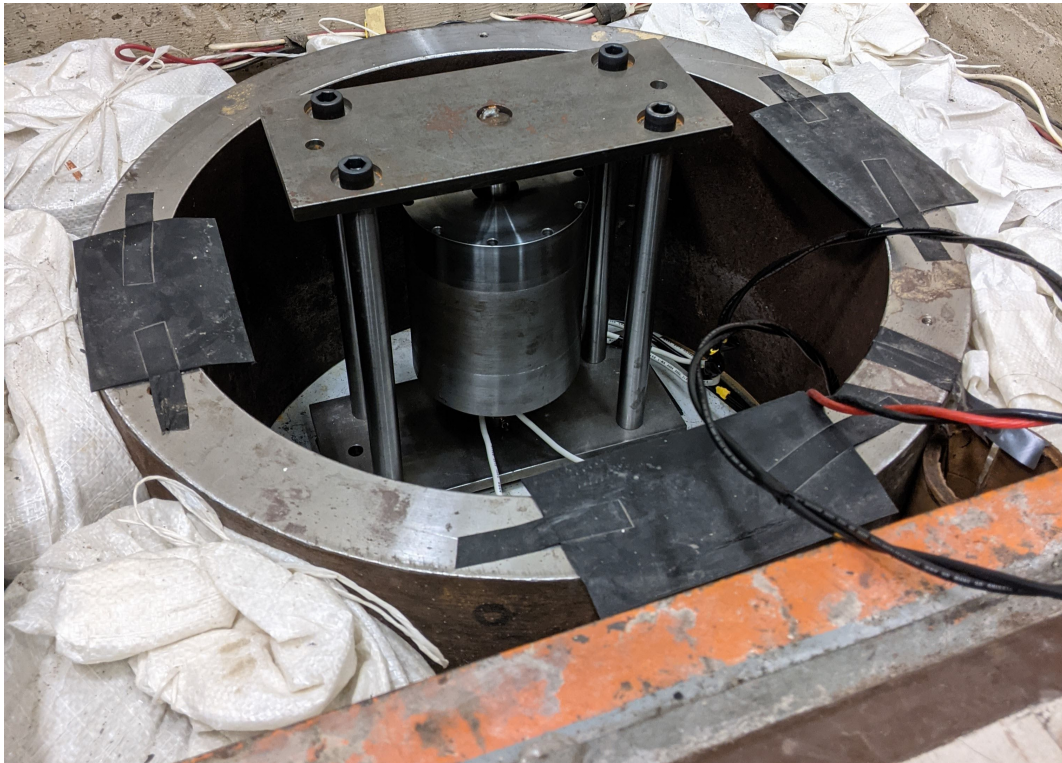
Figure 6.5: Machine assembly containment. The sandbags, steel cylinder, and machine assembly can be seen in the picture.
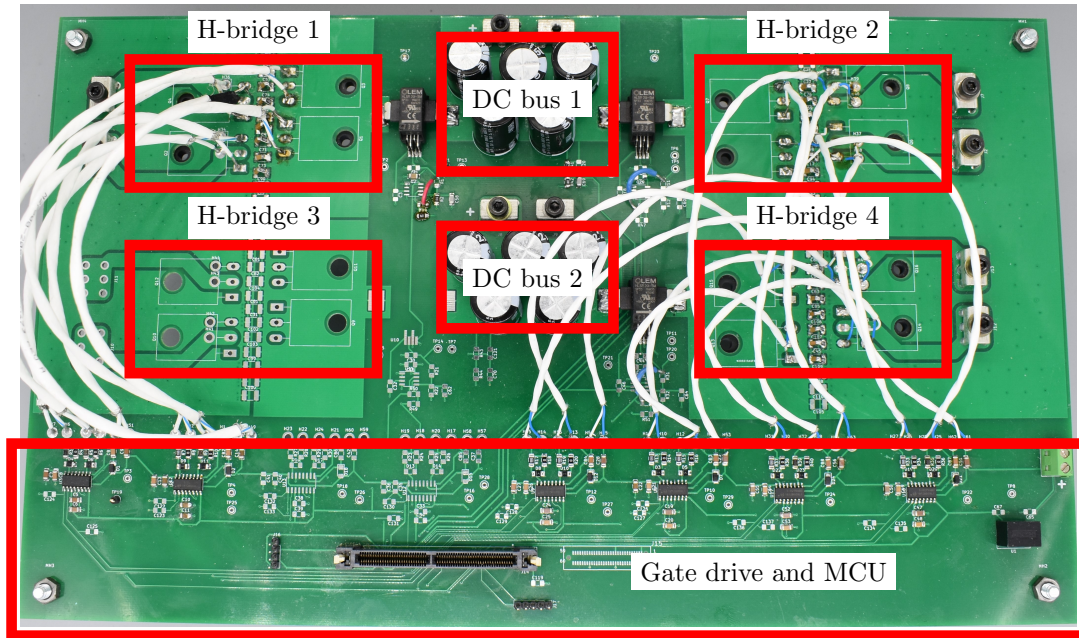
Figure 6.6: Drive PCB. H-bridge 3 is not populated. The power device transistor tabs are located underneath the board. The logic and gate drive are located at the bottom of the board.

control scheme presented in Section 5.1.2 because the sampling time of the reactive current is in the center of the zero state.

Silicon carbide (SiC) 700V and 900V transistors in the TO-247 package were used for their superior body diode reverse recovery characteristics over silicon MOSFETs. The body diode reverse recovery time for SiC transistors is around ten times less than that for silicon MOSFETs. SiC transistors also have two to three times less reverse recovery charge. Initially, silicon 200V transistors (IXFH180N20X3 and IRFP4668PbF) were used, but they displayed extremely poor body diode reverse recovery switching transients. During the hard switched edge when the body diode is turned off, the switching node would exhibit excessive overshoots and ringing.

The layout of the H-bridge circuit is very important to minimize parasitic trace inductance in the basic switching cell. The parasitic trace inductance in series with the parasitic transistor capacitances and local decoupling capacitors form a resonant circuit that rings during the switching node's hard switched rising edge. The switching cell layout can be seen in Figure 6.7. In the layout the switching loop involving the decoupling capacitors, high side switch, and low side switch has been made as small as possible. To reduce the parasitic inductance of the decoupling capacitors, many small ceramic capacitors were placed in parallel to close the switching loop. Small series resistances were added in series with the decoupling capacitors to dampen voltage overshoots.
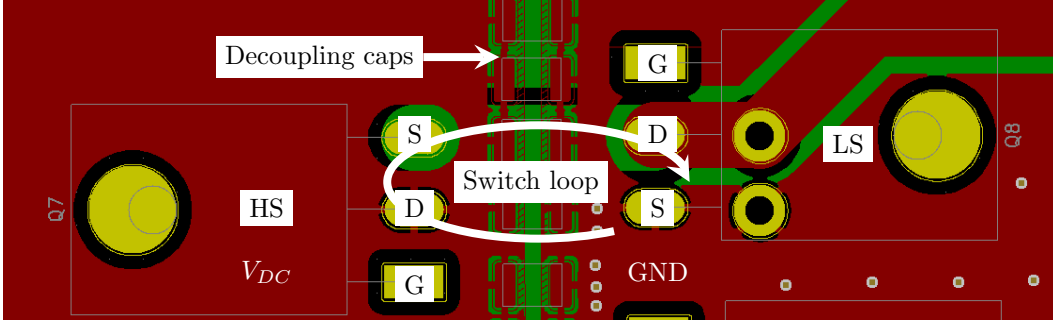
Figure 6.7: Switching cell layout. Red is front copper layer, and green is back copper layer. The front copper plane on the left is at the potential V_{dc}, and the right front copper plane is at potential GND.

6.2.2 TI C2000 Controller Software

The control algorithm was implemented on a TI F28379D controlCARD. The ePWM modules were used to generate the square waves. Special care was taken to setup the ePWM modules so that a control response twice per electrical period could be achieved. Single edge modulation was used, and the output was toggled upon match with the reference signal. The toggle action allows the generated square wave to have a period that is twice as long as the carrier signal period. The reference signal is used to control the square wave duty cycle. The square wave frequency is controlled by the carrier signal period. The carrier period can be adjusted at the middle of the square wave period smoothly without the potential for glitching. The ePWM module is able safely update the reference register from a reference shadow/buffer register when the carrier is reset to zero. This prevents the possibility of the reference being set to a value lower than the carrier as the carrier is counting up, resulting in a missed comparator match.

Double edge modulation was initially considered where the carrier counts up and then down. On the comparator match with the reference counting up, the output would be set high. On the match counting down, the output would be set low. However, adjusting the square wave period at the period's midpoint has the potential for glitches. If the reference is changed to a value that is larger than the carrier as the carrier is counting down, then the comparator match is missed for that half period. The ePWM module does not have the ability to safely update the reference register from a reference shadow/buffer register when the carrier reaches its maximum.

Phase shift modulation is used to generate the output square wave. The two legs of the H bridge generate a 50% duty unipolar square wave. The output of the H-bridge is the difference of those two voltages. Controlling the relative phase of the square waves in each leg results in a bipolar square wave output with the desired fundamental amplitude.

The timing diagram of the square wave generation scheme can be seen in Figure 6.8. Shown are the H-bridge's left leg voltage V_a, the right leg voltage V_b, the output voltage $V_a - V_b$, the carrier signal, and the two references Ref_A, Ref_B. The two reference signals correspond to the square wave output at the two H-bridge legs and are controlled differentially from the 50% common mode duty cycle. To find the i_q current, the motor current is sampled at the

phases $\pi/2$ and $3\pi/2$.

There are two interrupt routines - one for the motor controller and the other for generating 60 Hz PWM waveforms for the single phase load. The motor controller interrupt service routine occurs at twice the motor electrical frequency. It triggers at the end of an analog-to-digital conversion of the current. The second interrupt routine occurs at a fixed frequency of 20 kHz corresponding to the PWM frequency.
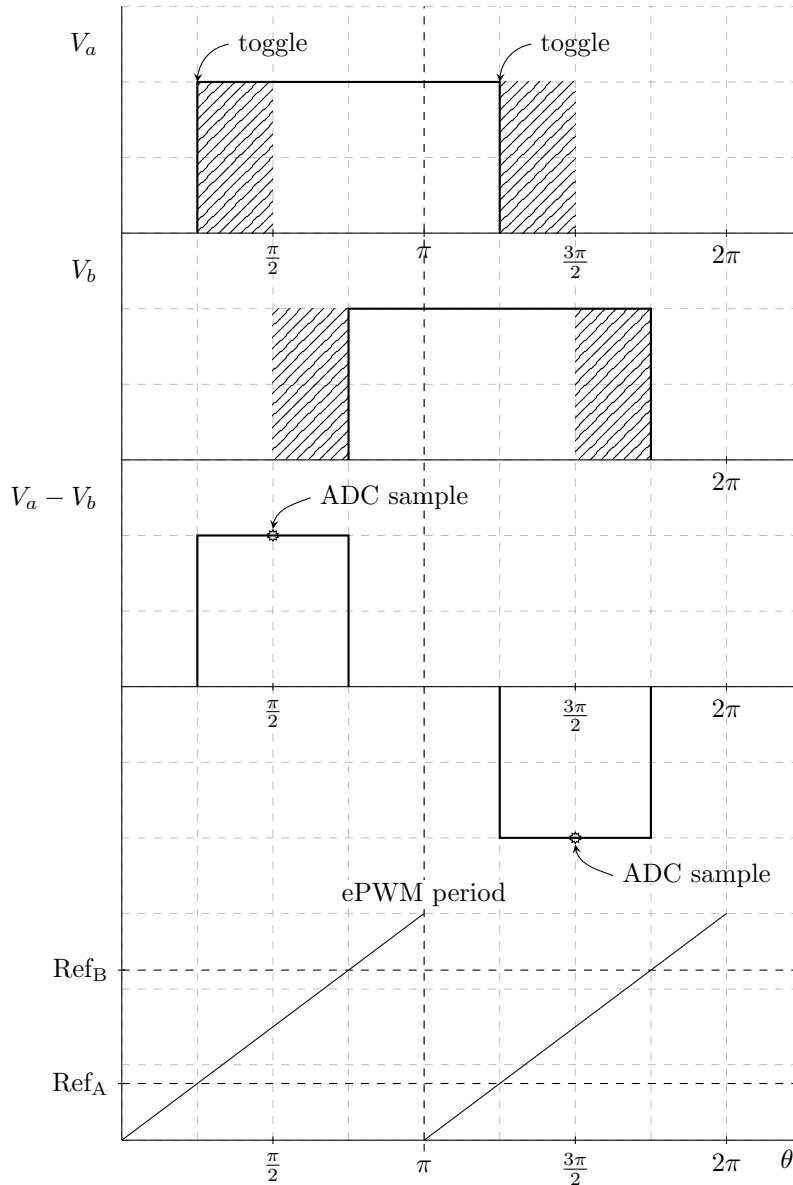
Figure 6.8: Square wave timing diagrams of H-bridge phase shift modulation. Shown are the H-bridge's left leg voltage V_a, the right leg voltage V_b, the output voltage $V_a - V_b$, the carrier signal, and the two references Ref_A, Ref_B.
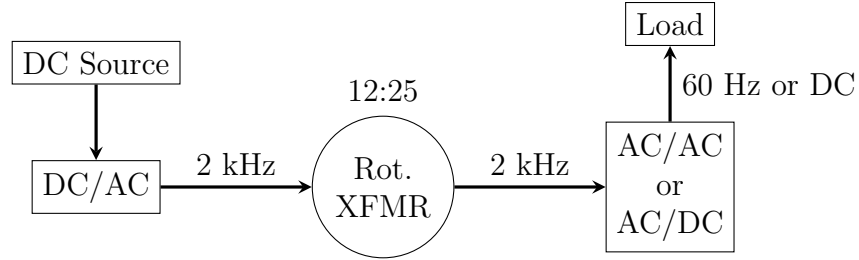
Figure 7.1: Block diagram of experimental setup.

7 Experimental System Results

This chapter presents the results of an experimental multiport system as seen at a high level in Figure 7.1. The system has two ports: a DC source is connected at one port (primary side) and a load at the other (secondary side). The load is either 60 Hz single phase or DC. It consists of a DC/AC converter, the rotating transformer, and an AC/AC or AC/DC converter. The rotating transformer is setup with a turns ratio of 12:25 by using winding 2 on the primary side and windings 1 and 3 in series on the secondary side. The system's functionalities of DC power transfer, 60 Hz AC power transfer with 120 Hz power balancing, and holdup energy are demonstrated.

The multiport system waveforms are presented in this section. First the basic functionality of transferring DC power from port 1 to 2 is shown. Then the system's 60 Hz AC power transfer with 120 Hz power buffering and its holdup energy functionality are demonstrated.

The experimental system in component level detail can be seen in Figure 7.2. The following quantities are labeled:

1. DC voltage source current

2a. Primary AC side current

2b. Secondary AC side current

3. Secondary DC voltage

4. Load current

All AC side current measurements are made by summing the primary and secondary AC side currents together. Due to the turns ratio and the identical switching sequences on both sides, the primary to secondary AC current ratio will always be 25:12. The AC side current measurement contains current that flows to the motor and also directly from the primary to secondary side, as the non-unity turns ratio does not cancel out those currents.

The load consists of a 4 Ω power resistor and a 435 μH inductor. The H bridge at the load is modulated to output either a DC or a 60 Hz voltage with PWM frequency of 20 kHz.

7.1 DC Power Transfer

DC power transfer from the DC source to load is shown in Figure 7.3. The top magenta trace is the secondary DC bus voltage, the yellow trace is the secondary AC side voltage, the
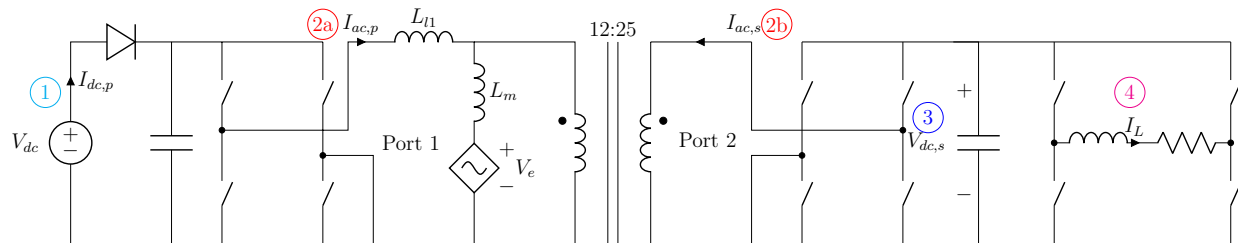
Figure 7.2: Component level detail of the experimental setup. Label 1 is the DC voltage source current, 2a is the primary AC side current, 2b is the secondary AC side current, 3 is the secondary DC voltage, and 4 is the load current.

blue trace is the load current, and the green trace is the AC side current. At the example operating point 36 W of power is transferred, and the machine's electrical frequency is 670 Hz.

The power transfer may only happen when the secondary DC voltage droops below the secondary referred primary side DC voltage. The droop happens during the primary/secondary AC side zero state. In this state, there is no power transfer from the primary side power supply, and the load current is supplied only from the secondary DC bus capacitors. During the active state when a non-zero voltage is applied at the primary and secondary AC sides in synchronism the two DC buses become connected incrementally in parallel through the leakage inductance and winding resistance. The difference in their voltages causes current to flow from the primary to the secondary side, and the secondary DC bus is recharged. The power transfer mechanism is analogous to that of switched capacitor converters or dual active bridge converters. The frequency of ripple in the secondary DC bus is equal to twice the machine's electrical frequency.

The blue load current is DC with a 20 kHz PWM ripple.

The AC side current has significant harmonic content at this operating point. The current takes on two distinct shapes depending on the state of the AC voltage. During the active state, the current is almost linear with a steep slope. The linearity arises from the short pulse widths, as the back emf does not change substantially during this short period of time. The square wave pulses are short to regulate the fundamental harmonic of the AC voltage down to match that of the back emf. The steep slope is explained by the large voltage mismatch between the DC bus and the back emf and also the recharging of the secondary DC bus. At this low electrical frequency the back emf magnitude is around 33.5 V on the secondary side, much lower than the 100 V secondary DC bus. A pulse of current also flows directly from primary to secondary side at the beginning of the active state to recharge the secondary DC bus.

During the zero states, the current is driven solely by the back emf. At 670 Hz the winding impedance is dominated by the winding self inductance. The back emf waveform can be inferred from this state, as it is proportional to the derivative of the current. The back emf zero crossings can easily be located at the instances where the current's slope changes sign. The sign of the back emf is equal to the opposite sign of the current's slope because of the current measurement polarity.
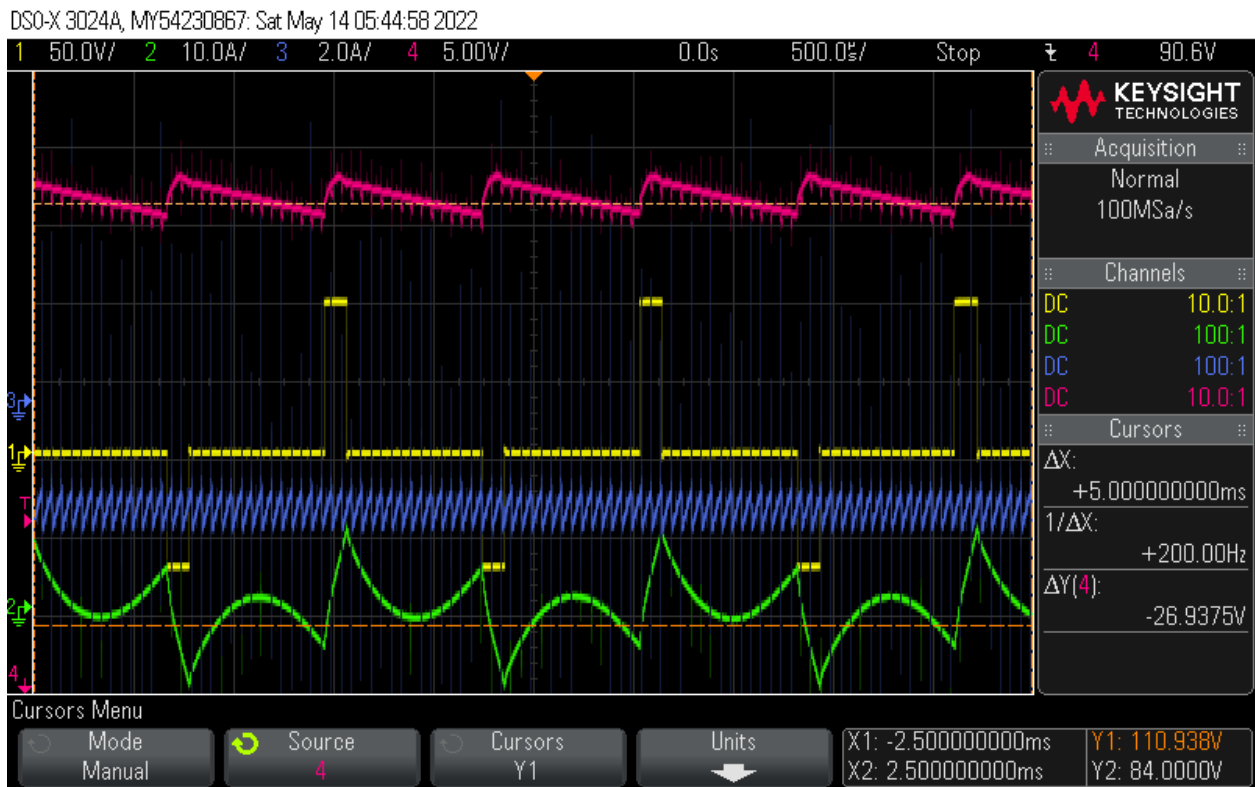
Figure 7.3: DC power transfer system waveforms. The top magenta trace is the secondary DC bus, the yellow trace is the secondary AC side voltage, the blue trace is the load current, and the green trace is the sum of the primary and secondary AC side currents.

7.2 Power Buffer

When the load on port 2 is 60 Hz single phase, there is an undesirable 120 Hz ripple present in the system waveforms. Figure 7.4 illustrates that effect. The plots are numbered as seen in the circuit diagram in Figure 7.2. The machine is rotating at 8 krpm with a back emf voltage magnitude of 50 V. The average power transferred is 300 W.

In the top blue plot of Figure 7.4, the DC voltage source current is shown. The pulses correspond to active states of the primary H bridge and so occur at twice the motor electrical frequency. Instantaneously during the active states the DC voltage source current is equal to the demodulated version of the AC side current. The DC voltage source current is forced to be positive by the series diode. The inverter is not operating at unity power factor, and the reactive currents are forced through the DC bus capacitor instead. The envelope of the voltage source current is modulated at 120 Hz, showing that it is supplying the 120 Hz pulsating power to the single phase load. During the zero states there is no path for the DC side current to flow, and therefore it is zero.

The secondary DC bus voltage in the third plot sags when the load current is large. The active state is not long enough for the secondary DC bus voltage to be fully recharged given the loading and the winding impedance. The last plot shows the load current as reference for the timing of the other waveforms.

Waveforms obtained after the 120 Hz power balancing active control is enabled can be seen in Figure 7.5. The DC voltage source current envelope no longer contains the 120 Hz ripple. It still is equal to the primary AC side current during the AC side active state and zero during the zero state. The current envelope is constant and equal to half the peak of that in the unbalanced case.

In the second plot the motor i_q current is shown in red and represents the motor instantaneous real power. The blue waveform is obtained by measuring the secondary DC side current and applying a 120 Hz bandpass filter. It represents the instantaneous real power minus the average power transferred to the load. In order to achieve the 120 Hz power balancing, those two quantities must be 180 degrees out of phase and also have the same amplitude at 120 Hz. The DC offset of the motor i_q current is equal to the i_q current required to maintain the machine at constant speed.

The third plot shows that the secondary DC bus is now regulated when the load current is high, during which the motor helps recharge the secondary DC bus. The last plot shows the load current as reference for the timing of the other waveforms.

7.3 Holdup Energy

The rotating transformer is able to supply hold up energy when the power source is suddenly disconnected. In an experimental demonstration of this capability, the machine is rotating at 8 krpm with a secondary side back emf voltage magnitude of around 105 V. One second of supplying hold up energy to a 250 W DC load is demonstrated. The secondary DC bus and load current are shown in Figure 7.6. When time equals zero seconds, the power supply is turned off and disconnected from port 1. The load current is maintained constant. The secondary DC bus begins to droop from the power imbalance until the controller detects the droop. Then the rotating transformer supplies power to regulate the secondary DC bus.
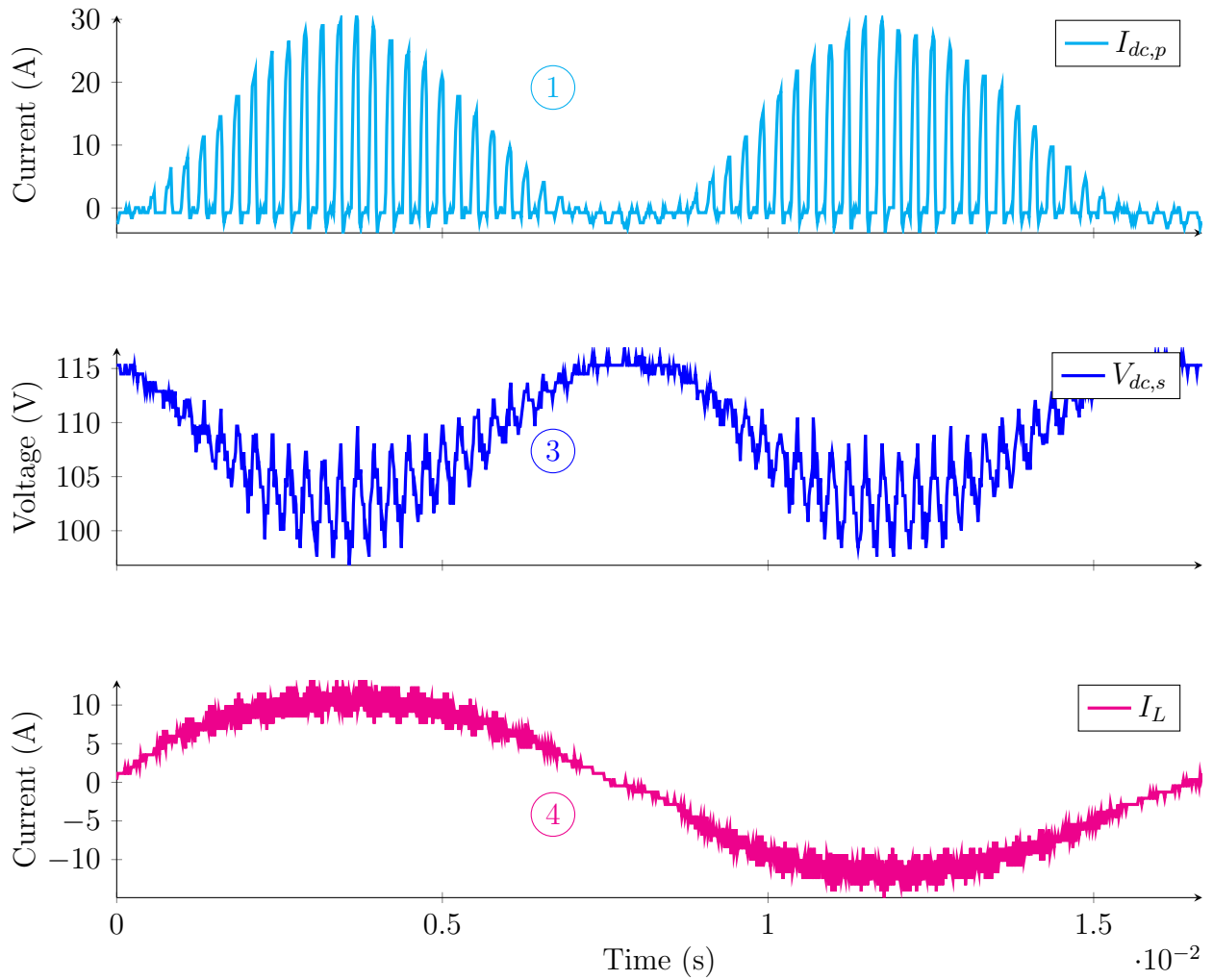
Figure 7.4: System waveforms showing the effect of 120 Hz system power imbalance. The top waveform is the DC voltage source current, the middle is the secondary DC bus, and the bottom is the load current.
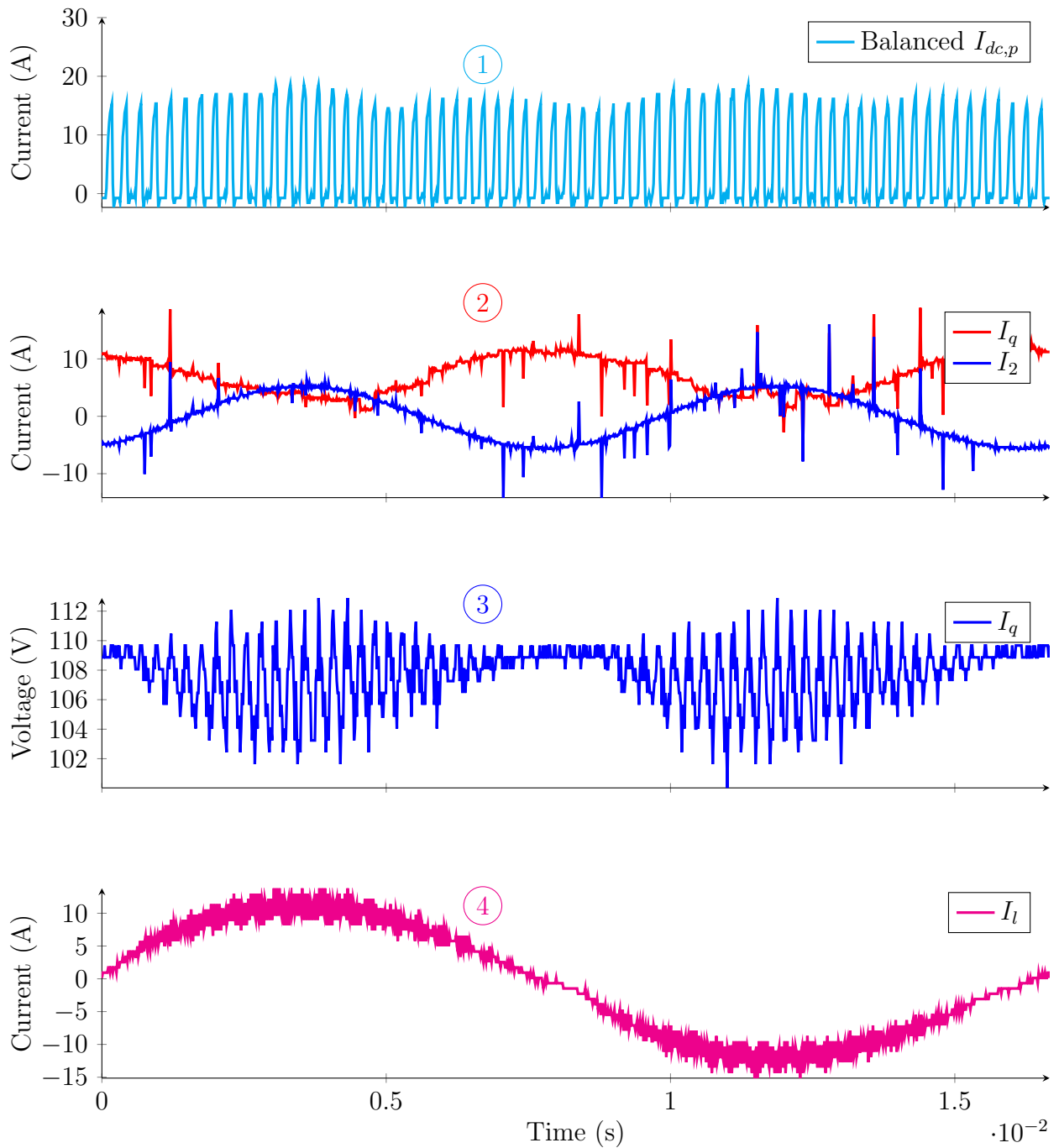
Figure 7.5: System waveforms are shown with the 120 Hz power balancing control enabled. Plot 1 shows the DC voltage source current, plot 2 shows the motor i_q current and the current representative of the 120 Hz power imbalance, plot 3 shows the secondary DC bus, and plot 4 shows the load current.
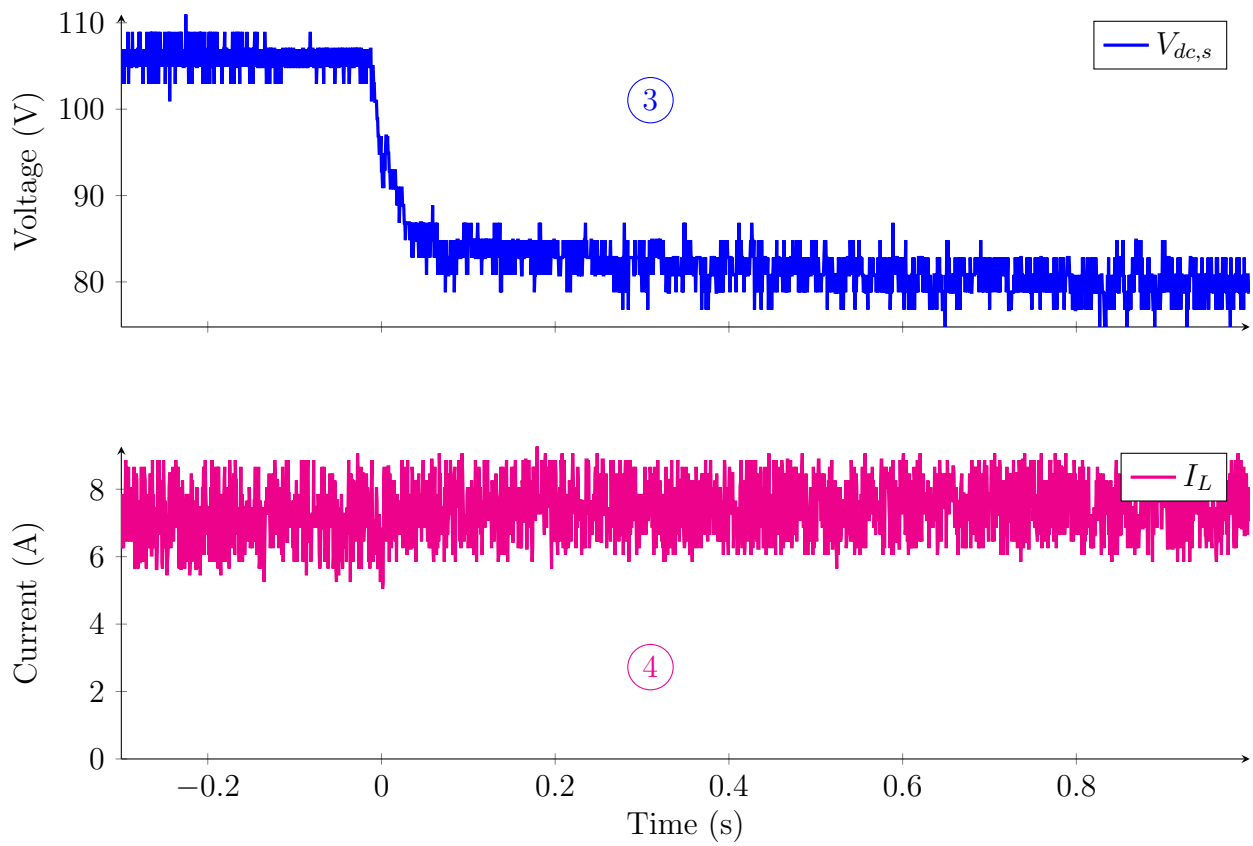
Figure 7.6: Secondary DC bus and load current waveforms showing constant power delivered to the load after power supply disconnection to $t = 0$s.
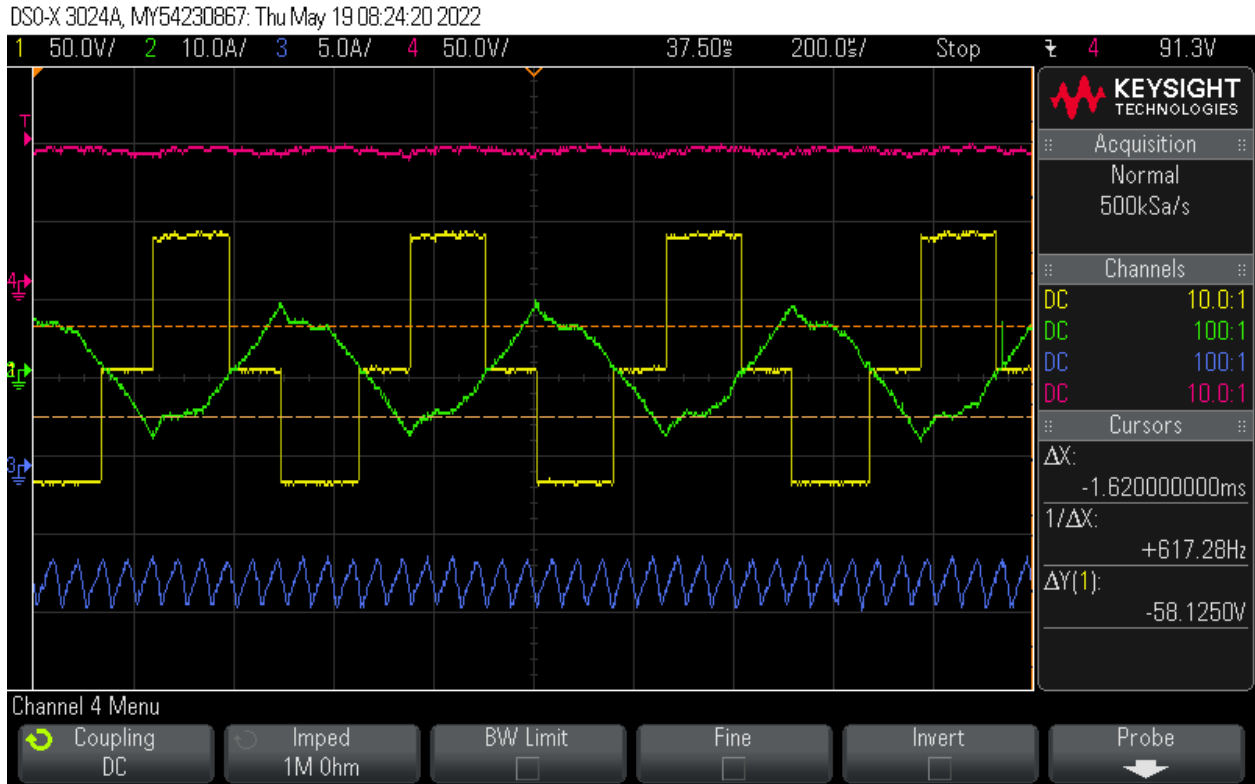
Figure 7.7: System waveforms after the power supply has been disconnected. The magenta waveform is the secondary DC bus, the yellow waveform is the secondary AC side voltage, the green waveform is the secondary AC side current, and the blue waveform is the load current.

The system waveforms are displayed in Figure 7.7 on the millisecond scale after the holdup control has been enabled. The magenta waveform on top is the secondary DC bus. It is being regulated to a constant value around 83 V. The yellow waveform shows the secondary AC side voltage, and the green waveform shows the secondary AC side current. The blue trace shows the load current with a 20 kHz PWM ripple.

8 Conclusion

A multi-port hub for integrating a single-phase utility connection, DC battery storage, DC PV generation, and critical customer loads was presented in this dissertation. The multiport system with rotating transformer has been demonstrated to solve many integration challenges in single-phase energy systems in a cost effective manner. The rotating transformer is an electric machine with multiple windings and provides the system with voltage conversion capabilities, galvanic isolation, 120 Hz ripple energy balancing for single-phase ports, and hold-up energy by use of intrinsic stored kinetic energy in rotation.

A prototype system was constructed that demonstrates all the functionalities of the rotating transformer. This dissertation has covered the design and implementation of the rotating transformer, its mechanical suspension, the system control, and the system power electronic converters.

References

[1] Department of Energy, "The SunShot Initiative," [Online]. Available: https://www.energy.gov/eere/solar/sunshot-initiative. [Accessed: 04-Dec-2018].

[2] W. Mackenzie, "Energy Research & Consultancy," Report — Wood Mackenzie, 07-Jun-2022. [Online]. Available: https://www.woodmac.com/reports/power-markets-us-solar-market-insight-q2-2022-150039609/. [Accessed: 15-Jul-2022].

[3] Ramasamy Vignesh, David Feldman, Jal Desai, and Robert Margolis. 2021. U.S. Solar Photovoltaic System and Energy Storage Cost Benchmarks: Q1 2021. Golden, CO:National Renewable Energy Laboratory. NREL/TP-7A40-80694.https://www.nrel.gov/docs/fy22osti/80694.pdf

[4] California Energy Commission, "Energy Commission Adopts Standards Requiring Solar Systems for New Homes, First in Nation," 09-May-2018. [Online]. Available: https://www.energy.ca.gov/releases/2018_releases/2018-05-09_building_standards_adopted_nr.html. [Accessed: 04-Dec-2018].

[5] "EIA's Residential Energy Survey now includes estimates for more than 20 new end uses," Homepage - U.S. Energy Information Administration (EIA). [Online]. Available: https://www.eia.gov/todayinenergy/detail.php?id=36412. [Accessed: 16-Jul-2022].

[6] "DigiKey Electronics Home," Digi. [Online]. Available: https://www.digikey.com/. [Accessed: 16-Jul-2018].

[7] P. T. Krein, R. S. Balog and M. Mirjafari, "Minimum energy and capacitance requirements for single-phase inverters and rectifiers using a ripple port", IEEE Trans. Power Electron, vol. 27, no. 11, pp. 4690-4698, Nov. 2012.

[8] F. A. Lindholm, Fossum, and Burgess, "IV curve," PVEducation. [Online]. Available: https://www.pveducation.org/pvcdrom/solar-cell-operation/iv-curve. [Accessed: 18-Jul-2022].

[9] "Maxout evergrid backup power turns grid tied system into a microgrid," maxoutrenewables.com. [Online]. Available: https://www.maxoutrenewables.com/evergrid. [Accessed: 19-Jul-2022].

[10] "American-made Solar prize," Energy.gov. [Online]. Available: https://www.energy.gov/eere/solar/american-made-solar-prize. [Accessed: 19-Jul-2022].

[11] K. Tweed, "Winning google's Little Box Challenge will take a 'holistic approach'," IEEE Spectrum, 24-Jun-2021. [Online]. Available: https://spectrum.ieee.org/google-little-box-inverter-challenge. [Accessed: 20-Jul-2022].

[12] "And the winner of the $1 Million Little Box Challenge is...CE+T power's Red Electrical Devils," Google AI Blog, 29-Feb-2016. [Online]. Available:

https://ai.googleblog.com/2016/02/and-winner-of-1-million-little-box.html. [Accessed: 20-Jul-2022].

[13] "C5750X6S2W225K250KA," DigiKey. [Online]. Available: https://www.digikey.com/en/products/detail/tdk-corporation/C5750X6S2W225K250KA/2733853. [Accessed: 20-Jul-2022].

[14] "Product specifications - mouser electronics." [Online]. Available: https://www.mouser.com/datasheet/2/257/Maxwell_BCSeries_DS_1017105-4-1179684.pdf. [Accessed: 20-Jul-2022].

[15] "Magnetics - T material," Magnetics - Ferrite Core Manufacturer. [Online]. Available: https://www.mag-inc.com/Products/Ferrite-Cores/T-Material. [Accessed: 22-Jul-2022].

[16] "Copper prices - 45 year historical chart," MacroTrends. [Online]. Available: https://www.macrotrends.net/1476/copper-prices-historical-chart-data. [Accessed: 22-Jul-2022].

[17] "K&J Magnetics," K&J Magnetics - Strong Neodymium Magnets, Rare Earth Magnets. [Online]. Available: https://www.kjmagnetics.com/. [Accessed: 22-Jul-2022].

[18] F. A. Raneiro, "Magnetic components," Magnetic Metals. [Online]. Available: https://www.magneticmetals.com/. [Accessed: 22-Jul-2022].

[19] "Steel pricing weekly average," UNARCO Pallet Rack and Warehouse Storage Systems, 22-Jul-2022. [Online]. Available: https://www.unarcorack.com/steel-average/. [Accessed: 22-Jul-2022].

[20] S. Boyd, S. Kim, L. Vandenberghe, and A. Hassibi, "A tutorial on geometric programming - Stanford University." [Online]. Available: https://web.stanford.edu/ boyd/papers/pdf/gp_tutorial.pdf. [Accessed: 09-Dec-2018].

[21] M. R. Harris, G. H. Pajooman and S. M. Abu Sharkh, "The problem of power factor in VRPM (transverse-flux) machines," 1997 Eighth International Conference on Electrical Machines and Drives (Conf. Publ. No. 444), Cambridge, UK, 1997, pp. 386-390.

[22] J. R. Anglada and S. M. Sharkh, "An Insight Into Torque Production and Power Factor in Transverse-Flux Machines," in IEEE Transactions on Industry Applications, vol. 53, no. 3, pp. 1971-1977, May-June 2017.

[23] C. Sullivan, "Optimal choice for number of strands in a litz-wire transformer winding," IEEE Transactions on Power Electronics, vol. 14, no. 2, pp. 283–291, 1999.

[24] Z. Q. Zhu and D. Howe, "Influence of design parameters on cogging torque in permanent magnet machines," in IEEE Transactions on Energy Conversion, vol. 15, no. 4, pp. 407-412, Dec. 2000, doi: 10.1109/60.900501.

[25] Maddison C.P., Mecrow B.C. and Jack A.G, "Claw Pole Geometries For High Performance Transverse Flux Machines", Int. Conf. on Elec. Mach. ICEM, pp. 340-345, Sept. 98, Vigo, Spain.

[26] Johnson L.A., Cornell E.P., Bailey D.J and Hegyi S.M., "Applications of low loss amorphous metals in motors and transformers", IEEE Power Eng. Soc. 1981, Transm. Distr. Conf. Expos.

[27] H. Shokrollahi and K. Janghorban, "Soft magnetic composite materials (SMCs)," Journal of Materials Processing Technology, Dec. 2007.

[28] Y. Guo, J. Zhu, H. Lu, Z. Lin and Y. Li, "Core Loss Calculation for Soft Magnetic Composite Electrical Machines," in IEEE Transactions on Magnetics, vol. 48, no. 11, pp. 3112-3115, Nov. 2012, doi: 10.1109/TMAG.2012.2197677.

[29] "Advanced Motor Design: New Motors reach new applications," Control Engineering, 10-Feb-2011. [Online]. Available: https://www.controleng.com/single-article/advanced-motor-design-new-motors-reach-new-applications/099e71c966a5dec800253ac2036e9fb2.html. [Accessed: 20-Jul-2022].

[30] Kraemer Erwin, Dynamics of Rotors and Foundations. Berlin: Springer Berlin, 2014.

[31] BASF, "Thermoplastic Polyurethane Elastomers Elastollan® – Material Properties," [Online]. Available: http://www.polyurethanes.basf.de/pu/solutions/en/ function/conversions:/publish/content/group/ Arbeitsgebiete_und_Produkte/Thermoplastische_Spezialelastomere/ Infomaterial/elastollan_material_uk.pdf [Accessed: 14-Dec-2018].

[32] A. Roshan, R. Burgos, A. C. Baisden, F. Wang and D. Boroyevich, "A D-Q Frame Controller for a Full-Bridge Single Phase Inverter Used in Small Distributed Power Generation Systems," IEEE Applied Power Electronics Conference, 2007.

[33] Hou, Haibo, W. Yao, and W. Zhang. "Vector control of single phase brushless DC motor." IEEE Electrical Machines and Systems (ICEMS), 2016.

[34] J.-Y. Lee and Y. Cho, "Synchronous Reference Frame Repetitive Control of a Single-Phase Three-Level Dual-Buck Photovoltaic Inverter," Electronics, vol. 7, no. 10, p. 226, Oct. 2018.

[35] R. Zhang, M. Cardinal, P. Szczesny, and M. Dame, "A grid simulator with control of single-phase power converters in D-Q rotating frame," 2002 IEEE 33rd Annual IEEE Power Electronics Specialists Conference. Proceedings (Cat. No.02CH37289).

[36] P. Kokotovic, H.K. Khalil, and J. O'Reilly. Singular Perturbation Methods in Control. London: Academic Press, 1986.

[37] M. Senesky and P. Tsao, "Simplified modelling and control of a synchronous machine with variable speed six step drive," Nineteenth Annual IEEE Applied Power Electronics Conference and Exposition, 2004. APEC 04.

[38] J. Xu, H. Qian, Y. Hu, S. Bian and S. Xie, "Overview of SOGI-Based Single-Phase Phase-Locked Loops for Grid Synchronization Under Complex Grid Conditions," in IEEE Access, vol. 9, pp. 39275-39291, 2021, doi: 10.1109/ACCESS.2021.3063774.

[39] A. Boglietti, P. Ferraris, M. Lazzari, and F. Profumo, "Energetic behavior of soft magnetic materials in the case of inverter supply," IEEE Trans. Ind. Applicat., vol. 30, pp. 1580–1587, Nov. 1994.

[40] W. C. Duesterhoeft, M. W. Schulz, and E. Clarke, "Determination of instantaneous currents and voltages by means of Alpha, beta, and Zero components," Transactions of the American Institute of Electrical Engineers, vol. 70, no. 2, pp. 1248–1255, 1951.

[41] R. H. Park, "Two-reaction theory of synchronous machines ," Electrical Engineering, vol. 52, no. 1, pp. 44–45, 1933.

[42] "Single-phase plls: A review of recent advances," IEEE Xplore. [Online]. Available: https://ieeexplore.ieee.org/stamp/stamp.jsp?arnumber=7819538. [Accessed: 20-Jul-2022].

[43] SKF bearing select. SKF Bearing Select. (n.d.). Retrieved June 22, 2022, from https://www.skfbearingselect.com/#/size-lubrication/single-bearing

[44] Tsao, P. (2003). An Integrated Flywheel Energy Storage System with a Homopolar Inductor Motor/Generator and High-Frequency Drive (dissertation).

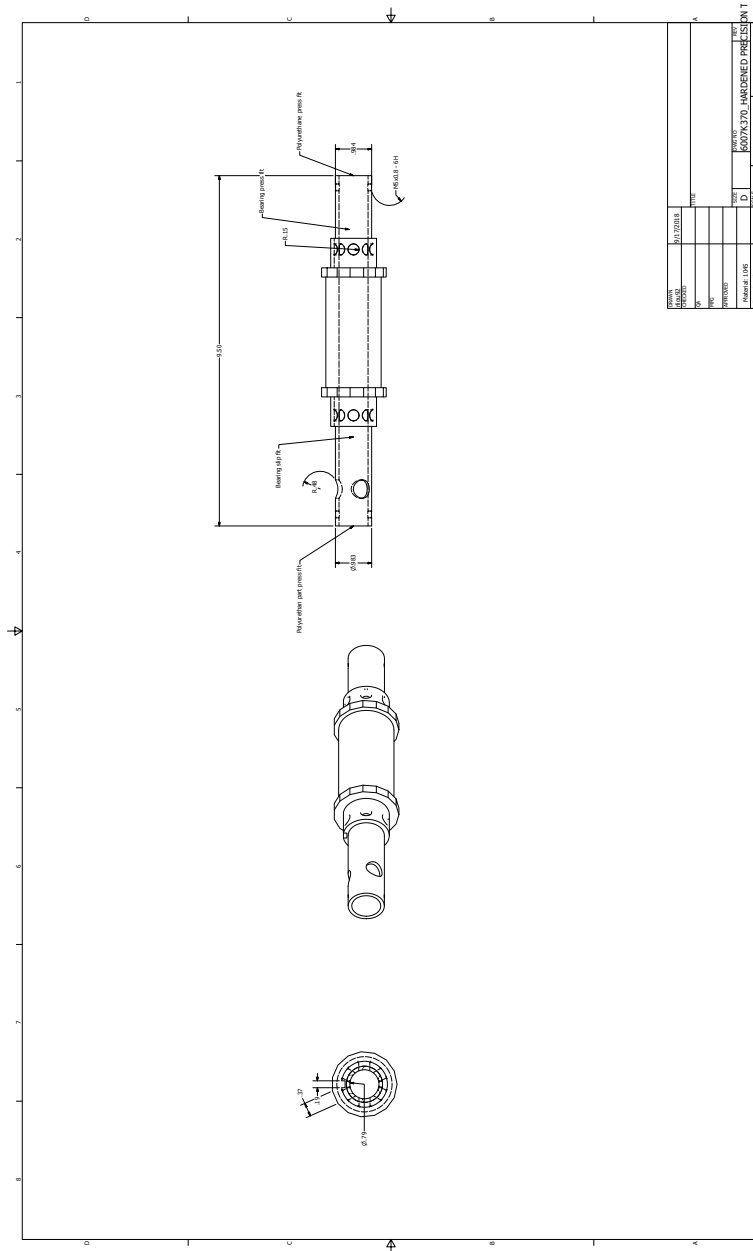# Appendices

A   Mechanical Drawings
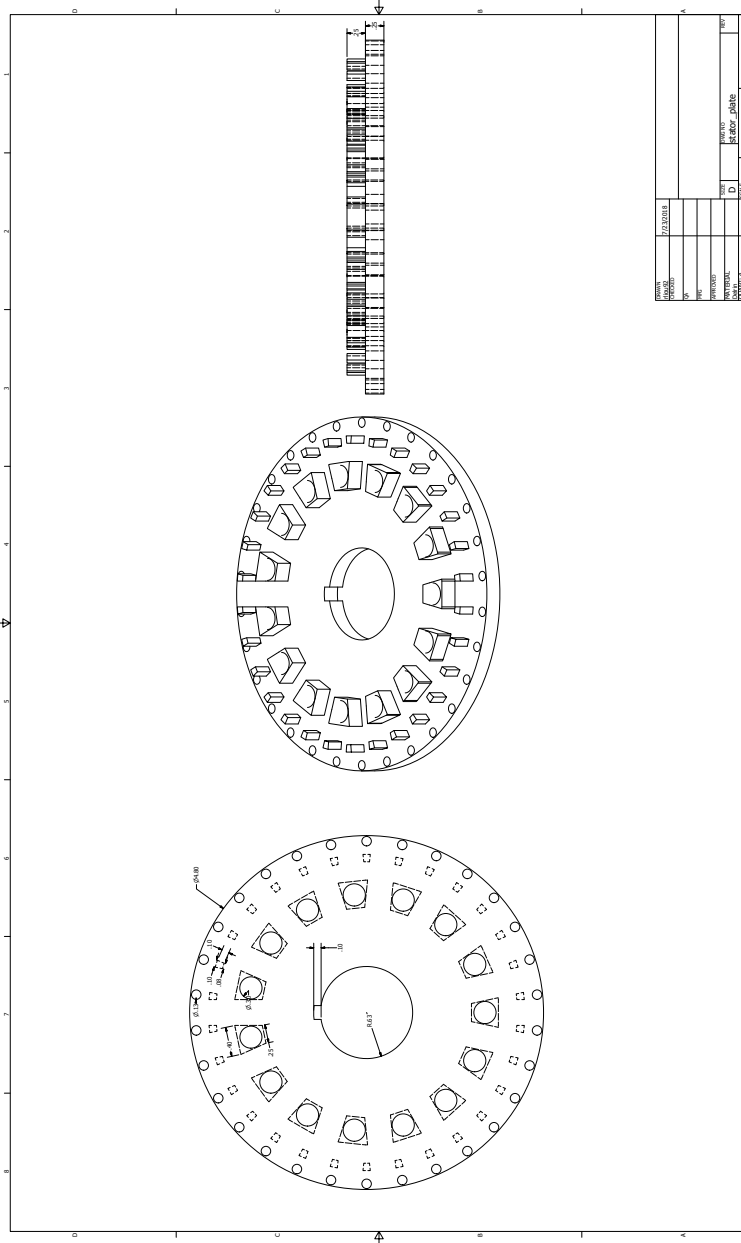

Figure A.1: TFM axle drawing.
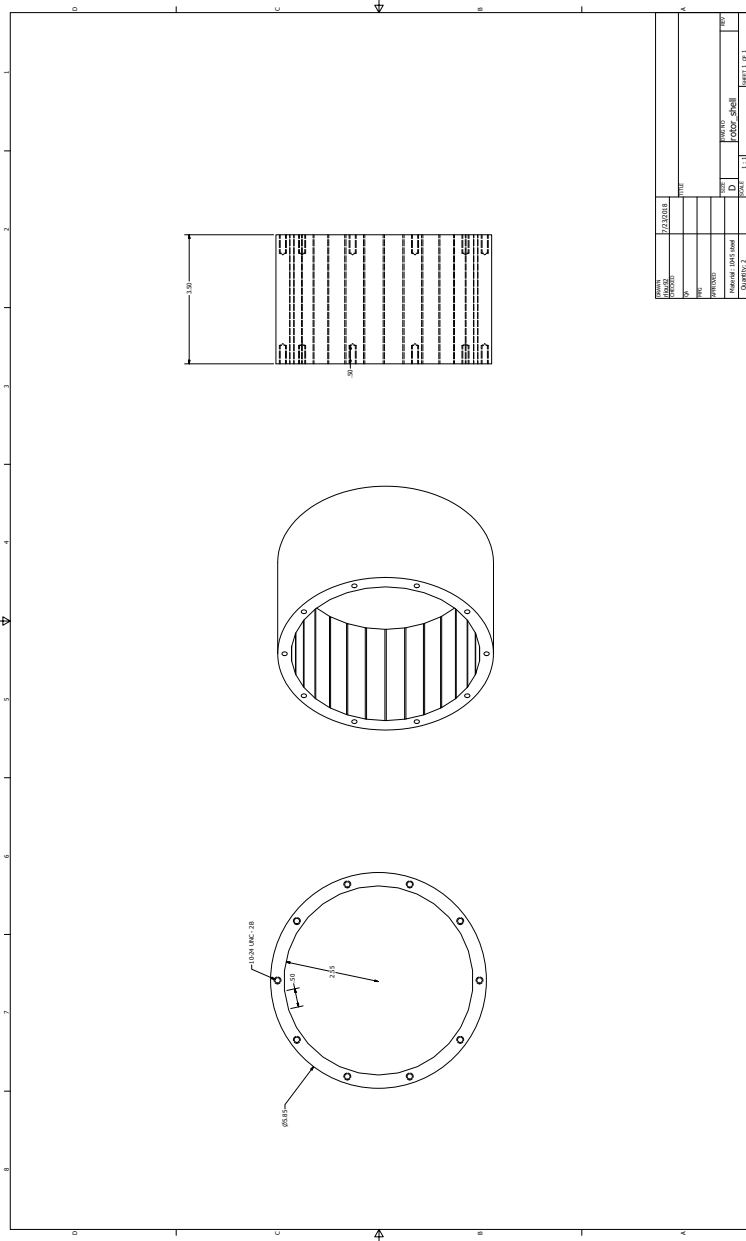
Figure A.2: TFM stator end plate drawing.
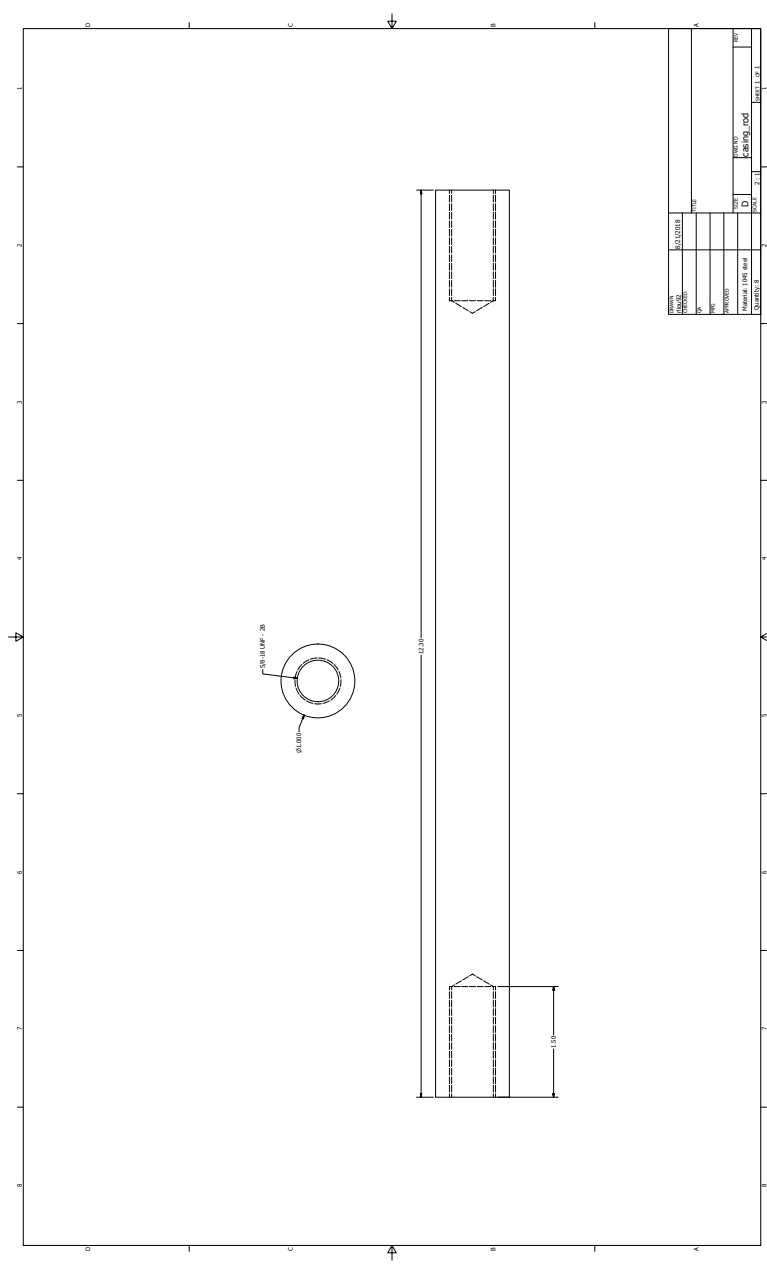
Figure A.3: TFM rotor shell drawing.
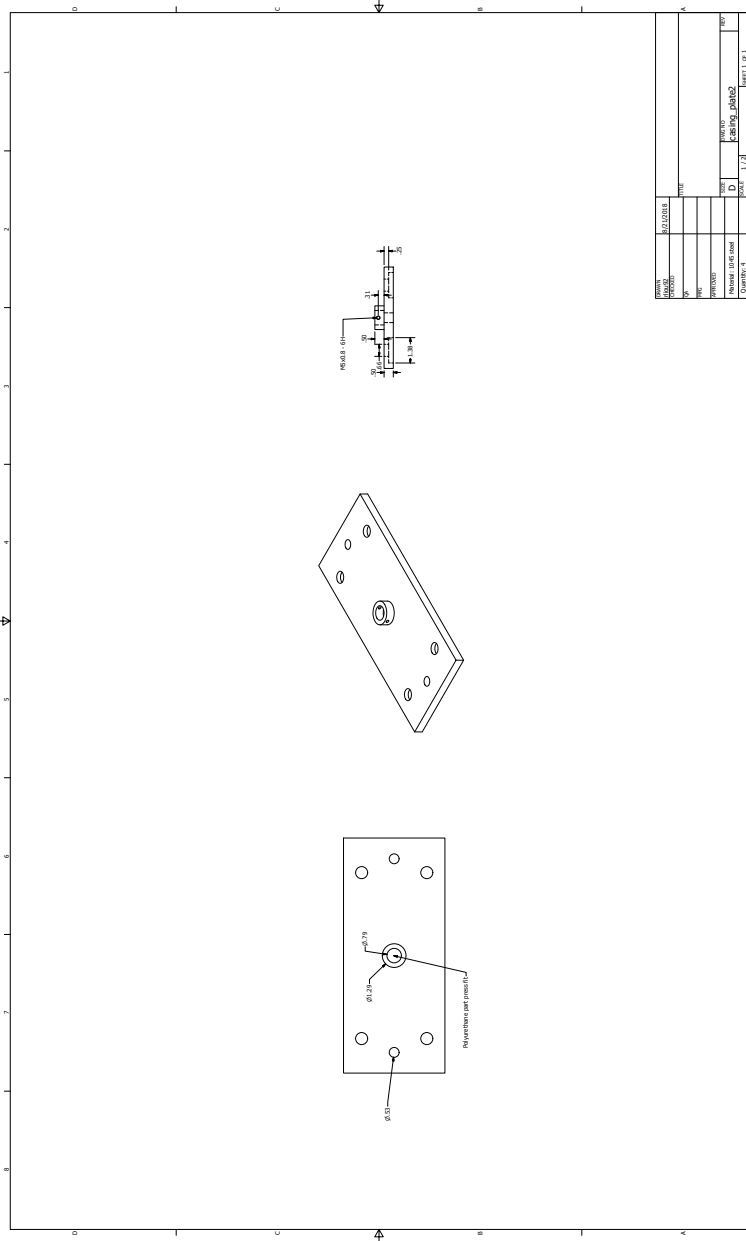
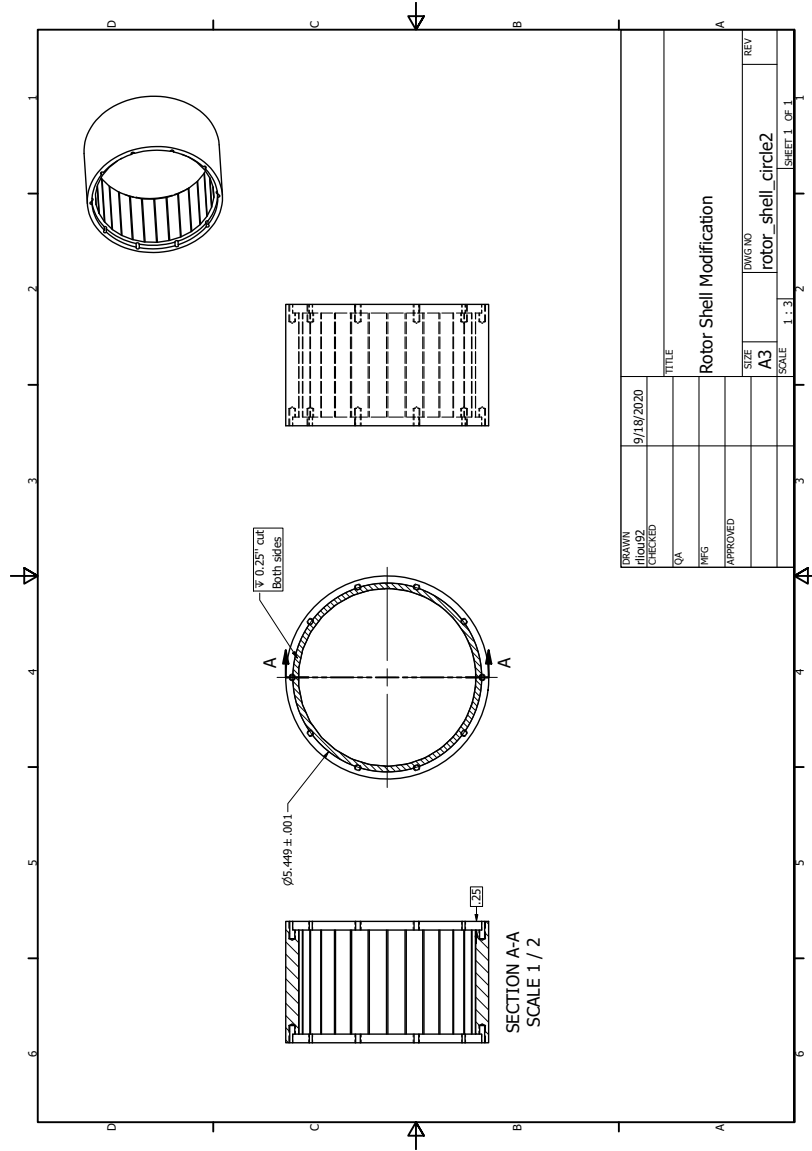Figure A.4: Mechanical support rod.

Figure A.5: Mechanical support plate.

Figure A.6: Rotor cylinder modification to accommodate rotor laminations and support two circumferential rings of 29 magnets.

B TFM Convex Optimization Design Code

```
%% constants
clear
m_to_in = @(x) (x)/.0254;
in_to_m = @(x) (x)*.0254;

Br = 1.3;
mu_0 = 1.2566e-6;
mu_r = 1.05;
g = 1e-3;
emf = 120;
k_f = .8;
k_r = .2; % lower is bad
k_p = .4;
cu_rho = 1.7e-8;
p_transfer = 3e3;
eff = .991;
metglas_density = 7150;
t = .125*.0254;
k_con = .7;
theta = pi/4;
power_angle = 60*pi/180;

%% CVX

% Assumptions for convexity:
% small angle approx
% estimate winding length as linear distance 2*pp*w (overestimate)
% treat magnet thickness as constant
cvx_begin gp
    variables wh ag w_m pp l w;

    f_m = w_m/2/pi;
    R1 = ag/(mu_0*(wh+l)*w);
    R2 = 2*(g+t)/(mu_0*w*l);
    w_e = pp*w_m;
    f_e = w_e/2/pi;
    Bg = Br/(1+mu_r*g/t);
    flux = k_f*Bg*w*l*pp/sqrt(2);
    N = emf/(w_e*flux);
    R = k_r/pp*(1/R1+1/R2)^(-1);
    L = N^2/R;
    X = w_e*L;
```

```
P = emf^2/X*sin(power_angle);

h = tan(theta)*(1-k_con)*w/2;
V_hf = pp*2*(1+k_con)*w*h/2*l;
V_met = w*2*pp*l*(ag+wh+3*l); % trap design
metglas_core_loss = 0.0000008*f_e^2+0.0019*f_e+0.4633;
hf_core_loss = 2.6505e-05*f_e^2+3.62e-02*f_e;
core_loss = metglas_core_loss*metglas_density*(V_met)+
    hf_core_loss*metglas_density*V_hf;
% Winding loss
winding_area = ag*(wh)*k_p/4;
r2_min = k_con/2*w*pp/pi;
r3_min = w*pp/pi; % w/(2*tan(pi/(2*pp)));
r4 = r3_min+t;

winding_avg_length = 2*pp*w;
winding_r = cu_rho*winding_avg_length/winding_area*N^2;
winding_loss = (p_transfer/emf)^2*winding_r;

V_mag = w*l*t*pp*4;

weight_met = 2.2*metglas_density*V_met; % lbs
weight_hf = 2.2*metglas_density*V_hf;
weight_mag = 2.2*metglas_density*V_mag;
weight = weight_met + weight_hf + weight_mag;
minimize (core_loss + winding_loss);

subject to

    % Power constraint
    P >= p_transfer;

    weight <= 5;

    1 <= pp <= 100;
    l >= in_to_m(.25);
    w >= in_to_m(.5);
    wh >= l+in_to_m(.5);
    w_m*r4 <= 90;

    r3_min >= r2_min+g+h+2*l+wh+.001; % so that C core won't
        collide in middle

cvx_end
```